# DEVELOPMENT AND ANALYSIS OF A HYBRID SOLID OXIDE FUEL CELL MICROTURBINE SYSTEM

by

**Michael M. Whiston**

B.A. in Philosophy, Secondary Major in Physics,

Carnegie Mellon University, 2009

Submitted to the Graduate Faculty of

the Swanson School of Engineering in partial fulfillment

of the requirements for the degree of

**Doctor of Philosophy**

University of Pittsburgh

2015

UNIVERSITY OF PITTSBURGH

SWANSON SCHOOL OF ENGINEERING

This dissertation was presented

by

Michael M. Whiston

It was defended on

July 14, 2015

and approved by

Laura A. Schaefer, PhD, Professor,
Department of Mechanical Engineering and Materials Science

Jeffrey S. Vipperman, PhD, Professor,
Department of Mechanical Engineering and Materials Science

Mark L. Kimber, PhD, Assistant Professor,
Department of Mechanical Engineering and Materials Science

Melissa M. Bilec, PhD, Associate Professor,
Department of Civil and Environmental Engineering

Dissertation Director: Laura A. Schaefer, PhD, Professor,
Department of Mechanical Engineering and Materials Science

**DEVELOPMENT AND ANALYSIS OF A HYBRID SOLID OXIDE FUEL CELL MICROTURBINE SYSTEM**

Michael M. Whiston, PhD

University of Pittsburgh, 2015

Hybrid solid oxide fuel cell microturbine (SOFC-MT) systems present opportunities for improvement over conventional systems, including high electric efficiency, cogeneration, and the potential for low carbon emissions. Hybrid systems require stringent control, however, and competing systems (including non-hybrid SOFC systems) currently generate power reliably and efficiently. In order to advance toward commercialization, hybrid systems need to adopt a control strategy that maintains safe and efficient operation, while also exhibiting favorable exergetic and economic performance.

The present work investigates the SOFC stack's dynamic response to step changes in control variables, as well as the hybrid and non-hybrid systems' energetic, exergetic, economic, and environmental performances. The numerical, 1-D, SOFC stack model developed herein allows for simulations on multiple timescales. An equivalent circuit combines the fuel cell's irreversiblities with the charge double layer. The hybrid and non-hybrid models integrate the SOFC stack model with the balance-of-plant component models, evaluating the energy and exergy flows through each component. Finally, the techno-economic model calculates the hybrid and non-hybrid systems' levelized costs of electricity (LCOEs).

Manipulating the current density is found to be the most effective way to control the fuel cell stack's power, giving rise to instantaneous power changes without restricting the fuel cell stack's fuel utilization. The charge double layer negligibly influences the fuel cell stack's behavior during normal operation, even during proportional-integral control. During baseload operation, the hybrid system model exhibits an LCOE of 8.7 ¢/kWh, and the non-

hybrid system exhibits an LCOE of 11.9 ¢/kWh. The hybrid system also operates at higher electric and exergetic efficiencies (58% (HHV) and 64%, respectively) than the non-hybrid system (44% (HHV) and 51%, respectively). The non-hybrid system cogenerates greater thermal energy than the hybrid system, however, yielding a fuel cost that is on par with that of the hybrid system. Both systems meet the EPA's proposed carbon pollution standard for new combustion turbines of 0.50 kg $CO_2$/kWh.

Hybrid systems demonstrate the potential to save fuel and money. Continued development of these systems, particularly focused on improving the system's dynamic behavior and minimizing cost, is warranted. Investment in hybrid systems will likely become viable in the future.

**Keywords:** solid oxide fuel cell, charge double layer, transient model, dynamic response, microturbine, gas turbine, hybrid system, techno-economic, cost, efficiency, exergy, environment, carbon dioxide emissions.

## TABLE OF CONTENTS

## LIST OF TABLES

## LIST OF FIGURES

## NOMENCLATURE

| | |
|---|---|
| $A$ | area $\left(\mathrm{m}^2\right)$ |
| $A_{\mathrm{plant}}$ | plant's availability (%) |
| $C$ | molar concentration $\left(\mathrm{mol/m}^3\right)$ |
| $C_{\mathrm{dbl}}$ | charge double layer capacitance (F) |
| $C_{\mathrm{f}}$ | Fanning friction factor (-) |
| $C_i$ | cost of component $i$ (\$/kW) |
| $C_{\mathrm{i,0}}$ | reference cost of component $i$ (\$/kW) |
| $C_{\mathrm{sys}}$ | system's total capital cost (\$/kW) |
| $CF_{\mathrm{e}}$ | electric capacity factor (-) |
| $CF_{\mathrm{h}}$ | heating capacity factor (-) |
| $c_{\mathrm{p}}$ | specific heat capacity at constant pressure $(\mathrm{J/kg \cdot K})$ |
| $CEPI$ | Chemical Engineering Plant Index (-) |
| $CEPI_0$ | Chemical Engineering Plant Index (reference) (-) |
| $D_{\mathrm{h}}$ | hydraulic diameter (m) |
| $D_i$ | combined diffusion coefficient of species $i$ $\left(\mathrm{m}^2/\mathrm{s}\right)$ |
| $D_{ij}$ | binary diffusion coefficient for species $i$ and $j$ $\left(\mathrm{m}^2/\mathrm{s}\right)$ |
| $D_{i,\mathrm{eff}}$ | effective diffusion coefficient for species $i$ $\left(\mathrm{m}^2/\mathrm{s}\right)$ |
| $D_{i,\mathrm{Knudsen}}$ | Knudsen diffusion coefficient for species $i$ $\left(\mathrm{m}^2/\mathrm{s}\right)$ |
| $D_{i,\mathrm{mixture}}$ | mixture diffusion coefficient for species $i$ $\left(\mathrm{m}^2/\mathrm{s}\right)$ |
| $\Delta T_{\mathrm{lm}}$ | log mean temperature difference (K) |
| $d$ | discount rate % |
| $\dot{\mathsf{E}}_{\mathrm{d}}$ | exergy destruction rate (W) |
| $\overline{\mathsf{e}}_{\mathrm{f}}$ | flow exergy (molar basis) (J/mol) |
| $\overline{\mathsf{e}}^{\mathrm{ch}}$ | chemical contribution to the flow exergy (molar basis) (J/mol) |
| $E_{\mathrm{N}}$ | Nernst potential (V) |
| $E_{\mathrm{act}}$ | activation energy (J/mol) |
| $F$ | Faraday's constant $\left(96485.34\ \mathrm{C\ mol}^{-1}\right)$ |
| $F_{\mathrm{c}}$ | fuel cost (\$/kWh) |

| | |
|---|---|
| $f_{\mathrm{e}}$ | equilibrium factor (-) |
| $\overline{g}$ | specific Gibbs function (molar basis) (J/mol) |
| HHV | higher heating value (J/kg) |
| $h$ | convection coefficient $\left(\mathrm{W/m^2 \cdot K}\right)$ |
| $\overline{h}$ | specific enthalpy (molar basis) (J/mol) |
| $i$ | electric current (A) |
| $i_{\mathrm{equip}}$ | equipment inflation rate (%) |
| $j$ | current density $\left(\mathrm{A/m^2}\right)$ |
| $j_0$ | exchange current density $\left(\mathrm{A/m^2}\right)$ |
| $J_i^*$ | diffusive molar flow rate of species $i$ (mol/s) |
| $K$ | loss coefficient (-) |
| $k$ | thermal conductivity $(\mathrm{W/m \cdot K})$ |
| $k_{\mathrm{o}}$ | pre-exponential factor $\left(\mathrm{mol/s \cdot m^2 \cdot Pa}\right)$ |
| $K_{\mathrm{wgs}}$ | equilibrium constant associated with water-gas shift reaction (-) |
| $L$ | length (m) |
| LCOE | levelized cost of electricity ($/kWh) |
| LHV | lower heating value (J/kg) |
| $M_i$ | molecular weight of species $i$ (kg/mol) |
| $MC_i$ | maintenance cost of component $i$ ($/kW) |
| $\dot{m}$ | mass flow rate (kg/s) |
| $n$ | number of moles (mol) |
| $\dot{n}$ | molar flow rate (mol/s) |
| $Nu$ | Nusselt number (-) |
| $N_{\mathrm{ch}}$ | number of channels in fuel cell (-) |
| $n_{\mathrm{e}}$ | number of moles of electrons (-) |
| $p$ | pressure (Pa) |
| $\hat{p}$ | perimeter (m) |
| $p^\circ$ | standard pressure (101,325 Pa) |
| $p_i$ | partial pressure of species $i$ (Pa) |
| $q$ | thermal energy (W) or charge (C) |
| $R$ | ohmic or equivalent resistance ($\Omega$) |
| $R_{\mathrm{F}}$ | capital recovery factor (-) |
| $\overline{R}$ | universal gas constant (8.314 J/mol-K) |
| $\dot{r}_i$ | rate of reaction $i$ $\left(\mathrm{s^{-1}}\right)$ |
| $r_{\mathrm{e}}$ | effective pore radius of electrode (m) |
| $Re$ | Reynolds number (-) |
| $S$ | shape factor (m) |

| | |
|---|---|
| $S_{\mathrm{i}}$ | capacity of component $i$ |
| $S_{\mathrm{i,0}}$ | reference capacity of component $i$ |
| S/C | steam-to-carbon ratio (-) |
| $\overline{s}$ | entropy (molar basis) $(\mathrm{J/mol \cdot K})$ |
| $t$ | time (s) |
| $T$ | temperature (K) |
| $T_0$ | reference temperature (K) |
| $T_{\mathrm{b}}$ | boundary temperature (K) |
| $u$ | axial velocity (m/s) |
| $U$ | overall heat transfer coefficient $(\mathrm{W/m^2 \cdot K})$ |
| $U_{\mathrm{f,1}}$ | fuel cell's fuel utilization (definition 1) (-) |
| $U_{\mathrm{f,2}}$ | fuel cell's fuel utilization (definition 2) (-) |
| $U_{\mathrm{f,sys}}$ | sytem's fuel utilization (-) |
| $V_{\mathrm{op}}$ | operational fuel cell voltage (V) |
| $V_{\mathrm{dbl}}$ | charge double layer voltage (V) |
| $W$ | work (J) or width (m) |
| $\dot{W}$ | power (W) |
| $x$ | axial coordinate axis |
| $x_{\mathrm{reform}}$ | extent of methane steam reforming (-) |
| $y_i$ | mole fraction of species $i$ |
| $z$ | coordinate axis along fuel cell's thickness |

**Greek Symbols**

| | |
|---|---|
| $\alpha$ | transfer coefficient (-) |
| $\alpha^*$ | aspect ratio (channel height to channel width) (-) |
| $\gamma$ | pre-exponential factor $\left(\mathrm{A/m^2}\right)$ |
| $\Delta$ | change (final value − initial value) |
| $\varepsilon$ | porosity (-) or exergetic efficiency (%) |
| $\varepsilon_i$ | emissivity of surface $i$ (-) |
| $\eta$ | polarization (V) or efficiency (%) |
| $\lambda_{\mathrm{air}}$ | excess air ratio (-) |
| $\mu$ | dynamic viscosity $\left(\mathrm{kg/m^2 \cdot s^2}\right)$ |
| $\nu_i$ | stoichiometric coefficient of species $i$ (mol) |
| $\rho$ | density $\left(\mathrm{kg/m^3}\right)$ |

| | |
|---|---|
| $\sigma$ | Stefan-Boltzmann constant $\left(5.670 \times 10^{-8}\ \mathrm{W/m^2 \cdot K^4}\right)$ |
| $\sigma_i$ | electrical conductivity of structural component $i$ (S/m) |
| $\sigma_{ij}$ | collision diameter of species $i$ and $j$ $\left(\text{Å}\right)$ |
| $\tau$ | tortuosity (-) |
| $\tau_{\mathrm{dbl}}$ | electrochemical settling time (sec.) |
| $\tau_i$ | thickness of component $i$ (m) |
| $\tau_{\mathrm{w}}$ | wall shear stress $\left(\mathrm{N/m^2}\right)$ |
| $\Omega_{\mathrm{D},ij}$ | collision integral of species $i$ and $j$ (-) |

**Subscripts**

| | |
|---|---|
| a | air channel |
| AC | alternating current |
| act | activation |
| AGR | anode gas recycle |
| air | air |
| an | anode |
| blow | air blower |
| c | cross-sectional |
| ca | cathode |
| cell | fuel cell |
| ch | channel |
| CHP | combined heat and power |
| comp | compressor |
| container | fuel cell stack's container |
| conc | concentration |
| cond | conduction |
| conv | convection |
| DC | direct current |
| e | electric |
| electro | electrolyte |
| eoh | electrochemical oxidation of hydrogen |
| exhst | exhaust |
| f | fuel channel |
| fuel | fuel |

| | |
|---|---|
| htg | heating |
| inlet | inlet |
| loss | loss |
| msr | methane steam reforming |
| preheat | air pre-heater |
| inter | interconnect |
| ohm | ohmic |
| PEN | positive electrode-electrolyte-negative electrode |
| rad | radiation |
| ref | reformer or reformate |
| rib | ribbing in interconnect |
| s | surface |
| seg | computational segment |
| SOFC | solid oxide fuel cell |
| stack | fuel cell stack |
| sys | system |
| turb | turbine |
| wgs | water-gas shift reaction |

**Superscripts**

| | |
|---|---|
| ch | channel |
| tpb | triple-phase boundary |
| $^\circ$ | standard pressure (101,325 Pa) |
| $''$ | per unit cross-sectional area |
| $'''$ | per unit volume |
| $^-$ | molar |

# 1.0 INTRODUCTION

The present work develops and analyzes a hybrid solid oxide fuel cell microturbine (SOFC-MT) system model. SOFCs are alternative energy devices that convert chemical energy directly into electricity at relatively high temperatures. Fuel cells are modular, electrically efficient, and well-suited for distributed generation. Microturbines are also modular, high-temperature devices that are well-suited for distributed generation. Microturbines currently meet a wide range of energy needs, including baseload power and heating. Integrating a solid oxide fuel cell stack with a microturbine presents a number of benefits, including increased power generation, improved fuel cell performance, and the potential for low environmental impact. The present work contributes to a number of areas in this regard. In particular, the present work simulates the SOFC stack's dynamic response to load changes, investigates electrochemical dynamics inside the SOFC, performs exergy and economic analyses of the hybrid system, and performs an environmental analysis of the hybrid system. The end of this chapter summarizes these contributions in more detail.

## 1.1 MOTIVATION

The motivation for the present work stems from the growing need for distributed generation systems. Distributed generation is the generation of electricity near the point of consumption [1, 2]. Distributed generation systems present a number of benefits, including cogeneration and the elimination of transmission and distribution (T&D) losses. SOFC-MT systems, in particular, offer especially high electric efficiencies, enhanced fuel cell performance, and the potential for low $CO_2$ emissions. There is a need, however, to better understand these systems

through modeling and simulation. The reasons for pursuing the present work are discussed in more detail below.

### 1.1.1 Combined Heat and Power

Combined heat and power, or CHP, is the simultaneous production of electricity and useful thermal energy, both from the same fuel source [3,4]. Because distributed generation systems generate electricity near the point of consumption, byproduct thermal energy may readily be used or stored alongside the electricity. By recovering thermal energy from the exhaust stream that would otherwise be wasted, CHP has the potential to achieve overall efficiencies as high as 80%, where the overall efficiency is defined as the sum of net electricity and net thermal energy divided by the fuel's higher heating value, or HHV [5]. University and college campuses, manufacturing plants, and wastewater treatment facilities are among the many users of CHP. CHP prime movers include reciprocating engines, gas turbines, steam turbines, fuel cells, and microturbines, and CHP systems may be sized and operated in a number of different ways. Systems operating in parallel with the power grid, for instance, may be sized to meet the baseload power demand of a building while importing power from the utility. Alternatively, systems may be sized to meet a building's peak power demand, selling excess power back to the grid. Generally speaking, the amount of thermal energy recovered determines the system's overall efficiency [3,6,7]. When integrated with renewable energy sources, CHP has the potential to generate clean, grid-independent power [8]. The choice of system design and operating strategy ultimately depends on the application.

Fuel cells and microturbines currently meet various energy needs. Fuel cell systems, for instance, meet 35% of the electricity and thermal energy demand of the Coca-Cola Bottling Company plant in Elmsford, NY. At this site, two 440 kW fuel cell systems provide continuous electricity, thermal energy for process and space heating, and backup power [9]. On a larger scale, a 2.8 MW fuel cell system helps meet the baseload power demand of a wastewater treatment facility in San Bernardino County, CA. This system consumes biogas and recycles the cogenerated thermal energy back to the anaerobic digester [10]. Microturbines meet various energy needs as well. The Crayne Compressor Station in Waynesburg, PA,

relies on three microturbines to meet 100% of the buildings' electricity and thermal energy loads, and the microturbines consume the same pipeline natural gas handled by the station. Thermal energy from the microturbines is also used to heat and decompress the natural gas, which is a process that would otherwise require thermal energy from a boiler [11]. University and college campuses also rely on microturbines. Microturbines meet 80% of the electricity demand and 100% of the heating and cooling demand of a facility located on Salem Community College's campus in Carneys Point, NJ [12]. At Foothill College in Los Altos Hills, CA, microturbines produce thermal energy to heat the college's Olympic-sized swimming pool [13]. Therefore, microturbines and fuel cells both demonstrate strong potential for continued growth.

### 1.1.2 Avoided Transmission and Distribution

Distributed generation systems avoid losses associated with transmitting and distributing electricity long distances, as they generate electricity near the point of consumption. Centralized power systems transmit electricity many miles before reaching customers. The U.S. transmission sector is partitioned into three interconnections, comprising (mostly) AC lines at 60 kV or greater. Power is stepped up in voltage before entering the high-voltage transmission lines, and after being transmitted many thousands of miles, the electricity is converted to low voltage by a step-down transformer. The electricity is then delivered to industrial, commercial, and residential customers by distribution lines [14]. Unfortunately, electricity is lost during this transmission process. Between 2004 and 2013, transmission and distributions losses amounted to 6% (on average) of the electricity transmitted and distributed annually in the U.S. [15]. Distributed generation systems avoid such losses by generating electricity on-site. That is, distributed generation systems generate electricity near the point of consumption, thus minimizing the distance between generation and consumption.

In addition to avoiding T&D losses, distributed generation systems provide a relatively easy way to accommodate new energy demand. Distributed generation systems connect directly to local loads (or the distribution network) via interfacing circuits [7], thus avoiding the complexities associated with expanding the T&D infrastructure. Expanding the grid

may require significant time and effort. Transmission projects must be approved at both the federal and state levels [14], and the capital costs associated with building new transmission lines are high, particularly if the lines are built underground [2]. Distributed generation systems also benefit from economies of production. Packaged (prefabricated) CHP systems, such as kW-scale reciprocating engines and microturbines, are relatively easily manufactured, tested (in-house), and commissioned in the field [3,6]. Microturbine models even (optionally) come packaged with heat recovery equipment, thus further simplifying their procurement [16].

As an additional benefit, distributed generation systems have the potential to generate power reliably. Fuel cells have demonstrated availabilities greater than 90% [5], and reciprocating engines have demonstrated availabilities exceeding 95% [5]. Parallel operation of these devices permits especially high reliability. If a distributed generator fails, that is, nearby generators may serve as backup [1, 2]. In the case of a grid outage, distributed generation system can also provide emergency power. Outages in the T&D sectors propagate rapidly, and on-site generators, particularly reciprocating engines, help to maintain power to critical loads [5]. In terms of power quality, distributed generation systems have the ability to deliver (and maintain) power at required voltage and frequency levels. Electricity storage, for instance, may be combined with small-scale generators to help stabilize the voltage in a microgrid [17]. Fuel cells control their output frequency using an inverter. The inverter converts boosted (or regulated) DC input into AC output, thus providing grid support, if needed [5].

### 1.1.3 High Electric Efficiency

Combining an SOFC stack with a microturbine enables the hybrid system to generate power efficiently. In fact, hybrid systems have the potential to achieve electric efficiencies approaching 70% (based on the fuel's lower heating value, or LHV) [18–23]. On their own, microturbines generate power at approximately 30% (LHV) electric efficiency [16, 24], and SOFC systems operate at 52%–60% (LHV) electric efficiency [25]. Fuel cells achieve higher efficiencies than microturbines because fuel cells convert chemical energy directly into electricity. Microturbines, on the other hand, require multiple conversion steps. That is, they

first convert chemical energy into thermal energy via combustion. The turbine then converts the thermal energy into mechanical energy via a rotating shaft. Finally, a generator converts the mechanical energy into electricity, delivering power to a load. By integrating a fuel cell stack with a microturbine, the fuel cell's exhaust drives the microturbine, generating additional power and increasing the system's electric efficiency. The fuel cell stack and microturbine effectively form a combined cycle.

### 1.1.4 Enhanced Fuel Cell Performance

Unlike commercial SOFC systems today, most (if not all) of which consist solely of an SOFC stack, hybrid systems pressurize the SOFC stack and place it between the air compressor and turbine. Importantly, pressurization enhances the fuel cell stack's performance, as higher pressures increase the fuel cell's reversible potential. The reversible potential of a fuel cell is defined as the potential difference between the fuel cell's electrodes in the absence of irreversibilities. In other words, the reversible potential represents an upper bound on the fuel cell's performance. The reversible potential depends on the pressure, temperature, and gas composition, and it is expressed using a formula called the Nernst equation. The Nernst potential of a fuel cell that electrochemically oxidizes $H_2$ is given by:

$$E_{\mathrm{N}} = -\frac{\Delta\overline{g}^{\circ}_{\mathrm{eoh}}(T)}{2F} + \frac{\overline{R}T}{2F}\ln\left(\frac{p_{\mathrm{H_2}}p_{\mathrm{O_2}}^{\frac{1}{2}}}{p_{\mathrm{H_2O}}p^{\circ\,\frac{1}{2}}}\right) \tag{1.1}$$

where $\Delta\overline{g}^{\circ}_{\mathrm{eoh}}(T)$ is the change in the molar Gibbs free energy of the oxidation reaction at standard pressure and temperature $T$, $F$ is Faraday's constant, $\overline{R}$ is the universal gas constant, $p_i$ is the partial pressure of species $i$, and $p^{\circ}$ is the standard pressure [26]. Figure 1.1 presents the Nernst potential as a function of pressure for various temperatures. The reversible potential increases significantly with pressure, particularly at lower pressure ratios (i.e., 1–10). As the pressure ratio increases, however, this benefit begins to taper off.

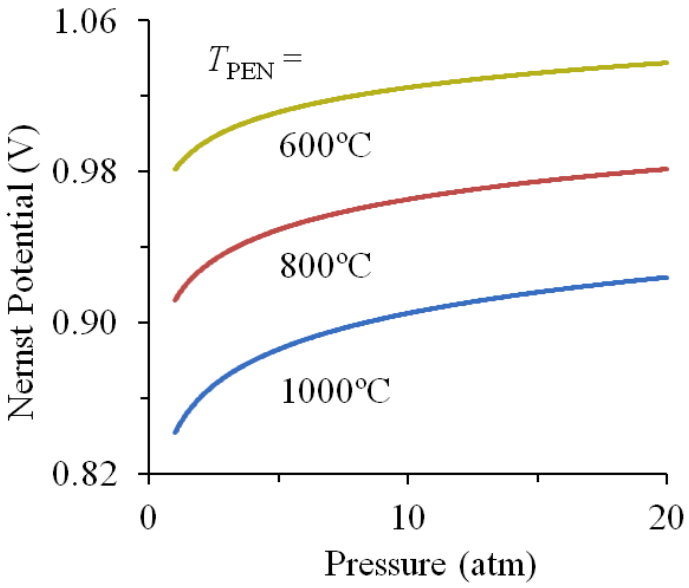


**Figure 1.1** The Nernst potential as a function of pressure and temperature. (The composition is assumed to be $y_{H_2} = 0.2631$, $y_{H_2O} = 0.4930$, and $y_{O_2} = 0.21$, based on a 30% pre-reformed $CH_4$-$H_2O$ mixture with a steam-to-carbon ratio of 2.5.)

### 1.1.5 Potential for Low $CO_2$ Emissions

Hybrid SOFC-MT systems have the potential to produce low $CO_2$ emissions. Environmentally sustainable power generation is becoming increasingly important, particularly as the U.S. Environmental Protection Agency (EPA) proposed $CO_2$ emission standards for existing, modified/reconstructed, and new power pants in the past few years [27–29]. By cogenerating electricity and thermal energy from the same fuel source, hybrid systems have the potential to achieve low $CO_2$ emissions. Cogeneration reduces a system's dependence on conventional heating systems, such as coal and natural gas-fueled boilers. By minimizing their dependence on conventional heating systems, hybrid systems effectively reduce their $CO_2$ emissions and fuel consumption. Second, by eliminating losses associated with transmitting and distributing electricity long distances, hybrid systems effectively increase their electric efficiency. Higher electric efficiency, in turn, reduces $CO_2$ emissions and primary energy consumption. Enhancing the fuel cell's reversible potential further improves the fuel cell's electric efficiency. Other pollutants, such as $NO_x$ and $SO_x$, fall well below those of more conventional systems. Fuel cells emit between 0.011–0.016 $lb_m$ $NO_x$/MWh (based on the sys-

tem's combined electricity and thermal output). For comparison, a reciprocating internal combustion engine emits between 0.013–0.17 $lb_m$ $NO_x$/MWh due to its higher combustion temperature. Solid oxide fuel cells emit negligible sulfur, as the natural gas is desulfurized prior to entering the fuel cell stack. Uncontrolled coal-fired plants, on the other hand, emit between 0.49–1.9 $lb_m$/MMBtu (HHV) [5]. Thus, $NO_x$ and $SO_x$ are considered to be insignificant.

It bears mentioning that hybrid systems, while having the potential to achieve low emissions, face certain environmental challenges. In particular, SOFC systems reform natural gas, which produces $CO_2$ as a byproduct. Hybrid systems also convert CO exiting the fuel cell stack into $CO_2$ in the combustor, further increasing emissions. Previous studies investigating the life cycle environmental impact of non-hybrid SOFC systems indicate that $CO_2$ emissions may, indeed, be significant during their use phase [30, 31]. Hybrid systems have the potential to overcome these issues by operating at relatively high electric and overall efficiencies, but further work is needed. While the present study does not address the hybrid system's environmental impact across its entire life cycle, it does compare the hybrid system's emissions to those of more conventional systems during use. The present study also compares the hybrid system's emissions to the recently proposed EPA standard for new combustion turbines. The EPA standard serves as a benchmark for future power generation.

### 1.1.6 Novel but Feasible

Despite the infancy of hybrid systems, these systems have been demonstrated experimentally. The National Fuel Cell Research Center at the University of California, Irvine tested a 220 kW SOFC-gas turbine (GT) hybrid system developed by Siemens Westinghouse in the early 2000s. The system successfully started, and the experimental results agreed well with researchers' simulation results [32–35]. FuelCell Energy, Inc. developed a hybrid system consisting of a molten carbonate fuel cell stack. During factory testing, the hybrid system generated more than 320 kW of power at an electric efficiency of 56% (LHV) [36]. Non-hybrid systems, on the other hand, which consist of a fuel cell stack as their sole power source, are being developed commercially. Several U.S. companies are developing non-hybrid

SOFC systems for various applications. Bloom Energy has developed the Energy Server, providing kW-scale baseload power to customers in retail, manufacturing, biotechnology, government, and other markets [37, 38]. Acumentrics Holding Corporation and Protonex have both developed SOFC systems for remote power applications [39, 40]. Microturbines, a more established technology, have experienced commercial success as well. Capstone Turbine Corporation and FlexEnergy, two leading microturbine manufacturers, have developed systems for a wide range of applications, including oil and gas operations, manufacturing, and waste management [41, 42]. The next sections describe the basic workings of solid oxide fuel cells and microturbines.

## 1.2 OVERVIEW OF SOLID OXIDE FUEL CELLS

### 1.2.1 Basic Features

Fuel cells consist of two electronically conductive structures, called electrodes, and an ionically conductive middle layer, called the electrolyte. Figure 1.2 illustrates the basic structure and operation of a fuel cell. The electrodes are called the anode and the cathode. Reactants are admitted into the flow channels, and the intermediate electrodes and electrolyte preclude direct mixing of the reactants. Instead, the reactants participate in electrochemical reactions along the fuel cell's flow path by diffusing through the electrodes to the electrode-electrolyte interfaces. At these interfaces, called triple-phase boundaries, catalyst-driven reactions occur. These reactions release electrons, providing electric current to an external circuit. In SOFCs, charge is transported across the electrolyte by $O^{2-}$ ions, while in other types of fuel cells (such as polymer electrolyte membrane fuel cells (PEMFCs) and phosphoric acid fuel cells (PAFCs), charge is transported by $H^{+}$ ions. The interconnect connects adjacent fuel cells together to form a fuel cell stack. The interconnect is electronically conducting, facilitating current flow through the stack.

Fuel cells are generally characterized by their electrolyte material. SOFCs consist of a ceramic electrolyte, which is commonly yttria-stabilized zirconia ($Y_2O_3$-stabilized $ZrO_2$, or

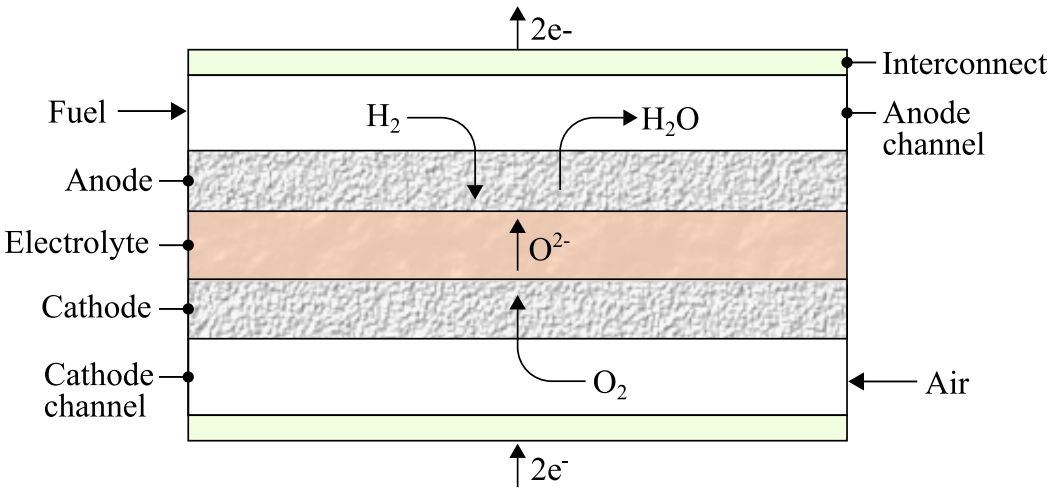


**Figure 1.2** Basic structure and operation of a fuel cell.

YSZ) [26, 43–45]. Yttria is used as the dopant to increase the number of oxygen vacancies in the electrolyte, thereby improving the material's ionic conductivity [26, 43]. High-temperature SOFCs operate between 600 and 1000°C. Such a high operating temperature greatly improves the conductivity of YSZ [43]. Moreover, SOFCs permit greater fuel flexibility than low-temperature, acid-electrolyte fuel cells, such as PEMFCs and PAFCs. SOFCs use a Ni catalyst to facilitate the electrochemical reaction at the anode, instead of Pt, as used in PEMFCs and PAFCs [43]. The use of Ni permits SOFCs to admit $CH_4$ and CO into the fuel channel, converting these species into $H_2$ through the methane steam reforming and water-gas shift reactions. The effectiveness of Ni-YSZ as a catalyst for the methane steam reforming reaction and water-gas shift reaction is suggested by experimental studies [46, 47]. SOFCs are even capable of operating on coal syngas [48]. Lower-temperature fuel cells, on the other hand, cannot tolerate CO. Carbon monoxide absorbs onto Pt, inhibiting the electrochemical reactions [43].

### 1.2.2 Electrode Reactions

SOFCs electrochemically oxidize $H_2$ to generate power. Hydrogen is either produced internally (from reforming $CH_4$ inside the fuel cell) or externally (from reforming in a separate chemical reactor). Air is admitted into the cathode channel. Oxygen is reduced at the cathode-electrolyte interface, producing $O^{2-}$ ions (Fig. 1.2). The $O^{2-}$ ions diffuse through the electrolyte to the anode-electrolyte interface, where they react with $H_2$ to produce electricity, steam, and thermal energy. The triple-phase boundary is the point of contact between the electrode, electrolyte, and reactants; it is where the electrochemical reactions occur [43–45]. Due to their various functions, the electrodes in an SOFC consist of dual layers. The first layer is located near the electrolyte and facilitates the electrochemical reactions. This layer is thin, finely porous, catalytic, and consists of many triple-phase boundary reaction sites. The second layer is located on top of the first layer. The second layer is thick, protective, mechanically supportive, electronically conductive, and highly porous for gas transport [43]. The following electrode reactions occur in an SOFC [26, 43–45]:

$$\text{Anode Reaction:} \qquad H_2 + O^{2-} \longrightarrow H_2O + 2\,e^- \tag{1.2}$$

$$\text{Cathode Reaction:} \qquad \tfrac{1}{2}\,O_2 + 2\,e^- \longrightarrow O^{2-} \tag{1.3}$$

Each of the electrode reactions constitutes a half-reaction. Oxygen is reduced at the cathode-electrolyte interface, and $H_2$ is oxidized at the anode-electrolyte interface. The overall reaction is given by:

$$H_2 + \tfrac{1}{2}\,O_2 \longrightarrow H_2O \quad \left(\Delta\bar{h}^{\circ}_{298.15} = -241.8\ \frac{\text{kJ}}{\text{mol}}\right) \tag{1.4}$$

The heat of reaction, $\Delta\bar{h}^{\circ}_{298.15}$, is provided above at 1 atm and 298.15 K [49]. The negative heat of reaction indicates that the electrochemical oxidation reaction is exothermic.

It would seem that CO could be directly oxidized by air through a process similar to that of $H_2$, as discussed above. This possibility, however, is not likely. According to electrochemical impedance spectroscopy data, the reaction kinetics of $H_2$ oxidation are dominant over those of CO in the presence of a $H_2$-$H_2O$-CO-$CO_2$ fuel mixture. In fact, the electrochemical oxidation of $H_2$ on Ni-YSZ cermet occurs approximately two to three times faster than that

of CO. Thus, CO is more likely to participate in the water-gas shift reaction than be electrochemically oxidized. The slower electrochemical oxidation rate of CO compared to that of $H_2$ seems to be related to mass-transfer and charge-transfer resistance [50]. In general, direct oxidation of CO is not considered to be a significant source of electric current.

### 1.2.3 Fuel Reforming

SOFCs produce additional $H_2$ through a conversion process called fuel reforming. Fuel reforming is the conversion of a hydrocarbon fuel into $H_2$ [43, 44]. Methods of fuel reforming include steam reforming (involving a reaction between a hydrocarbon fuel and $H_2O$), partial oxidation reforming (incomplete combustion of a hydrocarbon fuel), and autothermal reforming (a combination of steam reforming and partial oxidation reforming). Methane steam reforming, in particular, is given by the following chemical reaction [26, 43]:

$$\mathrm{CH_4 + H_2O \longrightarrow CO + 3\,H_2} \quad \left(\Delta\overline{h}^{\circ}_{298.15} = 206.4\ \frac{\mathrm{kJ}}{\mathrm{mol}}\right) \tag{1.5}$$

The methane stream reforming reaction is endothermic, as indicated by the positive heat of reaction.

Each of the reforming methods possess advantages and disadvantages. Steam reforming is advantageous because it does not introduce additional air into the fuel channel. The presence of air in the fuel channel reduces the Nernst potential by diluting $H_2$ with $N_2$. Steam reforming, however, requires a steam supply, which increases system complexity [26]. Steam reforming also requires a supply of thermal energy, as the methane steam reforming reaction is highly endothermic. The requisite thermal energy could come from combustion of fresh fuel, or from an afterburner that combusts the fuel cell's exhaust [43]. Partial oxidation reforming, on the other hand, does not require steam, but it does require oxidant, which lowers the Nernst potential, assuming that air is used. Partial oxidation reforming is also exothermic, which means that thermal energy from the electrochemical oxidation reaction cannot be used by the reforming reaction, as it could in the case of steam reforming [26]. Autothermal reforming is advantageous because it is energy neutral, meaning that its heat of reaction is zero, thus simplifying the thermal management system [26, 43]. Autothermal reforming, however, requires an oxidant, which (as before) lowers the Nernst potential.

Fuel reforming occurs either external or internal to the fuel cell stack. External fuel reforming occurs in a separate chemical reactor, whereas internal fuel reforming occurs on a catalyst surface inside the fuel cell. External reforming is particularly useful for producing the pure $H_2$ required by low-temperature fuel cells, such as PEMFs and PAFCs, as these fuel cells are CO-intolerant. In these systems, the fuel is reformed externally before passing through water-gas shift reactors and undergoing further CO clean-up. The CO content is thereby reduced to an acceptable level before entering the fuel cell stack [26, 43]. Internal reforming, on the other hand, is suitable for high-temperature fuel cells, as these fuel cells are tolerant of CO. Internal reforming is the steam reformation of $CH_4$ into $H_2$ inside the fuel cell itself. Internal reforming presents a number of benefits, including the use of thermal energy from the oxidation reaction to drive the endothermic methane steam reforming reaction, thus improving the system's overall efficiency by requiring less cooling air. Internal steam reforming also reduces (or eliminates) the need for outside steam by using the steam produced by the oxidation reaction inside the fuel cell [26]. Moreover, internal and external reforming are not mutually exclusive. In particular, many system adopt pre-reforming. Pre-reforming is the steam reformation of heavier hydrocarbons (possibly including $CH_4$) into $H_2$ prior to entering the fuel cell stack. The purpose of pre-reforming is to prevent heavier hydrocarbons in the fuel from forming solid carbon inside system components. Carbon formation is undesirable because it fouls the Ni catalyst [26, 51]. Various fuel types may be pre-reformed prior to entering the SOFC stack, including liquid petroleum gas, naptha, diesel fuel, and ethanol [51].

Internal reforming is classified as either direct or indirect. Direct internal reforming allows for more synergistic operation of the fuel cell, as it involves the steam reformation of $CH_4$ inside the anode channel itself (Fig. 1.3a). In the case of SOFCs, reformation occurs directly on the anode, driven by the Ni catalyst. The reforming reaction utilizes steam and thermal energy from the electrochemical reaction, thus improving the system's overall efficiency. Indirect internal reforming, on the other hand, involves the steam reformation of $CH_4$ in a compartment separate from the anode but still thermally connected to the fuel cell stack (Fig. 1.3b). The reforming reaction and electrochemical reactions do not chemically interact, as in the case of indirect reforming, necessitating that steam be provided externally

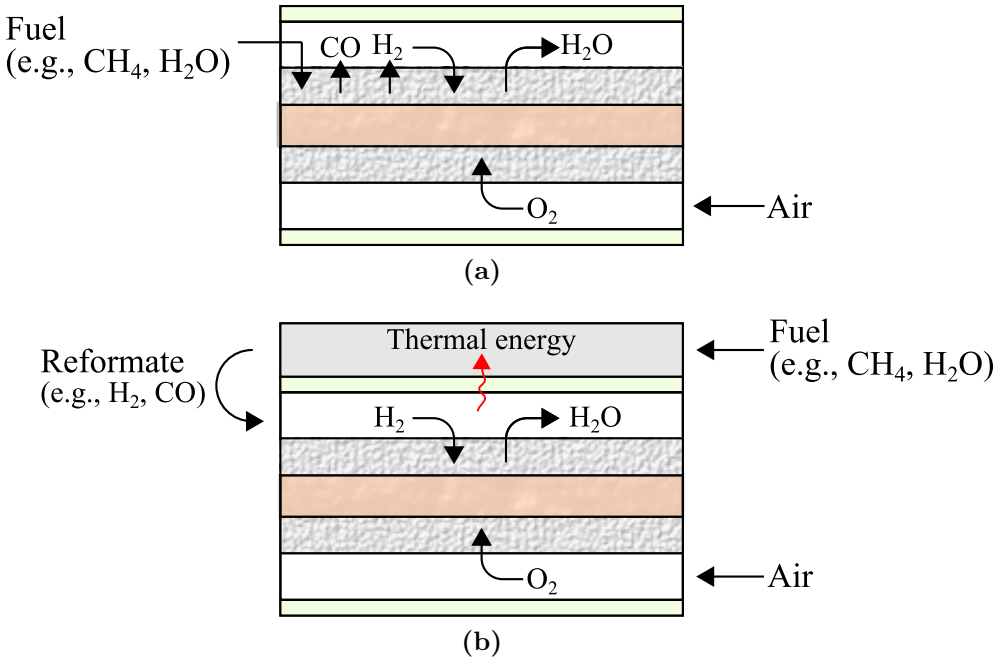


**Figure 1.3** Internal reforming configurations: (a) direct internal reforming, (b) indirect internal reforming (adapted from [52]).

(e.g., recirculated from the anode channel). Nonetheless, thermal energy from the fuel cell is transferred to the reforming reaction through the compartment wall [26].

### 1.2.4 Water-Gas Shift Reaction

The water-gas shift reaction converts part of the CO produced by the methane steam reforming reaction into $H_2$. The forward water-gas shift reaction proceeds as follows [43]:

$$\mathrm{CO} + \mathrm{H_2O} \longrightarrow \mathrm{CO_2} + \mathrm{H_2} \quad \left(\Delta\overline{h}^{\circ}_{298.15} = -41.2\ \frac{\mathrm{kJ}}{\mathrm{mol}}\right) \tag{1.6}$$

The forward water-gas shift reaction is slightly exothermic, thus helping to drive the steam reforming reaction. Furthermore, it has been found that the water-gas shift reaction reaches equilibrium in the presence of a $CH_4$-containing fuel undergoing steam reformation over Ni-YSZ cermet at a temperature of approximately 900°C. One possible explanation for this phenomenon is that the presence of CO brought about by the methane steam reforming

reaction catalyzes the water-gas shift reaction [47]. Experimental data further indicates that the water-gas shift reaction, when occurring alongside the methane steam reforming reaction over Ni-YSZ, reaches equilibrium across a wide temperature range, 400°C–1000°C [53]. In the present study, the water-gas shift reaction is assumed to be in equilibrium.

## 1.3 OVERVIEW OF MICROTURBINES

Microturbines are small gas turbines, generating between 28 and 333 kW of power. General characteristics of microturbines are summarized in Table 1.1. Microturbines operate at approximately 30% (LHV) electric efficiency [16, 24]. Similar to fuel cells, microturbines are modular. That is, generators may be installed incrementally. Installing multiple units not only provides flexibility in adjusting power output, but it also improves power reliability, as nearby generators can serve as backup if one unit fails [5]. Microturbines are furthermore capable of load-following. The load-following methodology depends on the number of microturbines installed. If multiple units are installed, then the net power may be adjusted by turning on or off certain microturbines. If only a single unit is installed, then the power may be varied by changing the shaft speed and turbine inlet temperature. Reducing the shaft speed reduces the air mass flow rate, thereby reducing the power. Reducing the turbine inlet temperature also reduces the power [5]. However, the electric efficiency of the gas turbine decreases as the firing temperature decreases.

Microturbines are well-suited for various applications. The exhaust temperature of microturbines typically ranges between 256°C and 325°C. Byproduct thermal energy may be used in absorption chilling, steam generation, boiler feedwater preheating, hot water heating, and trigeneration applications [16, 24]. In addition, microturbines are well-suited for biogas recovery, resource recovery, and remote power. Biogas recovery uses methane obtained from the degradation of organic matter for power generation. Landfill gas and anaerobic digester gas, if properly cleaned, may serve as fuel for a microturbine as well. Resource recovery refers to the use of microturbines in oil production and coal mining. In these applications, microturbines drive pumps necessary for oil and coal operations, and the microturbines op-

**Table 1.1** General characteristics of microturbines.

| | |
|---|---|
| Power | 28–333 kW |
| Efficiency | 30% (LHV) |
| Operation | Baseload or load-following |
| Applications | Distributed generation<br>Combined heat and power<br>Biogas recovery<br>Resource recovery<br>Remote power |
| Fuel | Gaseous (natural gas, propane, landfill, digester)<br>Liquid (diesel, aviation, kerosene) |
| Cycle | Brayton |

erate on the methane or natural gas produced as a byproduct [5, 54]. In addition to gaseous fuels, microturbines can operate on propane, diesel, aviation, and kerosene [24].

Thermodynamically, nearly all microturbines operate on the Brayton cycle. Figure 1.4 presents a schematic of a Brayton cycle. The basic components of a microturbine include the compressor, combustor, turbine, and recuperator. The compressor compresses ambient air entering the system. The compressor and turbine are both radial-flow devices, as these devices achieve modest efficiencies at low air flow rates. The recuperator preheats the air entering the combustor, reducing the amount of fuel required in the combustor. The fuel is then mixed with the air and combusted in the combustor, producing thermal energy to drive the turbine. The turbine generates sufficient power to both drive the compressor and serve a load. Before exiting the system, the exhaust thermal energy is used to preheat the incoming air, and any remaining thermal energy is recovered in the heat recovery heat exchanger. It should be mentioned that the pressure losses in the heat recovery heat exchanger (i.e., non-zero back-pressure) and inlet air filters (i.e., non-zero inlet pressure) reduce the system's efficiency. Ambient temperature and altitude also impact a microturbine's performance [5].

In order to generate 60 Hz AC, microturbines typically adopt one of two strategies. In the first strategy (shown in Fig. 1.4), the shaft (which may be rotating as fast as 60,000 rpm)

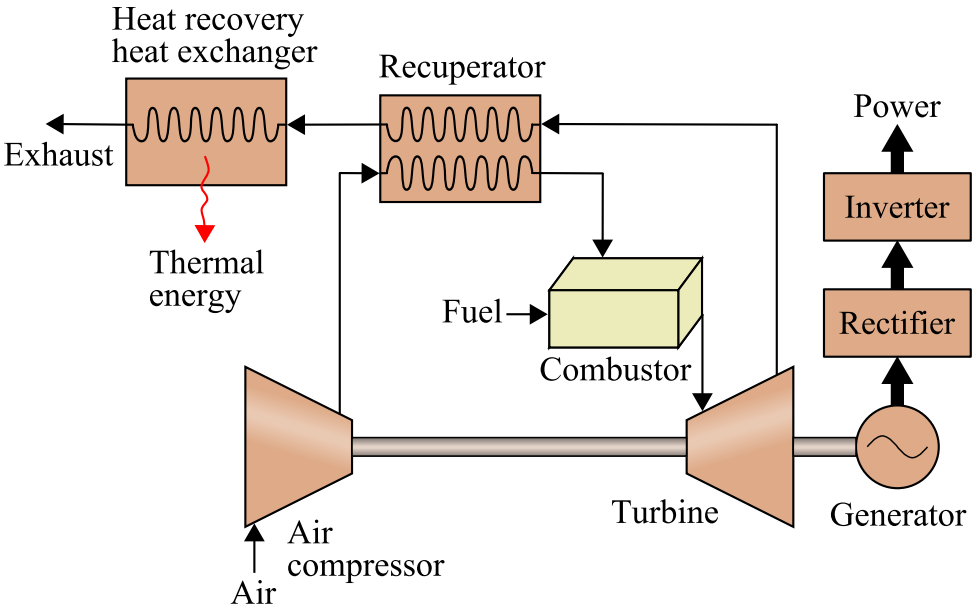


**Figure 1.4** Schematic of a microturbine (adapted from [16, 49, 55]).

drives a high-speed generator. The rectifier then converts the generator's high-frequency output into DC power. The inverter finally converts the DC power into 60 Hz AC. Capstone Turbine Corporation adopts such an approach. In the second strategy, a gearbox reduces the shaft speed to 3,600 rpm. The shaft then drives a synchronous generator, precluding the need for a rectifier or inverter. FlexEnergy adopts such a strategy [5]. Two-shaft microturbines (not yet commercial) will likely also adopt this same strategy. That is, the power turbine will likely connect to a synchronous generator through a gearbox, and the gasifier turbine will rotate on a different shaft, and at a different (slower) speed [55]. Capstone is currently developing a two-shaft design that is projected to operate at 42% efficiency (LHV, gross output) [5].

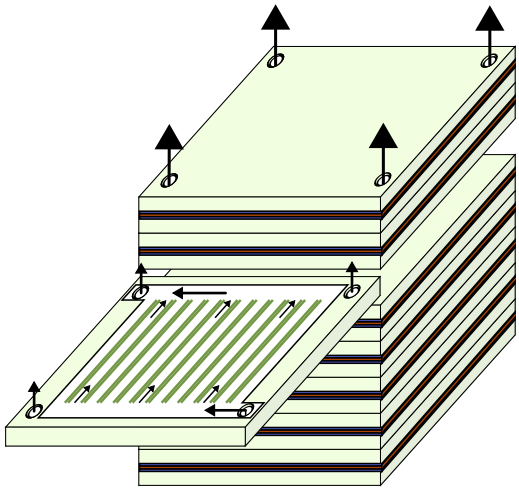

**Figure 1.5** SOFC stack showing individual SOFC.

## 1.4 CONTRIBUTIONS

The present work develops an SOFC-MT model. Specifically, the present work develops a one-dimensional, numerical SOFC stack model, as presented in Fig. 1.5. The fuel cell model consists of balance equations discretized in space (along the flow direction) and time. The stack's performance is obtained by linearly scaling the fuel cell's performance up to the stack level. The fuel cell stack is furthermore integrated with two overall system models. The hybrid system, presented in Figure 1.6, integrates the fuel cell stack with a microturbine. The fuel and air react electrochemically inside the fuel cell stack, and unused fuel is combusted in the auxiliary combustor. The combustion products drive the microturbine, generating additional power, and the turbine's exhaust preheats the incoming fuel and air. The remaining thermal energy is recovered in the heat recovery heat exchanger. For comparison, the present work also models a non-hybrid system (shown in Fig. 1.7). The non-hybrid system relies on the fuel cell stack as its sole power source. The fuel cell stack operates at near-atmospheric pressure, and the exhaust exits the system soon after leaving the auxiliary combustor. Both systems consume natural gas, which is desulfurized and pre-reformed prior to entering the fuel cell stack. A fraction of the anode's exhaust is returned to the pre-reformer's inlet, supplying steam and thermal energy to the fuel feed.

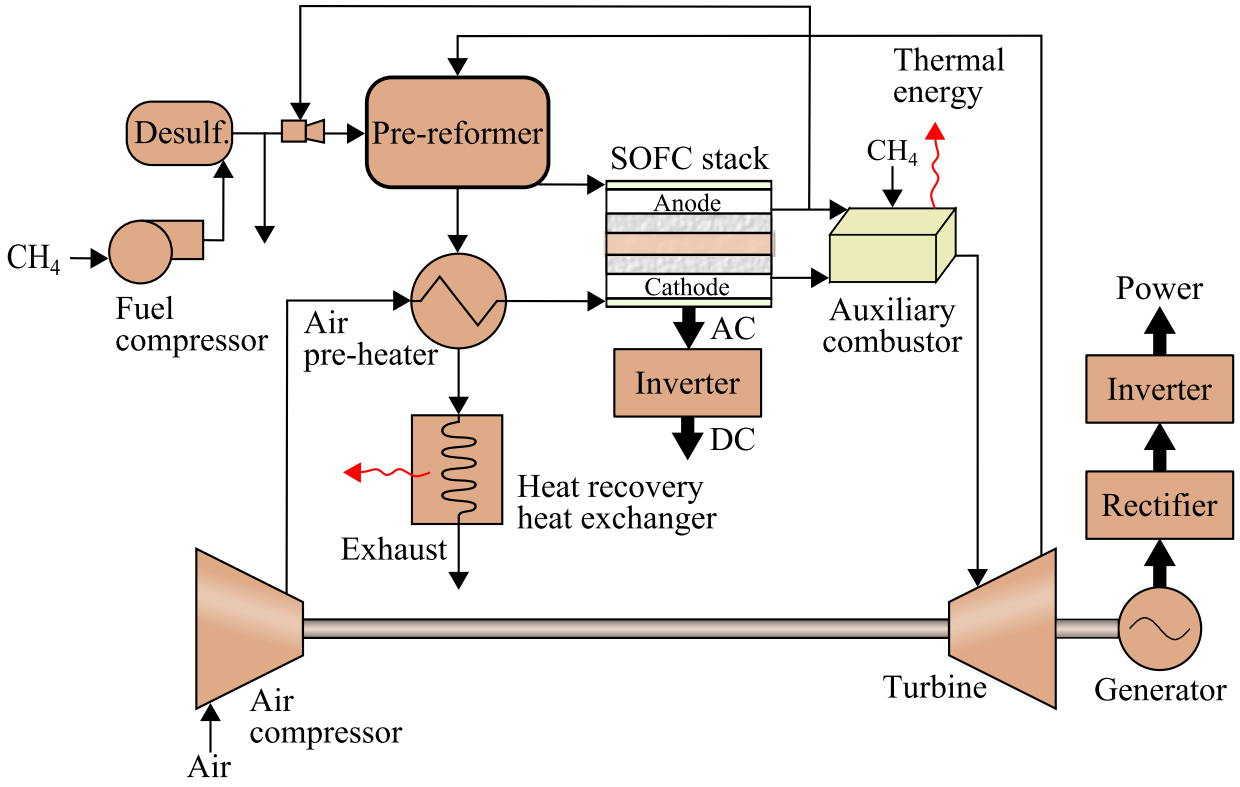


**Figure 1.6** Hybrid system schematic.

The present study contributes to a number of areas involving the fuel cell stack and system models. Specifically, the present study (i) simulates the SOFC stack's dynamic response to control variables commonly encountered in hybrid systems, (ii) investigates settling times associated with the charge double layer under various operating conditions, (iii) conducts exergy and economic analyses of the hybrid and non-hybrid systems, and (iv) conducts an environmental analysis of the hybrid and non-hybrid systems. The fuel cell stack model allows for simulations on multiple timescales, capturing electrochemical, mass flow, and thermal processes. The fuel cell stack's behavior on these different timescales dictates the effectiveness of a control strategy. The stack model also includes the so-called the "charge double layer" to simulate electrochemical dynamics. The system models, on the other hand, calculate changes in the fluid's composition and temperature as the fuel cell stack interacts with the BoP components. The thermodynamic models also calculate the exergy flows, as well

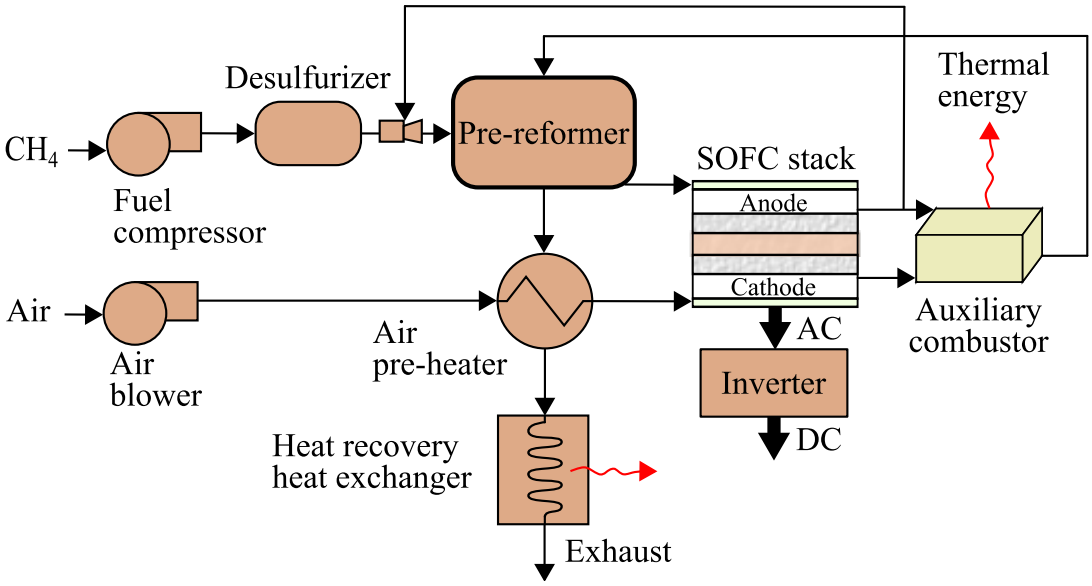


**Figure 1.7** Non-hybrid system schematic (adapted from [56]).

as the systems' electric and overall efficiencies. The systems' economic and environmental performances depend on the systems' electric and overall efficiencies. The present study's contributions are discussed in more detail below.

### 1.4.1 Dynamic Response to Control Variables

The present study investigates the uncontrolled (open-loop) response of the average PEN temperature, fuel utilization, and SOFC power to step changes in the inlet fuel flow rate, current density (or voltage), and inlet air flow rate on different timescales. The former set of variables typically requires control in an SOFC-GT system for safety and efficiency reasons.[1] The latter variables are often manipulated to achieve control, as manipulation of these variables is feasible and can also induce significant changes in the controlled variables [22,23,57–59]. Physical processes inside SOFCs are tightly coupled, and choosing the proper combination of controlled and manipulated variables inside the SOFC stack is essential to achieving safe and efficient dynamic response. The present study identifies pairs of control

[1]It should be reiterated that microturbines (MTs) form a subcategory of gas turbines (GTs).

variables (i.e., pairs of controlled and manipulated variables) that minimize interdependence, where interdependence may be defined as the inability of a manipulated variable to effectively control a targeted variable, unless control of another variable(s) is implemented. The reason for minimizing interdependence is to reduce the risk of oscillations between control levels in a cascade controller [23]. Consideration is also given in this study to the time required for the SOFC to meet a power demand. Faster settling times are desired, as they enable a system to more quickly meet demand.

The fuel cell model developed in the present study is a 1-D, planar, co-flow model that includes direct internal methane steam reforming, water-gas shift, and $H_2$ oxidation reactions. The model is subdivided into the fuel cell's main components, consisting of the fuel and air channels, the PEN (positive electrode-electrolyte-negative electrode) structure, and the fuel and air-side interconnects. The fuel cell's main components are further discretized along the flow direction, and the balance equations are applied numerically to each control volume. The governing equations consist of charge, species mass, energy, and momentum balances, each modeled dynamically. The performance of a single fuel cell is obtained by linearly scaling the performance of a single channel by the number of channels in the fuel cell, and the performance of the stack is obtained by linearly scaling the performance of a single fuel cell to the stack level. During dynamic simulations, emphasis is placed on SOFC stack (rather than system) behavior, and therefore, the balance-of-plant models are not considered. Neither are shaft speed dynamics considered (air flow is assumed to be instantaneous—this assumption may be likened to using an air bypass valve to adjust the air flow rate [58]).

### 1.4.2 Electrochemical Settling Time

Developing a fuel cell model that is both accurate and computationally efficient is important, especially when incorporating the fuel cell model into a larger, controlled system. While electrochemical processes inside SOFCs are often assumed to be steady-state, few (if any) studies have investigated the validity of this assumption across a wide range of operating conditions. The present study investigates the assumption of steady-state vs. dynamic electrochemistry under various operating conditions. In particular, the SOFC model described above incorpo-

rates electrochemical dynamics via an equivalent circuit. The charge double layer, which is a (dual) layer of positive and negative charge that accumulates along the electrode-electrolyte interface, is modeled as a capacitor in the equivalent circuit. The circuit represents each polarization (ohmic, activation, and concentration) as an equivalent resistance, and the Nernst potential is represented as a voltage source. Combining these various elements together, the electrochemical model expresses the fuel cell's operating voltage as a function of the charge double layer capacitance, time, and additional quantities.

In order to determine the fuel cell's electrochemical settling time under various operating conditions, baseline operating conditions are first defined, followed by consideration of minor and major deviations from the baseline case. Under each set of operating conditions, the SOFC stack model is subjected to step changes in load (current density or power demand), and proportional-integral (PI) control is also considered. Based on the results herein, the charge double layer influences the SOFC stack's settling time significantly under the following conditions: (i) the activation and concentration polarizations are significantly increased, or (ii) a large value of the double layer capacitance is assumed. Under normal (baseline) operation, on the other hand, the charge double layer effect diminishes within milliseconds (including under PI control). It seems reasonable, then, to neglect the charge double layer under normal operation. Careful consideration, however, should be given to potential variations in operation or material properties that may give rise to longer electrochemical settling times.

### 1.4.3 Exergy and Economic Analyses

The present work evaluates the economic competitiveness of hybrid systems. Hybrid systems currently remain in the demonstration phase. The National Fuel Cell Research Center at the University of California, Irvine [33] and FuelCell Energy, Inc. [36] have both successfully demonstrated hybrid systems, but these systems have yet to become commercial. Non-hybrid systems, on the other hand, are commercial. Bloom Energy [37], Acumentrics Holding Corporation [39], and Protonex [40] currently develop non-hybrid systems. Moreover, a hybrid system's economic competitiveness depends on numerous factors, including capital

costs and fuel costs. Hybrid systems operate at especially high electric efficiencies, thus lowering their fuel costs. Higher capital costs, however, may negate these lower fuel costs. Hybrid systems also tend to produce less thermal energy than atmospheric systems due to their lower exhaust temperature, potentially making them less effective CHP systems. The present study calculates the levelized cost of electricity (LCOE) of the hybrid and non-hybrid systems.

In addition to evaluating the systems' economic performance, the present study also performs exergy analyses of the hybrid and non-hybrid systems. Previous studies have performed exergy analyses on large hybrid systems (1–300 MW) [60–62], but none have specifically compared small (kW-scale) hybrid and non-hybrid systems. The exergy analyses performed herein identify sources of inefficiency within each system. Such inefficiencies include exergy destruction and exergy loss. Exergy destruction is the reduction of work potential due to irreversibilities, such as heat transfer and spontaneous chemical reaction. Exergy loss is the departure of (unused) exergy from the system, which may be in the form of high-temperature exhaust or unused fuel. Minimizing exergy destruction and exergy loss is crucial to maximizing a system's exergetic efficiency, which indicates how effectively a system utilizes its inlet exergy. Higher exergetic efficiency is typically associated with better use of fuel, whereas lower exergetic efficiency indicates room for improvement. The present study compares the hybrid and non-hybrid systems in terms of their exergetic performance.

### 1.4.4 Environmental Analysis

The thermodynamic models also calculate the $CO_2$ emissions during the hybrid and non-hybrid systems' operation. The hybrid system's emissions are compared to those from the non-hybrid system. Emissions from these systems are also compared with those from more conventional technologies, including distributed generation systems, and coal and natural gas sources in the U.S. These existing, more mature technologies represent the status quo. Emissions from the hybrid and non-hybrid systems are also compared to the EPA's proposed regulations for new power plants. In particular, the EPA proposed regulations limiting the $CO_2$ emissions from new power plants, specifically targeting utility boilers, integrated gasi-

fication combined cycle power plants, and natural gas-fired stationary combustion turbines. These emission standards are provided on a rate basis ($lb_m$ $CO_2$/MWh). The EPA has also proposed regulations for modified, reconstructed, and existing power plants, although these regulations are more state and system-dependent than those proposed for new power plants [27–29]. The present study compares the hybrid and baseline systems' environmental performance to the EPA's proposed regulations on new combustion turbines.

## 1.5 SUMMARY

SOFCs and microturbines currently meet various energy needs. The motivation for pursuing SOFC-MT systems stems from the potential benefits of integrating an SOFC stack with a microturbine, including high electric efficiencies, enhanced fuel cell performance, and low $CO_2$ emissions. While non-hybrid systems are commercial, however, hybrid systems remain in the demonstration phase; hence, there is a need to better understand hybrid systems through modeling and simulation. In this regard, the present work makes several contributions. First, the present work investigates the open-loop response of the SOFC stack to load changes. Second, the present work investigates the electrochemical settling time of the SOFC stack. Third, the present work performs exergy and economic analyses of hybrid and non-hybrid systems. Lastly, the present work investigates the environmental performance of the hybrid and non-hybrid systems. The next chapter reviews the literature relevant to the aforementioned areas.

# 2.0 LITERATURE REVIEW

The literature on solid oxide fuel cells (SOFCs) spans many topics, ranging from microscale transport phenomena to system-level analysis. In accordance with the contributions discussed in Chapter 1, the literature reviewed in this chapter is divided into four categories. First, previous studies on hybrid SOFC-gas turbine (GT) control strategies are reviewed.[1] These studies indicate that a control strategy's choice of controlled and manipulated variables significantly influences the system's behavior. Second, the charge double layer is reviewed. Few studies have modeled the charge double layer, but the few that have provide insight into the fuel cell's behavior on short timescales. Third, previous exergy and economic analyses of SOFC systems are reviewed. Previous economic studies have focused largely on design and operation optimization. Exergy analyses are also briefly summarized. Lastly, the literature on SOFC economic performance is reviewed. Life cycle assessment (LCA) studies indicate that $CO_2$ emissions are significant during operation relative to other life cycle stages.

## 2.1 CONTROL STRATEGIES

The purpose of a controller is to maintain safe and efficient operation of a system. Safe and efficient operation is critical to successfully operating an SOFC system. Previous studies on hybrid systems have proposed various control strategies for meeting demand effectively. In particular, Martinez, et al. [23,63] proposed a control strategy for a locomotive SOFC-GT system. These authors developed a cascade control strategy that involved controlling a number of variables at varying levels of priority. At the highest priority, control of the average SOFC temperature proceeded by manipulating the air flow (or shaft speed). At a lower priority,

[1] As discussed in Chapter 1, microturbines (MTs) form a subcategory of gas turbines (GTs).

manipulating the SOFC voltage controlled the fuel utilization. At the lowest priority, control of system power was achieved by manipulating the inlet anode flow rate, and (on the same level) manipulating the combustor fuel flow controlled the turbine inlet temperature (thus influencing the system's efficiency). These authors found that the hybrid system followed the power demand reasonably well, although the controlled parameters sometimes exceeded their bounds. A major benefit of such a cascade controller is the minimization of interference between control loops, as lower levels are not pursued until the higher (safety-oriented) levels have been satisfied. Such a control scheme is also amenable to development in a conventional programming language, such as Fortran or C, to coincide with a model written in one of these or similar languages. A major challenge, however, is avoiding oscillations between the various levels (if the control loops operate on similar timescales). Changes in one level could provoke changes in another level due to the coupled nature of physical processes inside SOFCs.

Mueller, et al. [57] developed a control strategy that takes advantage of the synergism inherent in hybrid systems. In particular, the hybrid system manipulated the SOFC stack's current to simultaneously alter the SOFC power and the fuel flow rate exiting the stack. Changing the fuel flow rate helped to maintain a safe recuperator inlet temperature by reducing the exit combustor temperature. During a load change, the stack absorbed excessive thermal energy (resulting from increased current) as the shaft speed (cooling air) ramped up. Meanwhile, the gas turbine temporarily generated greater power than intended to compensate for delays in fuel delivery to the stack. Thus, one prime mover's strengths compensated for the other prime mover's shortcomings. For comparison, the authors developed a non-hybrid microturbine model, which maintained a desired recuperator inlet (turbine exit) temperature by maintaining a relatively constant fuel-to-air ratio in the combustor. The authors found that the non-hybrid system followed demand at a maximum rate of approximately 1 kW/s, whereas the hybrid system met an instantaneous 100 kW demand increase in only approximately 20 s. Thus, the hybrid system clearly exhibited superior performance.

Roberts and Brouwer [33] developed an SOFC-GT model based on a proof-of-concept prototype developed by Siemens Westinghouse and tested at the National Fuel Cell Research Center (University of California, Irvine). The system consisted of separate power and gasi-

fier turbines, as well as multiple combustors to heat the SOFC during start-up. The system operated on natural gas, which was fed directly to the SOFC stack and combustors. Bypass valves were used to control the SOFC stack's temperature. During start-up, the authors subjected the model and experimental system to identical control moves, including the repositioning of bypass valves and adjustment of the SOFC stack's fuel flow. The authors found that the power generated by the SOFC stack during start-up agreed well with the simulation results, as did the power generated by the turbine. The results differed slightly, however, during SOFC stack bypass valve repositioning. The authors attributed these discrepancies to inaccurate valve measurement. The authors also compared the steady-state temperatures of the hybrid model to those of the demonstration system, again finding reasonable agreement. Discrepancies in these results were attributed to the authors' modeling assumption of an adiabatic recuperator and adiabatic SOFC stack.

Stiller, et al. [22] developed a control strategy for a hybrid system model that involved manipulating the SOFC stack's current to control system power, system fuel flow to control the SOFC's fuel utilization, shaft speed (via the generator power) to control the system air flow, and the air flow setpoint to control the fuel cell's temperature. (Leucht, et. al. [58] also controlled fuel utilization by manipulating the fuel flow.) Predefined limits prevented the fuel utilization from falling outside the range 75%–90%, as too low fuel utilization could reduce the SOFC's efficiency significantly (potentially leading to excessively high afterburner and turbine inlet temperatures as well). Too high fuel utilization, on the other hand, could lead to harmful temperature gradients. The authors also specified a minimum SOFC voltage of 0.52 V, corresponding to the SOFC's maximum power output (or thereabouts). During simulation, the authors subjected the hybrid system to small (4.7%) and large (47%) step load changes. The authors found that the hybrid system responded in less than 1 min. to both types of load changes, which is relatively fast. The authors also subjected the system to various disturbances, including increased fuel cell ohmic resistance and system fuel flow overestimation, representing fuel cell degradation and sensor malfunction, respectively. The authors found that the average SOFC temperature remained stable following each disturbance, although slight changes in the average temperature occurred following each disturbance.

The foregoing studies, among others, have contributed substantially to the development of SOFC-MT control strategies. The present study differs from these studies, however, by focusing specifically on the open-loop response of variables in the SOFC stack. Processes within SOFCs are tightly coupled, and efficient system operation depends on proper operation of the SOFC stack. Thus, the present work identifies pairs of controlled and manipulated variables that facilitate cascade control. Chapter 7 further discusses possible control strategies that minimize interdependence, where interdependence may be defined as the inability of a manipulated variable to effectively control a targeted variable, unless control of another variable(s) is implemented. Minimizing interdependence reduces the risk of oscillations between control levels in a cascade controller (see Martinez, et al. [23]). It should be reiterated that while many of the foregoing studies implemented proportional-integral-derivative (PID) controllers, the present study considers only the open-loop response of control variables. Results from this study are intended to inform control decisions at the system level.

## 2.2 CHARGE DOUBLE LAYER

Numerous books on SOFC modeling present equivalent circuits that are useful for incorporating the charge double layer into fuel cell models. O'Hayre, et al., for instance, [43] discuss an equivalent circuit model based (qualitatively) on electrochemical impedance spectroscopy data. In this circuit, the charge double layer is represented as a capacitor, the ohmic resistance and reaction kinetics are both represented as resistors, and species diffusion through the electrodes is represented as a Warburg element. The properties of each of these elements are obtained from Nyquist plots. A Nyquist plot displays the fuel cell's impedance in the complex plane. Each equivalent circuit element (or polarization) produces a unique pattern on the Nyquist plot. Ohmic resistance, for instance, appears as a single point on the Nyquist plot. Hence, its value is simply read off of the real axis. Activation kinetics and the charge double layer, on the other hand, appear together as semi-circles on the Nyquist plot. The Warburg element may appear linear on the Nyquist plot, if the diffusion thickness is sufficiently large, or it may appear circular, if the diffusion thickness is relatively small.

Nehrir and Wang [64], Gemmen [65], and Larminie and Dicks [26] present similar equivalent circuit models. These references, however, do not provide as extensive of a discussion on electrochemical impedance spectroscopy data as that found in O'Hayre, et al. [43].

Prior modeling studies have investigated the charge double layer. Qi, et al. [66] developed a state-space SOFC model that incorporated the charge double layer via an equivalent circuit. The model tracked changes in the current, operating voltage, reaction rates, and species diffusion rates on the millisecond timescale in response to step changes in the load resistance and species partial pressures. The authors found that the ohmic resistance responded instantaneously to a step change in the load resistance. The charge double layer, on the other hand, exhibited a slower (but still millisecond-scale) response. The authors also investigated the influence of diffusion resistance through the electrodes and boundary layers on SOFC performance. The authors found that increasing the diffusion layer thickness from 1 mm to 3 mm significantly increased the diffusion rate's settling time due to increased concentration loss. As expected, increasing the diffusion layer thickness also decreased the SOFC's output voltage. Qi, et al. [67] used the same equivalent circuit in a tubular SOFC model (discretized axially and radially) to investigate the responses of the fuel cell's operating voltage, current, and exit gas properties (i.e, exit temperature, pressure, composition, and flow velocities) to step changes in the load resistance and inlet gas properties. The authors found that the charge double layer, again, diminished within milliseconds. The authors also found that the inlet flow velocity minimally influenced the fuel cell's dynamic response, whereas the inlet pressure and temperature had a larger influence.

Wang and Nehrir [68] developed a lumped-parameter SOFC model that tracked changes in the operating voltage on millisecond, second, and minute timescales in response to step changes in the current. These authors used an equivalent circuit to combine the charge double layer with the ohmic, activation, and concentration polarizations. The authors varied the charge double layer capacitance value between 0.4 F and 4 F. Similar to Qi, et al. [66, 67], these authors found that the double layer polarization settled in a span of milliseconds following a step change in load. The mass flow dynamics, on the other hand, settled in a span of seconds following a step change in load. The thermal dynamics lasted the longest, settling on the minute timescale. Wang and Nehrir [69] furthermore experimentally verified

a similar equivalent circuit model. The authors compared their results to those obtained from an SR-12 Avista Labs PEM fuel cell. The authors imposed step changes in current and tracked the operating voltage on short (electrochemical) and long (thermal) timescales. The simulation results agreed reasonably well with the experimental results in terms of settling times.

The foregoing studies indicate that electrochemical dynamics tend to diminish within milliseconds following a load change. Few (if any) studies, however, have investigated this assumption across a wide range of operating conditions. Many studies have investigated the dynamic response of an SOFC on second and minute timescales, but these fuel cell models do not include the charge double layer [70–81]. The present study investigates electrochemical dynamics under various operating conditions to determine if the electrochemical settling time could possibly last seconds (or longer). It bears mentioning that the present model is a macroscale model that incorporates the charge double layer (a microscale phenomenon) via an equivalent circuit (a macroscale representation). As such, the present model does not capture the same level of detail as a microscale model, particularly in terms of elementary reaction chemistry, mass transfer through the PEN structure, and electric potential distributions. (Further information on these phenomena may be found in Refs. [82–86], among others). Nevertheless, the use of an equivalent circuit permits (computationally) investigation into the dynamic behavior of the charge double layer under a wide range of operating conditions, involving not only dynamic electrochemistry but also dynamic mass flow, energy, and momentum balances, and on longer-than-usual timescales (greater than milliseconds, which is the charge double layer's characteristic time). Thus, the present model is considered suitable for the task at hand.

## 2.3 EXERGETIC AND ECONOMIC ANALYSES

Exergy represents the quality of energy. Unlike the first law of thermodynamics, which considers only the quantity of energy, exergy considers the usefulness (or value) of energy [87]. Moran, et al. define exergy as follows:

> Exergy is the maximum theoretical work obtainable from an *overall* system consisting of a system and the environment as the system comes into equilibrium with the environment (passes to the dead state). [49, p. 362, emphasis in the original]

Calise, et al. [61] performed perhaps one of the earliest exergy studies on a hybrid system. The authors performed an exergy analysis of a 1.5 MW hybrid system consisting of an internal reforming fuel cell stack, gasifier turbine, power turbine, and balance-of-plant components. During operation, the authors found that the largest exergy destruction occurred in the SOFC stack, followed by the afterburner. The authors varied the fuel cell's current density and operating pressure to improve the system's performance. They found that decreasing the current density reduced the system's total exergy destruction, thus increasing the system's electric and overall efficiencies. Increasing the fuel cell's operating pressure further improved the system's performance, but only up to a certain pressure. Gandiglio, et al. [60] performed an exergy analysis of a large (280 MW) hybrid system. Similar to Calise, et al. [61], these authors found that the largest exergy destruction occurred in the SOFC stack and afterburner. Calise, et al. [62] also performed an exergy analysis of a hybrid system, this time considering both full-load and part-load operation. The authors found that the system achieved an exergetic efficiency of 62.6% at full-load operation. The system's part-load performance, on the other hand, depended largely on the control strategy. In particular, reducing the fuel flow rate (while maintaining a constant air flow rate) reduced the system's exergetic efficiency to less than 45% at low loads. Alternatively, maintaining a constant fuel-to-air ratio allowed for a higher efficiency but reduced the system's operating envelope.

Economic analyses generally fall into one of the following categories: thermoeconomic or techno-economic analyses. A thermoeconomic analysis integrates energy and exergy balances to calculate the product streams' costs (e.g., electricity and steam costs). Techno-economic analyses, on the other hand, incorporate only energetic performance data into life cycle cost calculations [49, 60]. Gandiglio, et al. [60], for instance, performed a thermoeconomic comparison between multi-MW hybrid (pressurized) and non-hybrid (atmospheric) power plants. The authors first defined each system's productive structure, thus specifying the resources (e.g., fuel) and products (e.g., electricity) associated with each system. The authors then

applied cost balances to each system component to calculate the levelized cost of electricity, or LCOE (defined as the ratio of the life cycle cost to net power output), as well as the thermoeconomic cost of electricity, or TCOE (defined as the ratio of the total exergetic cost to the net power output). The authors found that the hybrid and non-hybrid systems exhibited similar LCOEs, but in terms of TCOE, the hybrid system performed superior to the non-hybrid system (47.71 $/MWh vs. 64.19 $/MWh, respectively). Franzoni, et al. [88] performed a techno-economic analysis of a hybrid system with various $CO_2$ capture configurations. The authors found that $CO_2$ capture with steam condensation yielded a lower LCOE and capital cost than a system with amine-based capture. Santin, et al. [89] performed a techno-economic analysis of a hybrid system with different fuels. The authors found that methanol-fueled systems yielded higher internal rates of return on investment (IRRs) than kerosene-fueled systems. Cheddie and Murray [90] performed a techno-economic analysis of a multi-MW hybrid system, finding that the system yielded a minimum LCOE of 4.65 ¢/kWh.

In addition to hybrid systems, authors have considered advanced SOFC power plants to address environmental concerns surrounding central (baseload) power generation. Siefert, et al. [91] performed a techno-economic analysis of an integrated gasification fuel cell (IGFC) power plant with carbon capture and sequestration (CCS). The power plant yielded an IRR of approximately 4%. The authors compared the IGFC-CCS's economic performance to that of more conventional fossil fuel power plants, including natural gas combined cycle and pulverized coal combustion power plants. The authors found that advanced power plants (IGFC and integrated gasification combined cycle (IGCC) power plants with CCS) yielded lower LCOEs than more conventional power plants, assuming sufficiently high natural gas and $CO_2$ emission prices. Siefert, et al. [92] modeled an IGFC-CCS with a CaO-looping gasifier. The authors found that the power plant yielded an IRR of approximately 5%, depending on the SOFC's operating point. Siefert and Litster [93] and Trendewicz and Braun [94] both performed techno-economic analyses of biogas-fueled SOFC systems. These studies found the SOFC systems to be economically competitive with more conventional technologies, including microturbines and reciprocating engines. Becker, et al. [95] performed a techno-economic analysis of an SOFC polygeneration system, which produced thermal energy, $H_2$, and power, all from the same fuel source. The authors determined the cost of $H_2$ production (4.4 $/kg) to

be competitive with alternative $H_2$ production pathways, such as steam-methane reforming and electrolysis.

The present study perhaps draws most heavily on the work of Braun [56,96,97], who considered small (residential-scale) non-hybrid, SOFC systems. Braun [97] performed a techno-economic analysis of different SOFC system configurations, considering such features as anode gas recycle, cathode gas recycle, internal reforming, external reforming, $H_2$-fuel, and $CH_4$-fuel. He found that the $CH_4$-fueled system with anode gas recycle, cathode gas recycle, and 100% internal reforming yielded the greatest life cycle savings. Braun also found that even lower life cycle costs could be achieved by varying the fuel cell's voltage, fuel utilization, temperature, and air temperature rise. In his thesis and related work [56], Braun provides a thorough discussion of his modeling methodology and results. Hawkes and Leach [98–100] and Hawkes, et al. [101–104] also considered residential-scale CHP systems. Similar to many of the studies reviewed herein, the present work calculates the LCOEs of hybrid and non-hybrid systems. The present study also investigates the sensitivity of the LCOE to variations in operating parameters. The present study, however, does not implement a formal optimization method. More formal techniques may be found in the literature [98–107].

## 2.4 ENVIRONMENTAL ANALYSIS

Over the past few years, the U.S. Environmental Protection Agency (EPA) has proposed $CO_2$ emission standards for existing, modified/reconstructed, and new power pants. On September 20, 2013, the EPA proposed emission standards for new power plants, targeting utility boilers, IGCC power plants, and natural gas-fired stationary combustion turbines. The EPA proposed that utility boilers and IGCC plant be required to meet a standard of 1,000 $lb_m$ $CO_2$/MWh (0.45 kg $CO_2$/kWh) over a one year period, or 1,000–1,050 $lb_m$ $CO_2$/MWh (0.45–0.48 kg $CO_2$/kWh) over a seven year period. New combustion turbines with a heat input greater than 850 MMBtu/h (approximately 100 $MW_e$) would need to limit their emissions to 1,000 $lb_m$ $CO_2$/MWh (0.45 kg $CO_2$/kWh), while those with a heat input less than or equal to 850 MMBtu/h would need to limit their emissions to 1,100 $lb_m$ $CO_2$/MWh

(0.50 kg $CO_2$/kWh) [27]. On June 2, 2014, the EPA proposed emission standards for modified and reconstructed power plants. These standards established rate-based limits depending on the system type and time of modification [28]. On this same date, the EPA proposed the Clean Power Plan to establish state-specific, rate-based emission goals for existing power plants. The proposed guidelines would allow states to formulate their own plans toward meeting emission targets [29].

Previous life cycle assessment (LCA) studies indicate that $CO_2$ emissions from SOFC systems may be a concern, particularly during their use phase. LCA is a methodology for assessing a system's environmental impact over the course of its life cycle [108, 109]. Staffell, et al. [110] conducted a comparative LCA between a 1 kW residential SOFC-CHP system and a conventional system. The conventional system drew on electricity from the power grid and a condensing boiler to meet the thermal energy demand. The authors simulated both the SOFC and conventional systems in 1,000 residential buildings in the United Kingdom. The authors found that the SOFC system emitted significantly more $CO_2$ during its use stage than during its manufacturing and disposal stages. Osman and Ries [30] developed LCA models of various energy systems for commercial buildings, including an SOFC system, microturbine, and internal combustion engine. The authors found that the SOFC system produced higher global warming emissions across its life cycle compared to the other systems. These higher emissions resulted from the steam reforming of natural gas. Karakoussis, et al. [31] performed a life cycle inventory study on the manufacturing of planar and tubular SOFC systems. These authors compared key air emissions associated with the SOFC system manufacturing process with those during its use stage. The authors determined that the SOFC systems emitted significantly more $CO_2$ emissions during their use stage than during their manufacturing stage.

The present work calculates the $CO_2$ emissions during the operation of hybrid and non-hybrid systems. The hybrid system's emissions are compared to the EPA's proposed regulations for new power plants (described above). These regulations serve as a benchmark for future power generation. The hybrid system's emissions are also compared to those of more conventional CHP technologies. In particular, emissions data is taken from the EPA's Catalog of CHP Technologies [5] for reciprocating internal combustion engines, gas turbines,

and microturbines. These more mature technologies provide a benchmark for current power generation. Lastly, the hybrid system's emissions are compared to those of coal and natural gas sources in the U.S. The U.S. Energy Information Administration provides emissions data for coal and natural gas sources [111, 112]. Clearly, the environmental prospect of SOFC systems depends on a number of different factors. The present study addresses only a subset of these factors.

SOFC systems impact the environment during other life cycle stages as well. Osman and Ries [30] found that over 99% of the SOFC system's $NO_x$ emissions originated upstream of the use phase, during manufacturing and fuel production. The SOFC system emitted $1.41 \times 10^{-3}$ kg $NO_x$/kWh, compared to $2.34 \times 10^{-3}$ kg/kWh emitted by the microturbine. Pehnt [113] similarly found that the fuel cell system's acidification impact originated primarily from upstream manufacturing and fuel production processes. The electricity used to manufacture the stack, in particular, contributed significantly to the system's environmental impact. Exergetic life cycle assessment (ExLCA) is another technique for evaluating a system's environmental impact. ExLCA quantifies the mass, energy, and exergy flows associated with each life cycle stage. The system's (or process's) total exergy destruction equals the sum of its component exergy destructions, and the exergetic efficiency equals the total exergy output divided by the total exergy input [114]. Ozbilen, et al. [115] performed an ExLCA of an $H_2$ production process involving the thermochemical splitting of water. These authors applied exergy balance equations to the fuel processing, thermal energy production, and water-splitting stages. The fuel processing stage exhibited the highest exergy destruction (corresponding to the lowest exergetic efficiency), whereas the water-splitting stage exhibited the lowest exergy destruction (corresponding to the highest exergetic efficiency). Because the fuel processing stage exhibited the lowest exergetic efficiency, the authors recommended that this stage receive the most attention when improving system performance in future work. While the present study does not consider upstream life cycle stages, such as fuel processing or manufacturing, the integration of exergy with LCA is a possible direction for future work.

## 2.5 SUMMARY

The present work builds upon previous studies. Numerous studies, in particular, have investigated hybrid system control strategies. The present work complements these system-level studies by focusing specifically on the SOFC stack's behavior. Furthermore, numerous studies indicate that electrochemical dynamics inside fuel cells diminish within milliseconds following a load change. It seems reasonable, then, to neglect electrochemical processes inside an SOFC during dynamic operation. Few (if any) studies, however, have verified this assumption across a wide range of operating conditions, as done in the present study. Moreover, exergetic and economic studies demonstrate the potential of SOFC systems to operate efficiently and cost-effectively. The present study focuses specifically on comparing kW-scale hybrid and non-hybrid systems. Lastly, the EPA's proposed regulations provide a benchmark for future power generation, and emissions from more mature technologies provide a benchmark for current power generation. The next chapter develops the SOFC model. The SOFC model is incorporated into a larger system model in later chapters.

# 3.0 SOLID OXIDE FUEL CELL MODEL

The present work develops a solid oxide fuel cell (SOFC) model. The model is sufficiently simple to be incorporated into a larger system, while also capturing the fuel cell's main performance. The model calculates the fuel cell's operating voltage and power, as well as the current density, composition, and temperature profiles, among other quantities. The governing equations consist of the charge, species mass, energy, and momentum balances, and an equivalent circuit combines the fuel cell's irreversibilities with the charge double layer. The governing equations are applied separately to the gas channels, interconnect, and positive electrode-electrolyte-negative electrode (PEN) components along the flow path. Each of the channels is assumed to behave identically; hence, the fuel cell's performance is obtained by linearly scaling the performance of a single channel to the cell-level. The model allows for both steady-state and dynamic simulations.

## 3.1 REVERSIBLE VS. IRREVERSIBLE PERFORMANCE

SOFC performance is considered reversible (or ideal) when no irreversibilities are present. During reversible operation, the SOFC achieves its maximum possible operating voltage. In actual operation, however, the SOFC's performance is reduced by irreversible losses. These losses include slow reaction kinetics, finite mass flow rates through the electrodes, and ohmic resistance. Each of these losses depends on various fuel cell properties and operating parameters. The reversible and irreversible performance of a fuel cell are discussed in more detail in the sections to follow.

### 3.1.1 Reversible Performance

The first and second laws of thermodynamics provide an expression for the SOFC's reversible voltage. Steady-state operation is assumed, and changes in kinetic energy and potential energy are assumed negligible. These assumptions result in the following relationship between the electrical work and Gibbs free energy change of reaction:

$$W_{\mathrm{e}} \leq -\Delta\overline{g}_{\mathrm{eoh}}(T_{\mathrm{PEN}}) \tag{3.1}$$

where $W_{\mathrm{e}}$ is the electrical work generated by the SOFC, $\Delta\overline{g}_{\mathrm{eoh}}$ is the change in molar Gibbs free energy of the $H_2$ electrochemical oxidation reaction, and $T_{\mathrm{PEN}}$ is the temperature of the PEN structure [49]. The change in the molar Gibbs free energy represents the SOFC's maximum possible power generation. The SOFC generates its maximum electrical work when all processes occurring within the fuel are reversible, in which case the electrical work equals the change in molar Gibbs free energy.

The electrical work performed by the SOFC equals the amount of charge flowing through the circuit, $q$, multiplied by the reversible potential difference between the anode and cathode, $E_{\mathrm{N}}$:

$$W_{\mathrm{e}} = -qE_{\mathrm{N}} \tag{3.2}$$

The reversible potential, $E_{\mathrm{N}}$, is called the Nernst Potential. The amount of charge produced by the $H_2$ oxidation reaction is denoted by $n_{\mathrm{e}}F$, where $n_{\mathrm{e}}$ represents the number of moles of electrons transferred during the electrochemical reaction (2 moles), and $F$ is Faraday's constant. Combining Eqns. (3.1) and (3.2), the Nernst potential is expressed as follows:

$$E_{\mathrm{N}} = -\frac{\Delta\overline{g}_{\mathrm{eoh}}(T_{\mathrm{PEN}})}{n_{\mathrm{e}}F} \tag{3.3}$$

After further substitution and manipulation, it can be shown that the Nernst potential takes the following form:

$$E_{\mathrm{N}} = -\frac{\Delta\overline{g}^{\circ}_{\mathrm{eoh}}(T_{\mathrm{PEN}})}{2F} + \frac{\overline{R}T_{\mathrm{PEN}}}{2F}\ln\left(\frac{p_{\mathrm{H_2}}p_{\mathrm{O_2}}^{\frac{1}{2}}}{p_{\mathrm{H_2O}}p^{\circ\,\frac{1}{2}}}\right) \tag{3.4}$$

where $\overline{R}$ is the universal gas constant, $p_i$ is the partial pressure of species $i$, and $p^{\circ}$ is the standard pressure [26, 43].

### 3.1.2 Irreversible Performance

During actual operation, irreversible processes occur in a fuel cell. These irreversible processes are called polarizations. Polarizations cause the fuel cell's voltage to fall below its maximum possible value. Polarizations are classified as activation, ohmic, and concentration polarizations. These polarizations polarizations are discussed in more detail below.

**3.1.2.1 Activation Polarization** The activation polarization represents voltage loss due to slow reaction kinetics. The activation polarization is determined separately for each electrode, and the total activation polarization is the sum of the electrode polarizations [26]. From an electrochemical standpoint, the activation polarization is directly related to the electrochemical reactions occurring at the anode and cathode. Each of the electrode reactions constitutes a half-reaction. The electrode reactions, introduced in Chapter 1, are revisited below:

$$\text{Anode Reaction:} \quad \mathrm{H_2 + O^{2-} \longrightarrow H_2O + 2\,e^-} \qquad (1.2 \text{ revisited})$$

$$\text{Cathode Reaction:} \quad \tfrac{1}{2}\,\mathrm{O_2 + 2\,e^- \longrightarrow O^{2-}} \qquad (1.3 \text{ revisited})$$

The net reaction rate for each electrode is given by the difference between the forward and backward reaction rates. Accordingly, the net current density is given by the following expression:

$$j_{\text{net}} = j_{\text{forward}} - j_{\text{backward}} \tag{3.5}$$

where $j_{\text{net}}$ is the net current density, $j_{\text{forward}}$ is the current density associated with the forward reaction, and $j_{\text{backward}}$ is the current density associated with the backward reaction [43].

The net current density can be recast into the form:

$$j = j_0 \left( e^{\frac{\alpha \eta_{\text{act}} n_e F}{R T_{\text{PEN}}}} - e^{\frac{-(1-\alpha)\eta_{\text{act}} n_e F}{R T_{\text{PEN}}}} \right) \tag{3.6}$$

where $j$ henceforth denotes the net current density, $\eta_{\text{act}}$ is the activation polarization, and $T_{\text{PEN}}$ is the temperature of the PEN structure. The first term on the right-hand side Eqn. (3.6) represents the forward current contribution, and the second term represents the reverse current contribution. The parameter $\alpha$ is the transfer coefficient, which typically falls

between 0.2 and 0.5. Equation (3.6) is known as the Butler-Volmer equation. The Butler-Volmer equation relates an electrode's activation polarization to the net current density at a given electrode-electrolyte interface [43]. At equilibrium, $j = 0$, and $j_{\text{forward}} = j_{\text{backward}} = j_0$, where $j_0$ is the exchange current density. The exchange current density represents the magnitude of current traveling to and from the electrode at equilibrium [26]. To produce a net current ($j > 0$), the Galvani potentials at both electrodes are reduced by certain amounts. Galvani potentials are electrical potentials that develop at the anode-electrolyte and cathode-electrolyte interfaces during equilibrium. These reductions in Galvani potentials are where the term "activation polarization" is obtained. The activation polarizations need not be the same for the anode and cathode, but both electrodes must experience an activation polarization to produce net current. Reducing the Galvani potentials promotes the forward electrode reaction by decreasing the forward reaction's activation barrier while simultaneously increasing the backward reaction's activation barrier [43].

Substituting $\alpha = 0.5$ into Eqn. (3.6) results in the following equation for the activation polarization:

$$\eta_{\text{act}} = \frac{2\overline{R}T_{\text{PEN}}}{n_{\text{e}}F} \sinh^{-1}\left(\frac{j}{2j_0}\right) \tag{3.7}$$

The exchange current densities at the anode and cathode are given by the following equations:

$$j_{0,\text{an}} = \gamma_{\text{an}} \left(\frac{p^{\text{tpb}}_{\text{H}_2}}{p^\circ}\right) \left(\frac{p^{\text{tpb}}_{\text{H}_2\text{O}}}{p^\circ}\right) \exp\left(-\frac{E_{\text{act,an}}}{\overline{R}T_{\text{PEN}}}\right) \tag{3.8}$$

$$j_{0,\text{ca}} = \gamma_{\text{ca}} \left(\frac{p^{\text{tpb}}_{\text{O}_2}}{p^\circ}\right)^{0.25} \exp\left(-\frac{E_{\text{act,ca}}}{\overline{R}T_{\text{PEN}}}\right) \tag{3.9}$$

where $\gamma$ is a pre-exponential factor, $p_i^{\text{tpb}}$ is the partial pressure of species $i$ at the triple-phase boundary, and $E_{\text{act}}$ is the activation energy [43, 116–118]. The exchange current density formulas have been obtained from Costamagna and Honegger [116]. (In reference to the anode exchange current density formula, Costamagna and Honegger cite Refs. [119, 120]. In reference to the cathode exchange current density formula, Costamagna and Honegger cite Ref. [121].) In calculating the exchange densities, it is assumed that $\gamma_{\text{an}} = 5.5 \times 10^8$ A/m$^2$, $\gamma_{\text{ca}} = 7 \times 10^8$ A/m$^2$, $E_{\text{act,an}} = 100 \times 10^3$ J/mol, and $E_{\text{act,ca}} = 120 \times 10^3$ J/mol [117].

**3.1.2.2 Concentration Polarization** The concentration polarization represents voltage loss due to finite mass flow rates through the electrodes. During operation, the consumption of species due to the oxidation reaction reduces the concentration of reactants at the triple-phase boundary reaction sites. Fresh reactants diffuse through the electrodes to the triple-phase boundary to take their place, but they do so at a finite rate, resulting in concentration gradients across the electrodes. Similarly, production of $H_2O$ at the triple-phase boundary gives rise to an $H_2O$ concentration gradient across the anode [43, 44]. The concentration polarization is given by the difference between the Nernst potential evaluated using the bulk (channel) partial pressures and the triple-phase boundary partial pressures:

$$\eta_{\text{conc}} = \frac{\overline{R}T_{\text{PEN}}}{n_e F} \ln\left(\frac{p_{H_2}^{\text{ch}} p_{O_2}^{\text{ch}\,\frac{1}{2}}}{p_{H_2O}^{\text{ch}}} \frac{p_{H_2O}^{\text{tpb}}}{p_{H_2}^{\text{tpb}} p_{O_2}^{\text{tpb}\,\frac{1}{2}}}\right) \tag{3.10}$$

where $p_i^{\text{ch}}$ is the partial pressure of species $i$ in the anode or cathode channel [43, 118].

As evidenced by Eqn. (3.10), calculation of the concentration polarization requires determination of the triple-phase boundary partial pressures. Fick's law of diffusion provides expressions for the triple-phase boundary partial pressures. Fick's law is applied along the thickness of the electrodes as follows:

$$J_i^* = -C D_{i,\text{eff}} \frac{dy_i}{dz} \tag{3.11}$$

where $J_i^*$ is the diffusive flux of species $i$, $C$ is the molar concentration of the gas mixture, $D_{i,\text{eff}}$ is the effective diffusion coefficient through the electrode, and $y_i$ is the mole fraction of species $i$ [122]. The coordinate $z$ is assumed to run along the electrodes' thickness. The oxidation reaction rate is given by Faraday's law:

$$\dot{r}_{\text{eoh}} = \frac{i}{n_e F} \tag{3.12}$$

where $\dot{r}_{\text{eoh}}$ is the electrochemical oxidation of $H_2$ (eoh) reaction rate, and $i$ is the electric current [43]. Combining Eqns. (3.11) and (3.12), the diffusion of reactant $i$ through the electrode is expressed as follows:

$$\frac{p D_{i,\text{eff}}}{\overline{R}T_{\text{PEN}}} \frac{y_i^{\text{ch}} - y_i^{\text{tpb}}}{\tau_{\text{an(ca)}}} = \nu_i \frac{j}{n_e F} \tag{3.13}$$

where $p$ is the (total) pressure, $y_i^{\text{ch}}$ is the mole fraction of species $i$ in the anode or cathode channel, $y_i^{\text{tpb}}$ is the mole fraction of species $i$ at the triple-phase boundary, and $\tau_{\text{an(ca)}}$ is the thickness of the anode (or cathode) [43,44,118]. In Eqn. (3.13), $p/\overline{R}T_{\text{PEN}}$ has been substituted for the mixture concentration according to the ideal gas equation of state. Lastly, rearranging Eqn. (3.13), and letting $y_i = p_i/p$, results in the following relations between the channel and the triple-phase boundary partial pressures:

$$p_{\text{H}_2}^{\text{tpb}} = p_{\text{H}_2}^{\text{ch}} - \frac{j}{n_{\text{e}}F}\frac{RT_{\text{PEN}}\tau_{\text{an}}}{D_{\text{H}_2,\text{eff}}} \tag{3.14}$$

$$p_{\text{H}_2\text{O}}^{\text{tpb}} = p_{\text{H}_2\text{O}}^{\text{ch}} + \frac{j}{n_{\text{e}}F}\frac{\overline{R}T_{\text{PEN}}\tau_{\text{an}}}{D_{\text{H}_2\text{O},\text{eff}}} \tag{3.15}$$

$$p_{\text{O}_2}^{\text{tpb}} = p_{O_2}^{\text{ch}} - \frac{1}{2}\frac{j}{n_{\text{e}}F}\frac{RT_{\text{PEN}}\tau_{\text{ca}}}{D_{O_2,\text{eff}}} \tag{3.16}$$

Eqns. (3.14)–(3.16) provide the desired relations between the channel and triple-phase boundary partial pressures.

The effective diffusion coefficient takes into account the porous nature of the electrode and the tortuosity of the diffusion path as follows:

$$D_{i,\text{eff}} = \frac{\varepsilon}{\tau}D_i \tag{3.17}$$

where $\varepsilon$ is the porosity, and $\tau$ is the tortuosity [123]. Representative values for both electrodes are $\varepsilon = 0.30$, and $\tau = 6$ [73, 124]. In Eqn. (3.17), $D_i$ is the combined diffusion coefficient, which accounts for diffusion due to concentration gradients, as well as the interactions between species and the electrode wall. The combined diffusion coefficient is calculated as follows:

$$D_i = \left(\frac{1}{D_{ij}} + \frac{1}{D_{i,\text{Knudsen}}}\right)^{-1} \tag{3.18}$$

where $D_{ij}$ is the binary diffusion coefficient, and $D_{i,\text{Knudsen}}$ is the Knudsen diffusion coefficient [73, 118, 125]. The Chapman-Enskog formula for the binary diffusion coefficient of species $i$ and $j$ in an ideal gas mixture is given by the following formula:

$$D_{ij} = \frac{0.0018583}{p\sigma_{ij}^2\Omega_{\text{D},ij}}\sqrt{T_{\text{PEN}}^3\left(\frac{1}{M_i} + \frac{1}{M_j}\right)} \tag{3.19}$$

where $\sigma_{ij}$ is the collision diameter, $\Omega_{\mathrm{D},ij}$ is the diffusion collision integral, and $M_i$ is the molecular weight of species $i$ [126]. The Knudsen diffusion coefficient is given by the following formula:

$$D_{i,\mathrm{Knudsen}} = \frac{2}{3} r_{\mathrm{e}} \left( \frac{8\overline{R}T_{\mathrm{PEN}}}{\pi M_i} \right)^{\frac{1}{2}} \tag{3.20}$$

where $r_{\mathrm{e}}$ is the effective pore radius of the electrode material [125]. A representative value for the effective pore radius is $r_{\mathrm{e}} = 0.5\ \mu$m for both electrodes [73, 124].

**3.1.2.3 Ohmic Polarization** The ohmic polarization represents voltage loss caused by ohmic and contact resistances. The ohmic resistance of each component is calculated using electrical conductivity formulas provided in the literature [127 (citing [128])]. The estimate for the contact resistance is based on results provided by Koide, et al. [129]. These authors experimentally determined the total ohmic area-specific resistance (ASR) of an SOFC (with materials similar to those used in the present model) to be approximately 0.25 ohm $\cdot$ cm$^2$ (higher or lower depending on the volume percent of Ni in the anode). The authors further determined that the contact resistance between the anode and electrolyte dominated their ASR measurement. The estimate of 0.25 ohm $\cdot$ cm$^2$ for the contact resistance is used in the present study, and this value is assumed to remain constant, regardless of the stack's operating point [116]. Since the SOFC components occur in series, the total ohmic resistance is calculated by simply summing the resistances of the individual components. Accordingly, the ohmic polarization is calculated as follows:

$$\eta_{\mathrm{ohm}} = i(R_{\mathrm{anode}} + R_{\mathrm{cathode}} + R_{\mathrm{electrolyte}} + R_{\mathrm{interconnect}} + R_{\mathrm{contact}}) \tag{3.21}$$

where $R_i$ is the resistance of component $i$.

**3.1.2.4 Charge Double Layer** In the present study, an equivalent circuit combines the fuel cell's irreversibilities with the charge double layer. The charge double layer is a (dual) layer of charge that accumulates along the anode-electrolyte and cathode-electrolyte interfaces during operation. Figure 3.1a presents one such charge configuration. Charge may accumulate due to electrochemical reactions or diffusion of charge across the interfaces, or possibly another cause [26, 43]. Values for the charge double layer capacitance vary widely

in the literature, ranging from hundreds of microFarads to a few Farads [26, 64, 130]. The charge double layers are represented as capacitors in the equivalent circuit, as shown in Fig. 3.1b. The parameters $C_{\text{dbl,an}}$ and $C_{\text{dbl,ca}}$ are the charge double layer capacitances of the anode and cathode, respectively. Additionally, the equivalent circuit presented in Fig. 3.1b also accounts for each of the polarizations previously discussed. In this circuit, each of the polarizations is represented by an equivalent resistance. The parameters $R_{\text{act,an}}$ and $R_{\text{conc,an}}$ denote the activation and concentration equivalent resistances of the anode, respectively, and similar for the cathode. Equivalent resistance is defined as the ratio of each polarization to the current [68]:

$$\text{Activation:} \quad R_{\text{act}} = \frac{\eta_{\text{act}}}{i} \tag{3.22}$$

$$\text{Concentration:} \quad R_{\text{conc}} = \frac{\eta_{\text{conc}}}{i} \tag{3.23}$$

$$\text{Ohmic:} \quad R_{\text{ohm}} = \frac{\eta_{\text{ohm}}}{i} \tag{3.24}$$

In the equivalent circuit, the Nernst potential is represented as a voltage source. Recall from Section 3.1.1 that the Nernst potential represents the reversible potential of the SOFC. The operating voltage of the SOFC is denoted by $V_{\text{op}}$.

In practice, a simplified equivalent circuit is used to obtain the charge balance equation. The simplified circuit is shown in Fig. 3.2. In this circuit, the parameters $R_{\text{act}}$ and $R_{\text{conc}}$ represent the total activation and concentration equivalent resistances, respectively, which are the sums of the individual electrode equivalent resistances. The operating voltage is determined by applying Kirchoff's Voltage Law. That is, Kirchoff's Voltage Law is applied to the entire circuit shown in Fig. 3.2 to obtain the following expression for $V_{\text{op}}$:

$$V_{\text{op}} = E_{\text{N}} - V_{\text{dbl}} - iR_{\text{ohm}} \tag{3.25}$$

where $V_{\text{dbl}}$ is the total voltage drop across the charge double layers. The equation above is the charge balance equation, and it accounts for the charging and discharging of the charge double layer. Applying Kirchoff's Voltage Law again, but this time to the smaller loop in

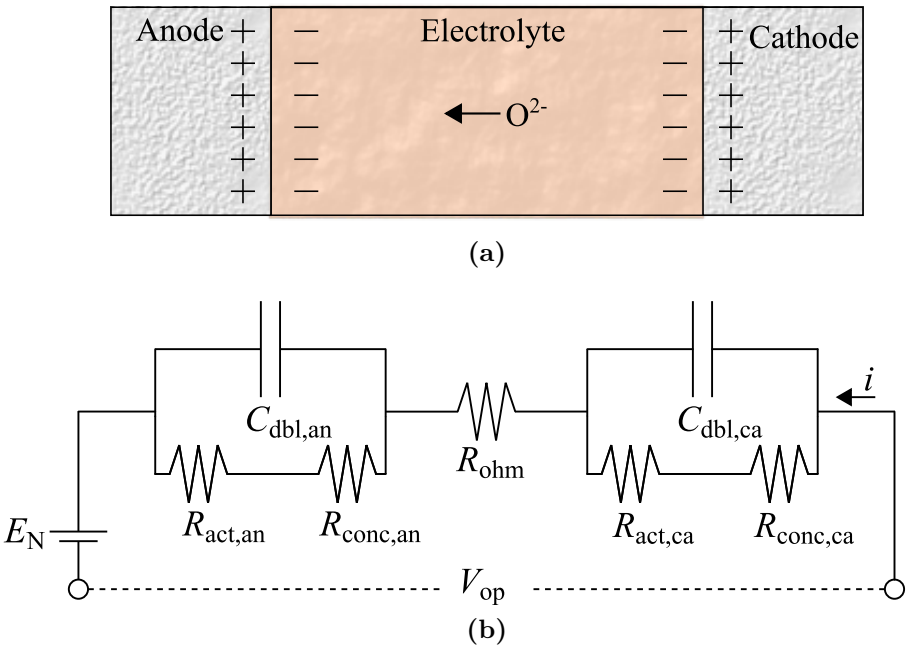


**Figure 3.1** Representation of irreversible processes inside the SOFC: (a) Possible charge double layer in SOFC (adapted from Ref. [43]) (b) Equivalent circuit (adapted from Refs. [43, 65, 66]).

Fig. 3.2 (consisting of the activation and concentration equivalent resistances, and the double layer capacitance), results in the following expression for the time rate of change of $V_{\text{dbl}}$:

$$\frac{dV_{\text{dbl}}}{dt} = \frac{1}{C_{\text{dbl}}}\left(i - \frac{V_{\text{dbl}}}{R_{\text{act}} + R_{\text{conc}}}\right) \tag{3.26}$$

During each time step, Eqn. (3.26) is used to update the value of $V_{\text{dbl}}$ [64].

## 3.2 GOVERNING EQUATIONS

In addition to the charge balance equation, the SOFC model consists of the species mass, energy, and momentum balance equations. Unlike the charge balance, these balance equations are 1-D, partial differential equations. Each of the balance equations is expressed dynamically, and the system of equations is solved using implicit, finite-difference approximations.

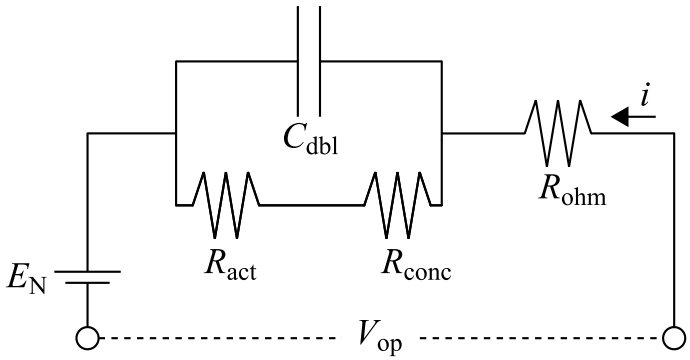


**Figure 3.2** Simplified equivalent circuit used to calculate SOFC operating voltage (adapted from Refs. [26, 64, 68, 69]).

Each of these balance equations is discussed in more detail below, and the charge balance is repeated for completeness.

### 3.2.1 Charge Balance

The charge balance relates the fuel cell's voltage and current density to the irreversibilities present within the SOFC. The equivalent circuit model presented in Section 3.1.2 provides such a relationship. This relationship is restated below. The SOFC's operational voltage is reduced below its reversible value due to activation, concentration, and ohmic polarizations. Internal current and fuel crossover are neglected.

$$V_{\text{op}} = E_{\text{N}} - V_{\text{dbl}} - iR_{\text{ohm}} \qquad \text{(3.25 revisited)}$$

$$E_{\text{N}} = -\frac{\Delta\overline{g}^{\circ}(T_{\text{PEN}})}{2F} + \frac{\overline{R}T_{\text{PEN}}}{2F}\ln\left(\frac{p_{\text{H}_2}p_{\text{O}_2}^{\frac{1}{2}}}{p_{\text{H}_2\text{O}}p^{\circ\,\frac{1}{2}}}\right) \qquad \text{(3.4 revisited)}$$

$$R_{\text{act}} = \frac{\eta_{\text{act}}}{i} \qquad \text{(3.22 revisited)}$$

$$R_{\text{conc}} = \frac{\eta_{\text{conc}}}{i} \qquad \text{(3.23 revisited)}$$

$$R_{\text{ohm}} = \frac{\eta_{\text{ohm}}}{i} \qquad \text{(3.24 revisited)}$$

The operating voltage is assumed constant along the SOFC's length. The temperature and partial pressures, on the other hand, vary along the SOFC's length, giving rise to spatially-varying Nernst potential and current density distributions. The power in each computational segment is calculated according to $\dot{W}_{\text{seg}} = i_{\text{seg}} V_{\text{op}}$, where $\dot{W}_{\text{seg}}$ is the power calculated in a given computational segment, and $i_{\text{seg}}$ is the electric current in that segment.

### 3.2.2 Species Mass Balance

Species in the anode and cathode channels undergo changes in molar flow rate as they participate in the oxidation, steam methane reforming, and water-gas shift reactions. The 1-D species mass balance applied to the anode and cathode channels is presented below on a molar basis:

$$\frac{\partial n_i'''}{\partial t} = -\frac{\partial \dot{n}_i''}{\partial x} - \frac{\partial J_i^{*\prime\prime}}{\partial x} + \sum_j \nu_{i,j} \dot{r}_j''' \tag{3.27}$$

where $n_i'''$ represents the moles of species $i$ per unit volume, $\dot{n}_i''$ is the molar flux of species $i$ due to advection, $J_i^{*\prime\prime}$ is the diffusive flux of species $i$, $\nu_{i,j}$ is the stoichiometric coefficient of species $i$ associated with reaction $j$, and $\dot{r}_j'''$ is the rate of reaction $j$ per unit volume [43, 96, 118, 122]. The species mass balance is expressed in implicit, finite-difference form as follows [96, 122, 131]:

$$\frac{n_{i,m+1}^{\prime\prime\prime p+1} - n_{i,m+1}^{\prime\prime\prime p}}{\Delta t} = -\frac{\dot{n}_{i,m+1}^{\prime\prime p+1} - \dot{n}_{i,m}^{\prime\prime p+1}}{\Delta x} - \frac{J_{i,m+1}^{*\prime\prime p+1} - J_{i,m}^{*\prime\prime p+1}}{\Delta x} + \sum_j \nu_{i,j} \dot{r}_j''' \tag{3.28}$$

where $p$ denotes the time step number, $m$ denotes the node number, $\Delta t$ denotes the time step size, and $\Delta x$ denotes the spatial step size.

The water-gas shift reaction is assumed to be in equilibrium. The equilibrium constant for the water-gas shift reaction is given by the following equation:

$$\ln\left(K_{\text{wgs}}\right) = -\frac{\Delta \overline{g}^{\circ}_{\text{wgs}}(T_{\text{PEN}})}{\overline{R} T_{\text{PEN}}} \tag{3.29}$$

where $\Delta \overline{g}^{\circ}(T_{\text{PEN}})$ is the change in the molar Gibbs free energy of the water-gas shift reaction evaluated at standard pressure and the PEN temperature. The equilibrium constant also

equals the ratio of the product species molar flow rates to the reactant species molar flow rates [49]:

$$K_{\text{wgs}} = \frac{\dot{n}_{\text{H}_2}\dot{n}_{\text{CO}_2}}{\dot{n}_{\text{H}_2\text{O}}\dot{n}_{\text{CO}}} \tag{3.30}$$

The changes in the species molar flow rates due to the water-gas shift reaction are related as follows by stoichiometry [49, 96]:

$$\Delta\dot{n}_{\text{CO,wgs}} = \Delta\dot{n}_{\text{H}_2\text{O,wgs}} \tag{3.31}$$

$$\Delta\dot{n}_{\text{H}_2\text{O,wgs}} = -\Delta\dot{n}_{\text{H}_2\text{,wgs}} \tag{3.32}$$

$$-\Delta\dot{n}_{\text{H}_2\text{,wgs}} = -\Delta\dot{n}_{\text{CO}_2\text{,wgs}} \tag{3.33}$$

In addition, the methane steam reforming reaction rate is given by the following formula:

$$\dot{r}_{\text{msr}} = k_{\text{o}} f_{\text{e}} p_{\text{CH}_4} A_{\text{r}} e^{-\frac{E_{\text{act}}}{\overline{R}T_{\text{PEN}}}} \tag{3.34}$$

where the pre-exponential factor $k_{\text{o}} = 4274$ mol/s·m$^2$·bar, the equilibrium function $f_{\text{e}} \approx 1$, $A_{\text{r}}$ is the electrode reaction surface area, and the activation energy $E_{\text{act}} = 8.2 \times 10^4$ J/mol [132]. The partial pressure of methane, $p_{\text{CH}_4}$, should technically be based on the concentration of methane at the electrode surface, but it has been shown that the partial pressure based on the bulk concentration in the channel provides a reasonable approximation [96]. The electrochemical oxidation reaction is given by Eqn. (3.12) and is restated below:

$$\dot{r}_{\text{eoh}} = \frac{i}{n_{\text{e}}F} \tag{3.12 revisited}$$

The electrochemical oxidation of CO is not considered in the present study.

Diffusive flux is given by Fick's law of diffusion:

$$J_i^* = -CD_{i,\text{mixture}}\frac{dy_i}{dx} \tag{3.35}$$

where $J_i^*$ is the diffusive flux of species $i$, $C$ is the molar concentration of the gas mixture, and $D_{i,\text{mixture}}$ is the mixture diffusion coefficient of species $i$ [122]. The mixture diffusion coefficient is calculated using the following formula for multicomponent mixtures:

$$D_{i,\text{mixture}} = (1 - y_i)\left(\sum_{\substack{j=1 \\ j\neq i}}^{n} \frac{y_j}{D_{ij}}\right)^{-1} \tag{3.36}$$

where $D_{i,\text{mixture}}$ is the mixture diffusion coefficient, $D_{ij}$ is the binary molecular diffusion coefficient for species $i$ and $j$ (calculated using the Chapman-Enskog formula), and $y_j$ is the mole fraction of species $j$ [133].

Lastly, the fuel utilization and air ratio specify the amount of fuel oxidized and the amount of air supplied to the SOFC, respectively. Different definitions of the fuel utilization are used in this study depending on the type of simulation being performed. The definition is specified as appropriate. The first definition accounts for the amount of fuel oxidized relative to the amount of fuel admitted into the SOFC:

$$U_{\text{f},1} = \frac{\dot{n}_{\text{H}_{2,\text{consumed}}}}{4\dot{n}_{\text{CH}_4,\text{inlet}} + \dot{n}_{\text{H}_2,\text{inlet}} + \dot{n}_{\text{CO,inlet}}} \tag{3.37}$$

where $U_\text{f}$ is fuel utilization, $\dot{n}_{\text{H}_2,\text{consumed}}$ is the amount of $\text{H}_2$ consumed by the SOFC, and $\dot{n}_{i,\text{inlet}}$ is the inlet molar flow rate of species $i$ [96, 127]. The second definition accounts for the difference between the inlet and exit flow rates relative to the inlet flow rate [57, 96]:

$$U_{\text{f},2} = 1 - \frac{4\dot{n}_{\text{CH}_4,\text{exit}} + \dot{n}_{\text{H}_2,\text{exit}} + \dot{n}_{\text{CO,exit}}}{4\dot{n}_{\text{CH}_4,\text{inlet}} + \dot{n}_{\text{H}_2,\text{inlet}} + \dot{n}_{\text{CO,inlet}}} \tag{3.38}$$

This latter definition accounts for fuel storage inside the SOFC, thus capturing mass flow dynamic behavior [57]. The air ratio is given by the following equation:

$$\lambda_{\text{air}} = \frac{\dot{n}_{\text{O}_2,\text{inlet}}}{2\dot{n}_{\text{CH}_4,\text{inlet}} + \frac{1}{2}(\dot{n}_{\text{H}_2,\text{inlet}} + \dot{n}_{\text{CO,inlet}})} \tag{3.39}$$

This equation defines the excess air ratio in terms of the number of moles of $\text{O}_2$ supplied to the SOFC divided by the number of moles of $\text{O}_2$ required for stoichiometry (assuming that the methane steam reforming and water-gas shift reactions are brought to completion) [96, 127].

### 3.2.3 Energy Balance

**3.2.3.1 Gas Channels** The energy balance applied to the gas channel includes contributions from advection and convection. The 1-D energy balance applied to the anode and cathode channels is expressed as follows:

$$\rho_{\mathrm{f(a)}} c_{\mathrm{p,f(a)}} \frac{\partial T_{\mathrm{f}}}{\partial t} = -\sum_{i} \frac{\partial \left( \overline{h}_i \left( \dot{n}_i'' + \dot{J}_i^{*''} \right) \right)}{\partial x} + \sum_{\text{reactions}} \overline{h}_i \nu_{i,j} \dot{r}_j''' + q_{\text{conv}}''' \tag{3.40}$$

where $\rho_{\mathrm{f(a)}}$ is the fuel (or air) density, $c_{\mathrm{p,f(a)}}$ is the fuel's (or air's) specific heat capacity at constant pressure, $T_{\mathrm{f(a)}}$ is the fuel's (or air's) temperature, and $\overline{h}_i$ is the molar specific enthalpy of species $i$ [43, 70, 73, 96, 118, 122, 134].

Convection occurs between the gases and solid components (i.e., the interconnect and PEN structure). Convection is modeled using Newton's law of cooling:

$$q_{conv} = h A_{\mathrm{s}} (T_{\mathrm{s}} - T_{\mathrm{f(a)}}) \tag{3.41}$$

where $T_{\mathrm{s}}$ is the surface temperature of the solid component, $T_{\mathrm{f(a)}}$ is the temperature of the fuel (or air), $A_{\mathrm{s}}$ is the heat transfer surface area, and $h$ is the convection coefficient between the solid and gas [122]. The following correlation by Shah and London provides the convection coefficient for a rectangular channel assuming laminar, fully-developed (thermally and hydrodynamically) flow and uniform temperature peripherally and axially:

$$Nu = 7.541 \left( 1 - 2.610\alpha^* + 4.970\alpha^{*2} - 5.119\alpha^{*3} + 2.702\alpha^{*4} - 0.548\alpha^{*5} \right) \tag{3.42}$$

where $\alpha^*$ is the aspect ratio of channel height to channel width [135].

The dimensionless Nusselt number is related to the convection coefficient as follows:

$$Nu = \frac{h D_{\mathrm{h}}}{k_{\mathrm{f(a)}}} \tag{3.43}$$

where $Nu$ is the Nusselt number, $k_{\mathrm{f(a)}}$ is the thermal conductivity of the fuel (air), and $D_{\mathrm{h}}$ is the hydraulic diameter of the gas channel [122]. The bulk thermal conductivity is calculated using Wassiljewa's formula for the thermal conductivity of a gas mixture at low pressure:

$$k = \sum_{i=1}^{n} \frac{y_i k_i}{\sum_{j=1}^{n} y_j A_{ij}} \tag{3.44}$$

where $n$ is the number of species, $k_i$ is the thermal conductivity of species $i$, $y_i$ is the mole fraction of species $i$, and $A_{ij}$ is calculated using Mason and Saxena's modification:

$$A_{ij} = \frac{\varepsilon[1 + (k_i/k_j)^{1/2}(M_i/M_j)^{1/4}]^2}{[8(1 + M_i/M_j)]^{1/2}} \tag{3.45}$$

where $\varepsilon \approx 1$, and $M_i$ is the molecular weight of species $i$ [136].

**3.2.3.2 PEN Structure** The anode, electrolyte, and cathode are modeled as a lumped solid. This assumption is common among SOFC models [56,73,74,118]. The energy balance applied to the PEN structure includes contributions from conduction, convection, radiation, and power generated by the SOFC [43,96,118]:

$$\rho_{\text{PEN}} c_{\text{p,PEN}} \frac{\partial T_{\text{PEN}}}{\partial t} = \sum_{\text{reactions}} \overline{h}_i \nu_{i,j} \dot{r}_j''' - \frac{\partial q_{\text{cond}}''}{\partial x} + q_{\text{conv}}''' + q_{\text{rad}}''' - P_{\text{seg}}''' \tag{3.46}$$

Heat transfer due to conduction is calculated using Fourier's Law:

$$q_{\text{cond}}'' = -k_{\text{PEN}} \frac{\partial T}{\partial x} \tag{3.47}$$

where $k_{\text{PEN}}$ is the thermal conductivity of the PEN structure [122]. Heat transfer due to radiation is calculated according to the formula for a two-surface enclosure, assuming that both surfaces are opaque, diffuse, gray, and isothermal with uniform radiosity and irradiation:

$$q_{\text{rad}} = \frac{\sigma(T_1^4 - T_2^4)}{\frac{1-\varepsilon_1}{\varepsilon_1 A_1} + \frac{1}{A_1 F_{12}} + \frac{1-\varepsilon_2}{\varepsilon_2 A_2}} \tag{3.48}$$

where $\sigma$ is the Stefan-Boltzmann constant, $\varepsilon_i$ is emissivity of surface $i$, and $A_i$ is the heat transfer surface area associated with surface $i$. The above formula assumes that the fuel and air are non-participating (transmissivity of the gas is approximately 1), which is a reasonable assumption considering the short separation distance between the top and bottom surfaces [122]. The boundaries of the PEN structure are assumed to be adiabatic.

**3.2.3.3 Interconnect** The energy balance applied to the fuel and air-side interconnects includes contributions from conduction, convection, and radiation. This energy balance can be expressed most simply as follows [43, 96, 118]:

$$\rho_{\text{inter}_{\text{f(a)}}} c_{\text{p,inter}_{\text{f(a)}}} \frac{\partial T_{\text{inter}_{\text{f(a)}}}}{\partial t} = \frac{\partial q''_{\text{cond}}}{\partial x} + q'''_{\text{conv}} + q'''_{\text{rad}} \tag{3.49}$$

Heat transfer due to conduction, convection, and radiation are calculated as before using Eqns (3.47), (3.41), and (3.48), respectively.

### 3.2.4 Momentum Balance

The momentum balance applied to the gas channels has the following form:

$$\frac{\partial \left(\rho_{\text{f(a)}} u_{\text{f(a)}}\right)}{\partial t} = -\frac{\partial \left(\rho_{\text{f(a)}} u_{\text{f(a)}} u_{\text{f(a)}}\right)}{\partial x} - \frac{\partial p_{\text{f(a)}}}{\partial x} - \frac{\hat{p}_{\text{f(a)}}}{A_{\text{c,f(a)}}} \tau_{\text{w}}$$

where $u_{\text{f(a)}}$ is axial velocity in the anode (or cathode) channel, $\hat{p}_{\text{f(a)}}$ is the perimeter of the anode (or cathode) channel, $A_{\text{c,f(a)}}$ is the cross-sectional area of the anode (or cathode) channel, and $\tau_{\text{w}}$ is the wall shear stress [79, 137, 138]. The Fanning friction factor for fully-developed (hydrodyamically and thermally), laminar flow in a rectangular channel is given by:

$$C_{\text{f}} Re = 24 \left(1 - 1.3553\alpha^* + 1.9467\alpha^{*^2} - 1.7012\alpha^{*^3} + 0.9564\alpha^{*^4} - 0.2537\alpha^{*^5}\right)$$

where $C_f$ is the fanning friction factor, and $Re$ is the Reynolds number [135]. The wall shear stress is related to the Fanning friction factor as follows:

$$C_{\text{f}} = \frac{\tau_{\text{w}}}{\rho u^2/2}$$

and the Reynolds number is defined as:

$$Re = \frac{\rho u D_{\text{h}}}{\mu_{\text{mixture}}} \tag{3.50}$$

where $\mu$ is the mixture viscosity in the gas channel [122]. The mixture viscosity is calculated using Wilke's formula for the viscosity of a gas mixture at low pressure:

$$\mu_{\text{mixture}} = \sum_{i=1}^{n} \frac{y_i \mu_i}{\sum_{j=1}^{n} y_j \phi_{ij}} \tag{3.51}$$

where

$$\phi_{ij} = \frac{[1 + (\mu_i/\mu_j)^{1/2}(M_j/M_i)^{1/4}]^2}{[8(1 + M_i/M_j)]^{1/2}} \tag{3.52}$$

and $\mu_i$ is the viscosity of species $i$ [136].

The SOFC model also accounts for minor losses at the inlet and exit of the gas channels [96, 139]. These additional pressure losses are presented below:

$$\Delta P_{\text{inlet}} = \frac{\rho u^2}{2} K_{\text{inlet}} \tag{3.53}$$

$$\Delta P_{\text{exit}} = \frac{\rho u^2}{2} K_{\text{exit}} \tag{3.54}$$

where $\Delta P_{\text{inlet}}$ is the inlet pressure drop, and $\Delta P_{\text{exit}}$ is the exit pressure drop [138]. Flow through the SOFC's feed and exhaust headers is characterized by sharp, right-angle turns [26, 140], and these turns induce pressure losses at the inlet and exit of the gas channels due to flow separation and swirling. The effect of these phenomena on the pressure drop is captured by the inlet and exit loss coefficients, $K_{\text{inlet}}$ and $K_{\text{exit}}$. Flow into and out of fuel cell headers is analogous to "branch flow" in pipes. Thus, representative values of the loss coefficients are $K_{\text{inlet}} = K_{\text{exit}} = 2.0$ [138].

## 3.3 SOLUTION TECHNIQUE

To solve the model's governing equations, a single SOFC channel is discretized into computational segments along the axial ($x$) direction (Fig. 3.3a). Each computational segment consists of several control volumes, corresponding to the anode channel, cathode channel, PEN structure, and interconnect components (Fig. 3.3b). Each control volume is assigned a node, representing the value of each quantity. The balance equations are applied to each

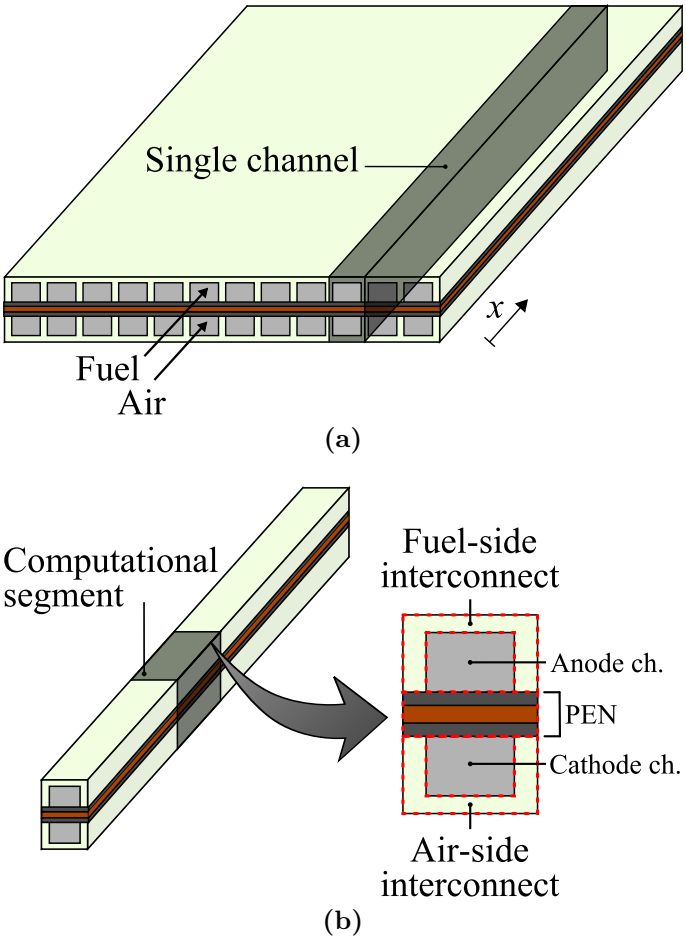


**Figure 3.3** SOFC discretization: (a) SOFC with channel highlighted, (b) Channel with computational segment highlighted (control volumes are indicated by red, dashed lines).

computational segment in finite-difference form. The energy balance applies to the gas channels, PEN structure, and interconnect, accounting for conduction, convection, and radiation. The species mass balance applies to the air and fuel channels, accounting for the production and consumption of each species. The momentum balance applies to the fuel and air channels. The resulting algebraic system is entered into the iterative equation solver software, Engineering Equation Solver (EES) [141]. Thermodynamic properties are obtained from EES. During dynamic simulations, parametric tables are used in EES to step through time, and lookup tables are used to store previous iterations.

## 3.4 SUMMARY

This chapter developed the SOFC model. The charge balance equation accounts for losses due to slow reaction kinetics, ohmic resistance, and finite mass flow rates through the electrodes. The equivalent circuit model combines the ohmic, activation, and concentration polarizations with the charge double layer, expressing the operating voltage in terms of the double layer capacitance, time, and additional quantities. The species mass and energy balances account for chemical and thermal changes axially, as well as thermal interactions and diffusion occurring perpendicular to the flow path. The momentum balance calculates the pressure drops in the fuel and air channels. The SOFC is divided into its individual components, and the gas channels are discretized into computational segments. The solution is obtained using the finite-different method, and the resulting linear system is solved in EES. The next chapter verifies the SOFC model during steady-state and dynamic operation.

# 4.0 FUEL CELL MODEL VERIFICATION

The solid oxide fuel cell (SOFC) model developed in in the previous chapter depends on many assumptions. While the model developed herein has intentionally been made sufficiently simple to be incorporated into a larger system, the model needs to also accurately capture the fuel cell's main performance. In this chapter, the fuel cell model is verified against results from reference studies in the literature. The International Energy Agency's (IEA's) Program of Research, Development, and Demonstration on Advanced Fuel Cells [142] serves as a benchmark study for the fuel cell's steady-state operation. Wang and Nehrir's study [68] on tubular SOFC dynamic response serves as a benchmark study for the fuel cell's dynamic behavior. While slight differences exist between the present study and reference studies, the overall agreement is acceptable.

## 4.1 GEOMETRIC AND MATERIAL PROPERTIES

The SOFC's geometric and material properties are presented in Tables 4.1 and 4.2, respectively. The geometric and materials properties are identical to those adopted in the IEA benchmark study [142, 127 (citing [128])]. The geometric properties (Table 4.1) define a square, electrolyte-supported, planar SOFC. Each of the gas channels is dimensioned identically, and the entire fuel cell area is assumed to be electroactive. Figure 4.1 presents the SOFC's dimensions pictorially. In Table 4.2, it should be mentioned that the thermal conductivity, heat capacity, and density pertain to the ceramic components, which comprises the interconnect and positive electrode-electrolyte-negative electrode (PEN) structure. The fuel cell's high operating temperature necessitates the use of ceramic interconnects. The

**Table 4.1** Geometric properties of the SOFC, according to the IEA benchmark study [142].

| Property | Value |
|---|---|
| Electroactive area, $L_{\text{cell}} \times W_{\text{cell}}$ | 100 mm × 100 mm |
| Anode thickness, $\tau_{\text{an}}$ | 0.05 mm |
| Cathode thickness, $\tau_{\text{ca}}$ | 0.05 mm |
| Electrolyte thickness, $\tau_{\text{electro}}$ | 0.15 mm |
| Interconnect thickness, $\tau_{\text{inter}}$ | 2.5 mm |
| Channel width, $W_{\text{ch}}$ | 3 mm |
| Channel height, $\tau_{\text{ch}}$ | 1 mm |
| Number of channels, $N_{\text{ch}}$ | 18 |
| Rib width, $W_{\text{rib}}$ | 2.42 mm |

**Table 4.2** Material properties of the SOFC, according to the IEA benchmark study [127 (citing [128])].

| Property | Value |
|---|---|
| Solid thermal conductivity | $2\ \text{W/m} \cdot \text{K}$ |
| Solid heat capacity | $400\ \text{J/kg} \cdot \text{K}$ |
| Solid density | $6600\ \text{kg/m}^3$ |
| Anode electronic conductivity | $\sigma_{\text{an}} = \frac{95\times10^6\ \text{K}\cdot\text{S}\cdot\text{m}^{-1}}{T_{\text{PEN}}} \exp\left(-\frac{1150\ \text{K}}{T_{\text{PEN}}}\right)$ |
| Cathode electronic conductivity | $\sigma_{\text{ca}} = \frac{42\times10^6\ \text{K}\cdot\text{S}\cdot\text{m}^{-1}}{T_{\text{PEN}}} \exp\left(-\frac{1200\ \text{K}}{T_{\text{PEN}}}\right)$ |
| Electrolyte ionic conductivity | $\sigma_{\text{electro}} = 3.34 \times 10^4\ \text{S} \cdot \text{m}^{-1} \exp\left(-\frac{10300\ \text{K}}{T_{\text{PEN}}}\right)$ |
| Interconnect electronic conductivity | $\sigma_{\text{inter}} = \frac{9.3\times10^6\ \text{K}\cdot\text{S}\cdot\text{m}^{-1}}{T_{\text{inter}}} \exp\left(-\frac{1100\ \text{K}}{T_{\text{inter}}}\right)$ |

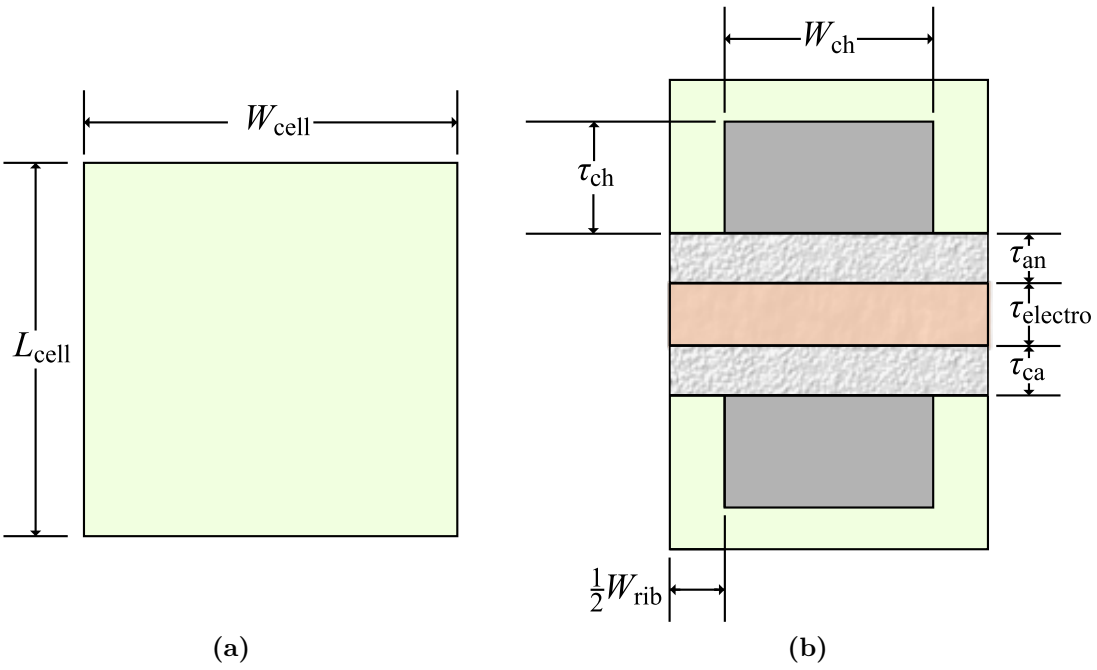


**Figure 4.1** SOFC dimensions: (a) Top view, (b) Front view.

material properties selected herein correspond to nickel zirconia cermet ($Ni_{0.35}\,(ZrO_2)_{0.65}$) as the anode material, strontium-doped lanthanum manganite ($La_{0.84}Sr_{0.16}MnO_3$) as the cathode material, yttria-stabilized zirconia ($(ZrO_2)_{0.90}\,(Y_2O_3)_{0.10}$) as the electrolyte material, and strontium-doped lanthanum chromite ($La_{0.84}Sr_{0.16}CrO_3$) as the interconnect material.

## 4.2 MESH INDEPENDENCE

The computational mesh is refined to the extent required for the results to become mesh-independent. Braun [96] demonstrated mesh-independence of a similar SOFC model by plotting distributions of the PEN temperature, current density, composition, and PEN temperature gradient vs. the number of nodes. The same approach is adopted here. While other quantities could be plotted to demonstrate mesh-independence, such as the Nernst potential

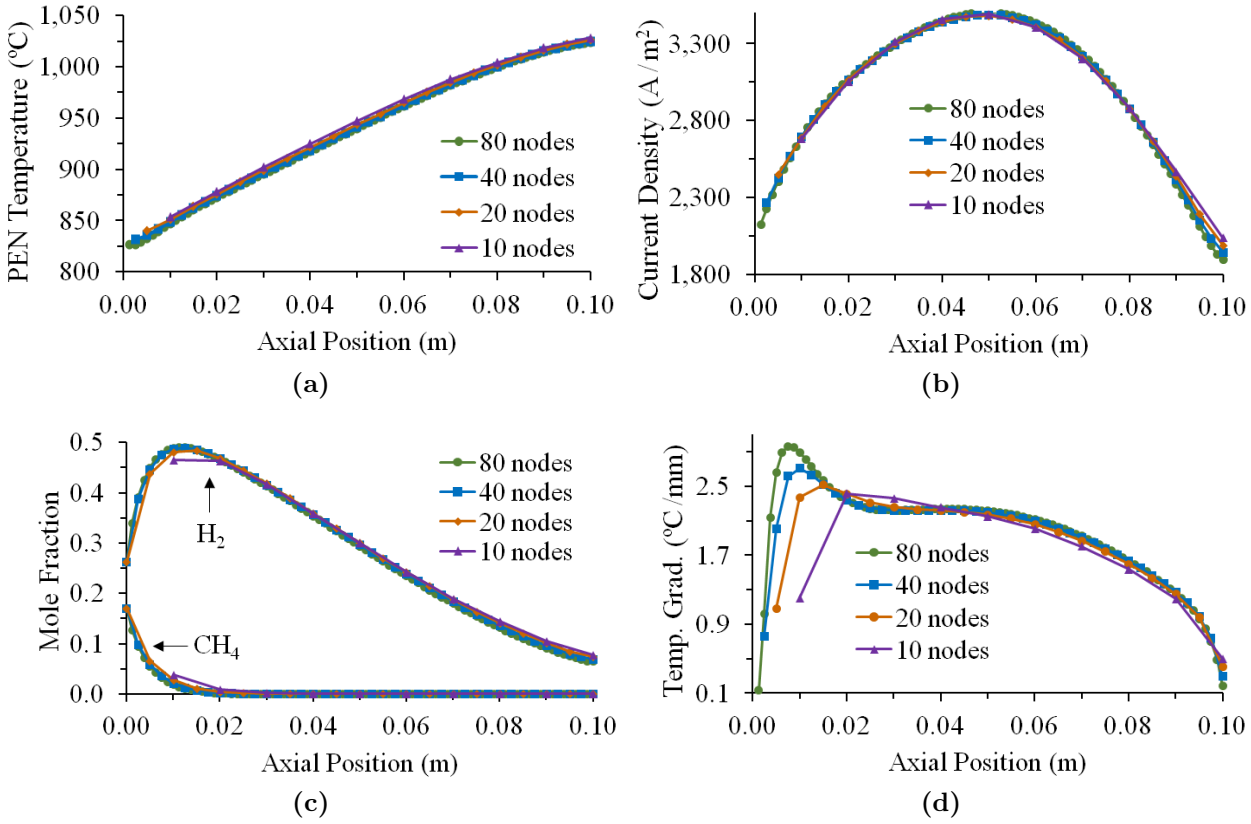


**Figure 4.2** Mesh-independence results: (a) PEN temperature distribution, (b) current density distribution, (c) fuel composition distribution, (d) PEN temperature gradient distribution.

or voltage, the chosen quantities are thought to represent the fuel cell's performance well. The Nernst potential and voltage, after all, depend on the temperature, current density, and composition profiles, as do other quantities. During mesh-independence testing, the number of nodes varies between 10 and 80 nodes. The operating conditions in the present study correspond to those adopted in the IEA benchmark study, which are presented in Table 4.3. Hence, the inlet gas composition, temperatures, and pressures remain fixed. The current density, fuel utilization, and air ratio also remain fixed.

Figure 4.2 presents the mesh-independence results. Based on these results, the 40-mode mesh appears to be adequate. That is, the distributions vary only slightly between the 40-node mesh and the 80-node mesh, suggesting that refinement beyond 40 nodes is unnecessary.

Notice, however, that the PEN temperature gradient associated with the 40-node mesh falls slightly below that associated with the 80 node-mesh near the fuel cell inlet ($\approx 1$ cm). (The high temperature gradient at this location results from the endothermic reforming reaction.) The 40-node mesh thus underestimates the temperature gradient and could provide misleading results when calculating the fuel cell's thermal stresses. The present study, however, is primarily concerned with the PEN temperature, which appears in the balance equations discussed in Chapter 3. The present model does not calculate the thermal stresses. Because the PEN temperature is ultimately the value sought, and Fig. 4.2a clearly demonstrates the PEN temperature's mesh-independence, the 40-node mesh is considered acceptable. Interestingly, models similar to the present use only 10 or 20 nodes [23,96]. Braun [96], for instance, found 20 nodes to be acceptable. Adopting Braun's choice of convection area in the present model does, indeed, yield a more even (parabolic) temperature gradient distribution.

The overall mass and energy balances provide an additional check on the model. Braun's methodology is again used here [96]. The overall mass balance applied to a single channel is given by the following equation:

$$\dot{m}_{\text{f,inlet}} + \dot{m}_{\text{a,inlet}} = \dot{m}_{\text{f,exit}} + \dot{m}_{\text{a,exit}} + \Delta\dot{m} \tag{4.1}$$

where $\dot{m}_{\text{f,inlet}}$ and $\dot{m}_{\text{a,inlet}}$ are the inlet fuel and air mass flow rates, respectively, and $\dot{m}_{\text{f,exit}}$ and $\dot{m}_{\text{a,exit}}$ are the exit fuel and air mass flow rates, respectively. The corresponding mass balance error is given by:

$$\varepsilon_{\text{mass}} = \left( \frac{\Delta\dot{m}}{\dot{m}_{\text{f,inlet}} + \dot{m}_{\text{a,inlet}}} \right) \times 100\% \tag{4.2}$$

Similarly, the overall energy balance applied to a single channel is given by the following equation:

$$\sum_i \dot{n}_i \overline{h}_{\text{f,inlet},i} + \sum_i \dot{n}_i \overline{h}_{\text{a,inlet},i} = \sum_i \dot{n}_i \overline{h}_{\text{f,exit},i} + \sum_i \dot{n}_i \overline{h}_{\text{a,exit},i} + \dot{W}_{\text{check}} \tag{4.3}$$

where $\overline{h}_{\text{f,inlet},i}$ and $\overline{h}_{\text{a,inlet},i}$ are the inlet fuel and air enthalpies of species $i$, respectively, $\overline{h}_{\text{f,exit},i}$ and $\overline{h}_{\text{a,exit},i}$ are the exit enthalpies of species $i$, respectively, and $\dot{W}_{\text{check}}$ is the check on the power. The corresponding energy balance error is given by:

$$\varepsilon_{\text{energy}} = \left( \frac{\dot{W}_{\text{calculated}} - \dot{W}_{\text{check}}}{\dot{W}_{\text{check}}} \right) \times 100\% \tag{4.4}$$

where $\dot{W}_{\text{calculated}}$ is the power calculated by the model. The overall mass and energy balances both yield reasonably small errors. The overall mass balance yields an error of $4.42 \times 10^{-5}\%$. The overall energy balance yields an error of $1.68 \times 10^{-17}\%$, which is round-off sized.

## 4.3 STEADY-STATE VERIFICATION

The IEA's Program of R, D & D on Advanced Fuel Cells [142] serves as a benchmark case for verifying the fuel cell's steady-state performance. In the IEA study (Annex II: Modelling and Evaluation of Advanced Solid Oxide Fuel Cells, Benchmark Test #2), participants simulated the steady-state operation of an internal-reforming, planar SOFC. Nine institutions participated in the 1996 benchmark study, all of whom calculated the fuel cell's power and operating voltage, as well as the current density and temperature distributions. Each participant developed their own model, and in order to ensure consistency across the different models, the participants adopted a common set of modeling assumptions. In particular, the participants modeled a single, adiabatic cell, and they neglected interactions between the cell and container. The participants also adopted a common cell geometry and set of material properties. The geometry and material properties are provided in Tables 4.1 and 4.2 of this work, respectively. Overall, the participants' results agreed well internally. Hence, the performance of the presentSOFC model, operating under identical (or similar) assumptions, would be expected to fall within (or come reasonably close to) the ranges of results in the IEA study.

The IEA's operating conditions are presented in Table 4.3. Such operating conditions are typical of high-temperature SOFCs. Excess air is provided to cool the cell, and the fuel utilization is specified to be 85%, thus avoiding concentration losses due to fuel overconsumption while also maintaining a reasonably high fuel cell efficiency. In addition, the water-gas shift reaction is assumed to be in equilibrium, and the reforming reaction rate is calculated using the Arrhenius-type equation provided by Achenbach and Riensche [132]. It should be mentioned, however, that slight differences exist between the modeling assumptions adopted by the IEA study and the present work. In particular, the IEA study considered the electro-

chemical oxidation of both $H_2$ and CO. The present study, on the other hand, considers the oxidation of $H_2$ alone. The IEA study also assumed that the activation polarization equaled the electrolyte's ohmic polarization. The present study, however, uses equations presented in the literature to calculate the activation polarization, as discussed in Chapter 3. The present study also includes an estimate of 0.25 ohm $\cdot$ cm$^2$ for the contact resistance (also discussed in Chapter 3). Besides these differences, the present model's assumptions are very similar to those presented in the IEA study.

Table 4.4 compares the results from the different studies. This table compares the fuel cell's operating voltage and power, minimum and maximum current density, minimum and maximum PEN temperature, and the exit gas temperatures from the present model to those from the benchmark study. It is evident from this comparison that the current density, PEN temperature, and exit gas temperatures fall well within the expected ranges. The operating voltage and power, on the other hand, fall slightly below the expected range. This finding is indicative of larger polarizations (lower efficiency) in the present model as compared to the benchmark study. The relatively low power and voltage may be attributed to the use of different polarization models in the present study. The present model, that is, includes an estimate for the contact resistance (0.25 ohm $\cdot$ cm$^2$), whereas the IEA benchmark study makes no mention of contact resistance. The present model also uses different equations for modeling the activation polarizations, whereas the benchmark study sets the activation polarizations equal to the electrolyte's ohmic polarization. As it turns out, reducing the contact resistance and equating the activation polarization to the ohmic polarization in the present model was found to influence the fuel cell's operating voltage and power, producing slightly higher values than those in the benchmark study. Braun [96], who included only the ohmic resistance and neglected the activation, concentration, and contact resistances, also obtained values for the operating voltage and power slightly above the benchmark study's range. Thus, the present model is considered to be reasonably accurate, given the differences in modeling assumptions.

**Table 4.3** Operating parameters used during the SOFC's steady-state and dynamic verification. The steady-state operating parameters come from the IEA benchmark study [132]. The dynamic operating parameters come from both Wang and Nehrir [68] and the IEA benchmark study [132].

| Parameter | Operation | |
|---|---|---|
| | Steady-state | Dynamic |
| Flow configuration | Co-flow | Co-flow |
| Inlet bulk pressure (fuel and air) | 1 bar | 3 atm |
| Inlet temperature (fuel and air) | 1173 K | 1173 K |
| Inlet fuel composition | $CH_4 = 17.10\%$ | $CH_4 = 17.10\%$[a] |
| | $H_2 = 26.26\%$ | $H_2 = 26.26\%$ |
| | $H_2O = 49.34\%$ | $H_2O = 49.34\%$ |
| | $CO = 2.94\%$ | $CO = 2.94\%$ |
| | $CO_2 = 4.36\%$ | $CO_2 = 4.36\%$ |
| Inlet air composition | $O_2 = 21\%$ | $O_2 = 21\%$ |
| | $N_2 = 79\%$ | $N_2 = 79\%$ |
| Fuel utilization ($U_{f,1}$) | 85% | - |
| Air ratio | 7 | 6 |
| Inlet fuel flow rate | - | $2.834 \times 10^{-6}$ kg/s[b] |
| Mean current density | 3000 A/m$^2$ | 3000 A/m$^2$ (initially)[c] |

[a] Wang and Nehrir assumed an inlet fuel composition of 90% $H_2$ and 10% $H_2O$ (molar basis).
[b] The fuel flow rate for the dynamic simulations is determined based on the results of the steady-state simulation (Wang and Nehrir instead specify a fuel flow rate of 0.096 mol/s).
[c] Wang and Nehrir specified current, but not current density (or electrochemically active area).

**Table 4.4** Comparison of SOFC model's results to IEA's results.

| Variable | IEA | Model |
|---|---|---|
| Operating voltage (V) | 0.633–0.649 | 0.596 |
| Power (W) | 18.99–19.47 | 17.43 |
| Current density ($mA/cm^2$) | | |
| Minimum | 101.0–238.2 | 194.1 |
| Maximum | 304.0–366.5 | 348.9 |
| PEN temperature (K) | | |
| Minimum | 1100.15–1135.15 | 1105 |
| Maximum | 1294.15–1307.15 | 1297 |
| Exit fuel temperature (K) | 1294.15–1299.15 | 1297 |
| Exit air temperature (K) | 1289.15–1299.15 | 1292 |

## 4.4 DYNAMIC VERIFICATION

The study performed by Wang and Nehrir [68] serves as a benchmark case for verifying the present model's dynamic behavior. Wang and Nehrir developed a dynamic, tubular, pressurized SOFC model based on electrochemical, species mass balance, and energy balance equations. These authors investigated the voltage response of the SOFC to step changes in the current density on small, medium, and large timescales, corresponding to electrochemical, mass flow, and thermal processes, respectively. The operating conditions adopted in the present study are presented in Table 4.3. The flow configuration, inlet gas temperatures and pressures, and the air ratio are identical to those of Wang and Nehrir. The inlet fuel composition, fuel flow rate, and the current density, on the other hand, are based on the IEA benchmark study (and the results thereof), as the corresponding conditions were either not specified by Wang and Nehrir, or they were not appropriate for use in the present model. Throughout this section, the settling time is estimated as the time required for the SOFC operating voltage to reach a uniform (constant-slope) profile after experiencing a step change in the current density. Figures 4.3–4.5 present the voltage responses of the SOFC model. Settling times estimated from Wang and Nehrir's results are indicated by red, dashed lines

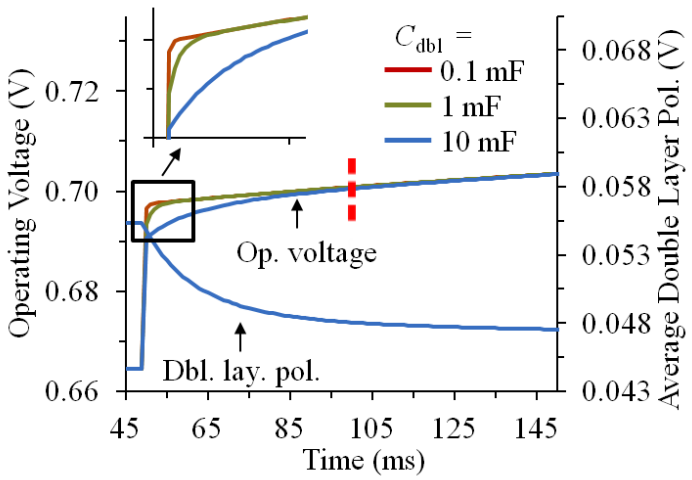


**Figure 4.3** Electrochemical voltage response. The red, dashed line indicates the estimated electrochemical voltage response time from Wang and Nehrir's results. The double layer polarization (axially averaged) is shown for $C_{\text{dbl}} = 10$ mF.

for comparison with the present model. In addition, as part of each simulation, a quantity is shown indicating the physical process associated with each transient phenomenon.

The model's electrochemical voltage response is shown in Fig. 4.3. The current density decreases from 3000 A/m$^2$ to 2500 A/m$^2$ at 50 ms, and the double layer capacitance is varied between 0.1 mF and 10 mF. The electrochemical voltage settling time for $C_{\text{dbl}} = 10$ mF is found to be approximately 50 ms. This result agrees with the settling time obtained by Wang and Nehrir, who also found a settling time of approximately 50 ms [68]. Notice, also, that the voltage settling time is very close to the double layer polarization settling time, indicating that the charge double layer is associated with the SOFC's dynamic behavior on the electrochemical timescale. It can furthermore be seen from Fig. 4.3 that the shape of the voltage profile depends on the value of the double layer capacitance. Higher values of the double layer capacitance lead to smoother (flatter) voltage profiles. This result also agrees with that of Wang and Nehrir. Finally, notice that the charge double layer polarization continues to increase even after settling has occurred. This longer transient behavior likely demarcates the beginning of the mass flow dynamic response, which characteristically occurs on the second timescale.

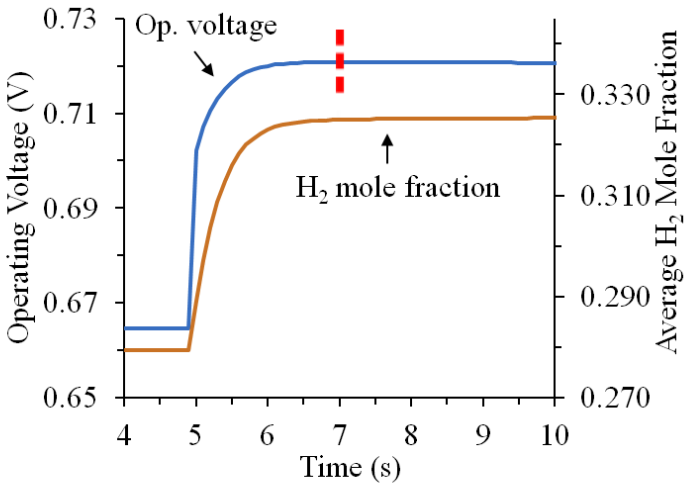


**Figure 4.4** Mass flow voltage response. The red, dashed line indicates the mass flow voltage settling time estimated from Wang and Nehrir's results. The $H_2$ mole fraction (axially averaged) is also shown.

The model's mass flow voltage response is shown in Fig. 4.4. The current density decreases from 3000 A/m$^2$ to 2500 A/m$^2$ at 5 sec. The mass flow voltage settling time is found to be approximately 2 sec. The mass flow voltage settling time estimated from Wang and Nehrir's results is also approximately 2 sec. [68]. Evidently, differences in the inlet fuel composition, while leading to different reactions inside the fuel cell (particularly the steam reforming and water-gas shift reactions), yields a negligible effect in terms of the mass flow voltage settling time. The choice of discretized vs. single-node domains also yields a negligible effect on the results, as Wang and Nehrir's model included only a single node, while the present model discretizes the domain along the flow path. Notice, also, that the voltage settling time is very close to the $H_2$ mole fraction settling time, indicating that the change in the gas composition is associated with the SOFC's dynamic behavior on this timescale.

Finally, the fuel cell's thermal voltage response is shown in Fig. 4.5. The current density decreases from 3000 A/m$^2$ to 2500 A/m$^2$ at 3000 sec. (50 min.). The thermal voltage settling time is approximately 600 sec. (10 min.). The thermal voltage settling time estimated from Wang and Nehrir's results, on the other hand, is approximately 1500 sec. (25 min.). One possible explanation for this discrepancy is the choice of fuel. The reforming reaction is

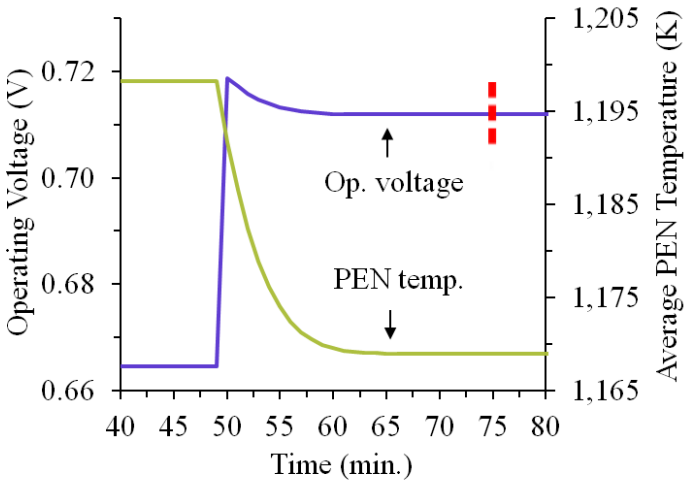


**Figure 4.5** Thermal voltage response. The red, dashed line indicates the thermal voltage settling time estimated from Wang and Nehrir's results. The PEN temperature (axially averaged) is also shown.

highly endothermic, leading to faster thermal settling times when the temperature is reduced (i.e., the load is decreased). Wang and Nehrir assumed an inlet fuel composition of $H_2$ and $H_2O$, whereas the present study assumed a pre-reformed fuel mixture, which then undergoes internal reforming. This difference may help to explain why Wang and Nehrir's results exhibit a significantly slower thermal settling time compared to the present study. Martinez, et al. [23] observed a similar phenomenon. These authors compared the performance of an $H_2$-fueled SOFC system to that of a natural gas-fed system, finding that the $H_2$-fueled system exhibited larger overshoots than the natural gas system during load decreases. Notice, also, that the thermal voltage settling time of the present model is very close to the average PEN temperature settling time, indicating that the average PEN temperature is associated the SOFC's dynamic behavior on this timescale.

## 4.5 SUMMARY

This chapter performed several checks on the SOFC model prior to simulation in later chapters. In particular, the present chapter demonstrated the fuel cell's mesh-independence. The PEN temperature, current density, composition, and PEN temperature gradient distribution exhibited only slight changes beyond 40 nodes. The present chapter also verified the SOFC model during both steady-state and dynamic operation. During steady-state operation, results from the model agree reasonably well with those from the benchmark case. Slight differences in the power and voltage likely arise from different polarization models. During dynamic operation, the fuel cell exhibits electrochemical (fast), mass flow (slower), and thermal (slowest) settling times that are on the same order of magnitude as those obtained by Wang and Nehrir [68]. The present model's shorter settling times on the thermal timescale likely arise from the endothermic reforming reaction. In the next chapter, the fuel cell model is incorporated into two larger system models.

# 5.0 SYSTEM AND COST MODELS

This chapter integrates the fuel cell stack with two potential overall systems. The hybrid system integrates the previously developed solid oxide fuel cell (SOFC) model with a microturbine. The SOFC stack replaces a conventional microturbine's combustor, and the SOFC stack's exhaust drives the turbine. The non-hybrid system, on the other hand, relies on the SOFC stack as its sole power source. The stack operates at near-atmospheric pressure, and the system's exhaust exits the system soon after leaving the fuel cell stack. Both systems generate constant power to meet a university building's baseload demand. The systems also cogenerate thermal energy to help meet the building's hot water demand. Finally, the cost model calculates the life cycle costs associated with the hybrid and non-hybrid systems during baseload operation. The life cycle costs include capital, operating, and maintenance costs. The results from these models are presented in Chapter 8.

## 5.1 FUEL CELL STACK

The SOFC stack serves as the main prime mover for meeting the building's baseload demand. In the SOFC stack model, multiple SOFCs are electrically connected in series, as shown in Fig. 5.1. Bipolar plates, or interconnect, electrically connect the SOFCs. In the present model, the performance of a single SOFC is linearly scaled up to the stack level. In other words, it is assumed that each fuel cell in the stack performs identically, thus neglecting cell-to-cell variations. The SOFC stack model furthermore accounts for thermal radiation exchange between the stack's high-temperature, ceramic surfaces and the stack's container. The stack's surface is assumed to be opaque, gray, and diffuse with an emissivity of $\varepsilon = 0.8$

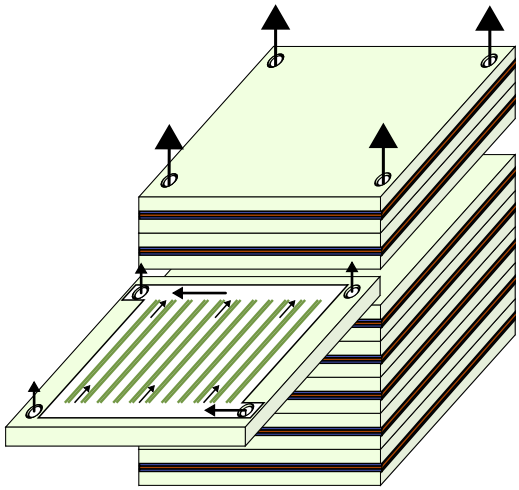

**Figure 5.1** SOFC stack showing individual SOFC.

[127]. The container is typically made of a metal alloy that is heated to approximately 650°C during operation. The container's geometry resembles a cavity that approximates a blackbody [143]. Accordingly, the surface energy balance applied to the stack results in the following formula for the net rate at which thermal energy leaves the stack due to radiation exchange:

$$q_{\text{stack}} = A_{\text{stack}} \varepsilon_{\text{stack}} \sigma (T_{\text{cell}}^4 - T_{\text{container}}^4) \tag{5.1}$$

where $A_{\text{stack}}$ is the stack's surface area, $\varepsilon_{\text{stack}}$ is the emissivity of the stack, $\sigma$ is the Stefan-Boltzmann constant, $T_{\text{cell}}$ is the SOFC's (interconnect's, electrode's, and electrolyte's) temperature, and $T_{\text{ccontainer}}$ is the container's temperature [122]. The stack model treats Eqn. (5.1) as a boundary condition. Hence, Eqn. (5.1) is applied at the inlet and exit of the solid material energy balance equations. The stack surface area in Eqn. (5.1) corresponds to the dimensions of the inlet and exit solid material. (It should be mentioned here that radiation between the fuel cell stack and container is not included in the system models, as the radiation boundary condition gave rise to an unreasonably small air temperature change.)

The SOFC stack model also accounts for heat transfer between adjacent SOFCs. The interconnect conducts and convects thermal energy between fuel and air channels belonging to adjacent fuel cells in the stack. This type of heat transfer, which shall be termed "cross-

channel heat transfer," differs from intra-channel convection, which has already been included in the gas channel energy balance equation (Eqn. (3.40) in Chapter 3). That is, cross-channel heat transfer occurs between adjacent fuel cells, whereas intra-channel convection occurs within a single fuel cell between the solid material and bulk flow. Cross-channel effects are calculated using the following equation, which is based on a thermal resistance network:

$$q_{\text{cross-channel}} = \frac{T_{\text{f}} - T_{\text{a}}}{1//h_{\text{f}}A_{\text{f}} + 1/k_{\text{PEN}}S + 1/h_{\text{a}}A_{\text{a}}} \tag{5.2}$$

where $A_{\text{f}}$ and $A_{\text{a}}$ are the surface areas of the anode and cathode channel walls, and $S$ is a shape factor that accounts for the 2-D heat flux through the interconnect [96, 122]. Using numerical analysis, Braun [96] calculated that $S = 0.019$ m. This value is adopted in the present work.

In the hybrid and non-hybrid systems, the fuel cell's dimensions are modified slightly from those presented in Chapter 3. In particular, the fuel cell's design is changed from an electrolyte-supported design, in which the electrolyte forms the thickest component, to an anode-supported design, meaning that the electrolyte is made relatively thin, and the thicker anode provides structural support. Anode-supported fuel cells typically operate at relatively low temperatures (e.g., 800°C), thereby permitting the use of metallic interconnects. The use of metallic interconnects reduces the fuel cell stack's cost (the cost model presented in Section 5.5 adopts the U.S. Department of Energy's SOFC cost goal of \$175/kW of net plant power). Electrolyte-supported fuel cells, on the other hand, operate at higher temperatures to minimize ohmic losses, necessitating the use of more expensive ceramic interconnects [43, 73]. Thijssen [144] provides typical dimensions for anode-supported fuel cells. The present work adopts these values. The anode is 325 $\mu$m thick, the electrolyte is 8 $\mu$m thick, and the cathode is 50 $\mu$m thick. Also, the interconnect's thermal conductivity is 30 W/m·K, representative of stainless steel interconnects [73, 96].

## 5.2 BALANCE OF PLANT COMPONENTS

The present work models the balance-of-plant (BoP) components. Each BoP component model consists of mass and energy balances that account for changes in a fluid's composition and temperature as the species interact chemically and thermally throughout the system. Steady-state operation is assumed. Each component also includes a pressure drop. The pressure drop values are assumed to remain constant, regardless of the system's operating point, and the values are based on previous studies. The component models are developed in Engineering Equation Solver (EES), which is the same software used to model the fuel cell stack. EES provides built-in thermodynamic properties, such as enthalpy and entropy, thus facilitating the model's solution. The BoP models are discussed in more detail in the following subsections.

### 5.2.1 Rotating Equipment

The air blower, air compressor, fuel compressor, and turbine are all rotating equipment. These devices increase (or decrease) a fluid's enthalpy by producing (or consuming) shaft power. Enthalpy is defined as the sum of a fluid's internal energy and the product of its pressure and volume (i.e., $\overline{h} = \overline{u} + p\overline{v}$). The enthalpy of an ideal gas mixture is given by the following formula:

$$\overline{h} = \sum_{i}^{n} y_i \overline{h}_i \tag{5.3}$$

where $\overline{h}$ is the mixture's molar enthalpy, $y_i$ is the mole fraction of species $i$, $\overline{h}_i$ is the molar enthalpy of species $i$, and $n$ is the number of species [49]. The air blower, air compressor, and fuel compressor increase the fluid's enthalpy by increasing the fluid's pressure and temperature. Compression requires a power input, which is supplied by the shaft-connected turbine (in the case of the air compressor) or an electric motor (in the case of the air blower and fuel compressor). The turbine, on the other hand, decreases the fluid's enthalpy from inlet to exit. The fluid rotates a shaft, producing mechanical power that drives a generator. In the case of the microturbine, the turbine generates sufficient power to both drive the compressor and provide net power to a load. Figure 5.2 presents the symbols representing each rotating

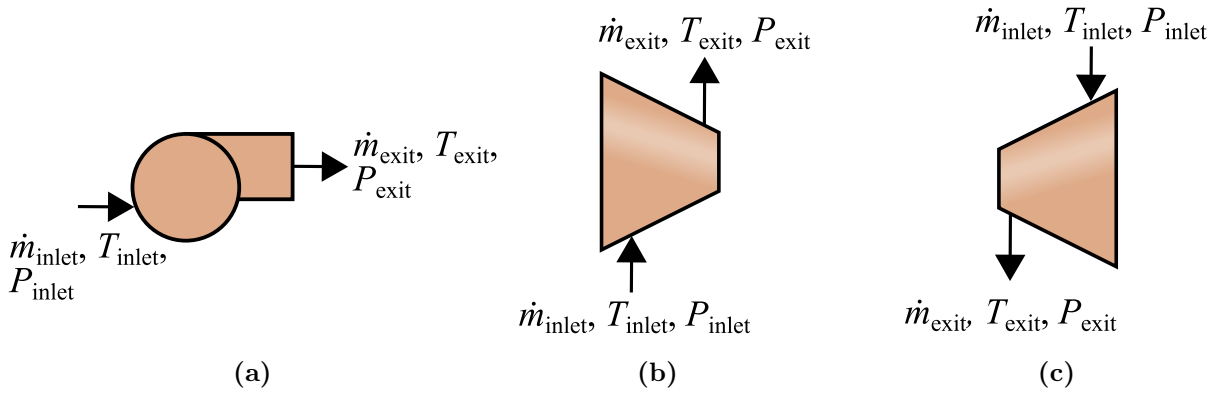


**Figure 5.2** Rotating equipment symbols: (a) Air blower and fuel compressor symbols, (b) Air compressor symbol, (c) Turbine symbol.

device. These devices are assumed to operate adiabatically, and the changes in potential and kinetic energies are neglected. The inlet mass flow rate, temperature, and pressure are generally known, and the models calculate the corresponding exit quantities.

The mass and energy balances calculate the exiting fluid's composition and temperature, respectively. The rotating devices are non-reacting. Thus, the species molar flow rates remain constant through these devices:

$$\dot{n}_{i,\text{inlet}} = \dot{n}_{i,\text{exit}} = \dot{n} \tag{5.4}$$

where $\dot{n}_{i,\text{inlet}}$ is the inlet molar flow rate of species $i$, and $\dot{n}_{i,\text{exit}}$ is the exit molar flow rate of species $i$. Furthermore, the energy balance yields the device's exit temperature based on the known inlet temperature and pressure ratio. The energy balance applied to the air blower, air compressor, and fuel compressor is expressed as follows:

$$T_{\text{exit}} = T_{\text{inlet}} + \frac{T_{\text{inlet}}}{\eta_{\text{blow(comp)}}} \left( \left( \frac{p_{\text{exit}}}{p_{\text{inlet}}} \right)^{\frac{\overline{R}}{\overline{c}_{\text{p}}}} - 1 \right) \tag{5.5}$$

where $T_{\text{exit}}$ is the exit temperature, $T_{\text{inlet}}$ is the inlet temperature, $\eta_{\text{blow(comp)}}$ is the blower's (or compressor's) isentropic efficiency, $p_{\text{exit}}$ is the exit pressure, $p_{\text{inlet}}$ is the inlet pressure, $\overline{R}$ is the universal gas constant, and $\overline{c}_{\text{p}}$ is the molar specific heat capacity of the ideal gas

mixture. The power consumed by the air blower, air compressor, and fuel compressor equals the change in enthalpy across these devices:

$$\dot{W}_{\text{blow(comp)}} = \dot{n}\left(\overline{h}_{\text{exit}} - \overline{h}_{\text{inlet}}\right) \tag{5.6}$$

where $\dot{W}_{\text{blow(comp)}}$ is the power consumed by the blower (or compressor), positively defined. The turbine model consists of similar governing equations. The energy balance applied to the turbine is given by the following formula, again, assuming ideal gas behavior:

$$T_{\text{exit}} = T_{\text{inlet}} - \eta_{\text{turb}} T_{\text{inlet}} \left( \left( \frac{p_{\text{exit}}}{p_{\text{inlet}}} \right)^{\frac{\overline{R}}{\overline{c}_{\text{p}}}} - 1 \right) \tag{5.7}$$

where $\eta_{\text{turb}}$ is the turbine's isentropic efficiency. The power generated by the turbine is similar to that of the compressors and air blower but with opposite sign:

$$\dot{W}_{\text{turb}} = \dot{n}\left(\overline{h}_{\text{inlet}} - \overline{h}_{\text{exit}}\right) \tag{5.8}$$

where $\dot{W}_{\text{turb}}$ is the power generated by the turbine, positively defined [49].

### 5.2.2 Desulfurizer

The desulfurizer removes sulfur from the natural gas. Utilities add sulfur to natural gas as an odorant to detect leaks. Sulfur poses a risk to fuel cell systems, however, as it deactivates the methane steam reforming and water-gas shift reaction catalysts [26]. Typically, sulfur poisons SOFC anodes at concentrations greater than 1 part per million (by volume) at high operating temperatures (e.g., 1000°C). At lower operating temperatures (e.g., 750°C), the anode's sulfur tolerance decreases to nearly 10 parts per billion (by volume). To desulfurize the natural gas, systems often include a bed of zinc oxide (ZnO) prior to the pre-reformer. The ZnO absorbs hydrogen sulfide ($H_2S$) at approximately 350°C [44]. In the present model, the desulfurizer is simply treated as a pressure drop. Hence, the mass flow rate and temperature remain constant, and the reactions inside the desulfurizer are not modeled. Figure 5.3 presents the symbol representing the desulfurizer.


**Figure 5.3** Desulfurizer symbol.

### 5.2.3 Air Pre-Heater

The air pre-heater transfers thermal energy from the system's exhaust to the incoming air. Figure 5.4 presents the symbol representing the air pre-heater. The air pre-heater operates in counter-flow (even though the symbol illustrates cross-flow operation, for compactness). The variables $\dot{m}_{\text{exhst,inlet}}$, $T_{\text{exhst,inlet}}$, and $p_{\text{exhst,inlet}}$ denote the exhaust's inlet mass flow rate, temperature, and pressure, respectively (and similar for the exit properties). The variables $\dot{m}_{\text{air,inlet}}$, $T_{\text{air,inlet}}$, and $p_{\text{air,inlet}}$ denote the air's inlet mass flow rate, temperature, and pressure, respectively. The air pre-heater operates adiabatically. Accordingly, the rate of heat transfer between the hot and cold fluids is given by the following formula:

$$q_{\text{preheat}} = \dot{n}\left(\overline{h}_{\text{air,exit}} - \overline{h}_{\text{air,inlet}}\right) \tag{5.9}$$

The rate of heat transfer may alternatively be expressed in terms of the hot fluid's inlet and exit enthalpies:

$$q_{\text{preheat}} = \dot{n}\left(\overline{h}_{\text{exhst,inlet}} - \overline{h}_{\text{exhst,exit}}\right) \tag{5.10}$$

Generally, the air's exit temperature and both fluids' inlet temperatures are known, and Eqns. (5.9) and (5.10) provide the exhaust's exit temperature [122].

The air pre-heater model also calculates the air pre-heater's $UA$ product. The $UA$ product is the product of the air pre-heater's overall heat transfer coefficient ($U$) and its heat exchange area ($A$). The $UA$ product provides an indication of the heat exchanger's size, which is used in the cost model to estimate the air pre-heater's capital cost. The log mean temperature difference relates the $UA$ product to the air pre-heater's rate of heat transfer as follows:

$$q = UA\Delta T_{\text{lm}} \tag{5.11}$$

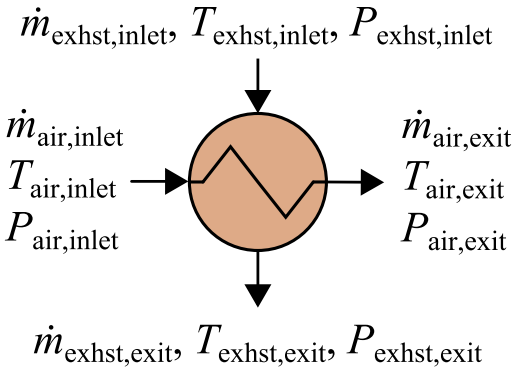


**Figure 5.4** Air pre-heater symbol.

where $\Delta T_{\text{lm}}$ is the log mean temperature difference. The log mean temperature difference is defined as follows:

$$\Delta T_{\text{lm}} = \frac{\Delta T_2 - \Delta T_1}{\ln\left(\Delta T_2 / \Delta T_1\right)} \tag{5.12}$$

For the counter-flow heat exchanger considered herein, $\Delta T_1$ and $\Delta T_2$ are given by the following equations:

$$\Delta T_1 = T_{\text{exhst,inlet}} - T_{\text{air,inlet}} \tag{5.13}$$

$$\Delta T_2 = T_{\text{exhst,exit}} - T_{\text{air,exit}} \tag{5.14}$$

The rate of heat transfer appearing in Eqns. (5.9) and (5.10), combined with the log mean temperature difference in (5.12), yields the $UA$ product [122].

### 5.2.4 Pre-Reformer

The pre-reformer converts $CH_4$ into a mixture of $H_2$, $H_2O$, CO, and $CO_2$ prior to entering the fuel cell stack. Often, a portion of $CH_4$ remains in the reformate, depending on the extent of pre-reforming. Figure 5.5 presents the symbol representing the pre-reformer. The pre-reformer model is based on the model developed by Braun [96]. The model accounts for

the methane steam reforming and water-gas shift reactions, and the pre-reformer operates adiabatically. The methane steam reforming reaction is given by the following equation:

$$\mathrm{CH_4 + S/C \cdot H_2O \longrightarrow (1 - x_{reform})CH_4 + (S/C - x_{reform}) \cdot H_2O + x_{reform} 3H_2 + x_{reform} CO} \quad (5.15)$$

where S/C is the steam-to-carbon ratio, or the ratio of the number of moles of $H_2O$ to the number of moles of $CH_4$ at the pre-reformer's inlet, and $x_{\text{reform}}$ is the extent of methane steam reforming. Based on the reactants' molar flow rates and the stoichiometry in Eqn. 5.15, the model calculates the molar flow rates exiting the pre-reformer.

The water-gas shift reaction is assumed to be in equilibrium. The water-gas shift reaction is given by:

$$\mathrm{CO + H_2O \longleftrightarrow CO_2 + H_2} \quad (5.16)$$

The following atom balances yield the molar flow rates of the water-gas shift products:

$$\text{Carbon:} \quad \dot{n}_{\mathrm{CO,wgs}} + \dot{n}_{\mathrm{CO_2,wgs}} = \dot{n}_{\mathrm{CO,msr}} + \dot{n}_{\mathrm{CO_2,msr}} \quad (5.17)$$

$$\text{Hydrogen:} \quad \dot{n}_{\mathrm{H_2,wgs}} + \dot{n}_{\mathrm{H_2O,wgs}} = \dot{n}_{\mathrm{H_2,msr}} + \dot{n}_{\mathrm{H_2O,msr}} \quad (5.18)$$

$$\text{Oxygen:} \quad \dot{n}_{\mathrm{CO,wgs}} + \dot{n}_{\mathrm{CO_2,wgs}} + \dot{n}_{\mathrm{H_2O,wgs}} = \dot{n}_{\mathrm{CO,msr}} + \dot{n}_{\mathrm{CO_2,msr}} + \dot{n}_{\mathrm{H_2O,msr}} \quad (5.19)$$

$$\text{Methane:} \quad \dot{n}_{\mathrm{CH_4,wgs}} = \dot{n}_{\mathrm{CH_4,msr}} \quad (5.20)$$

where $\dot{n}_{i,\text{msr}}$ is the molar flow rates of species $i$ yielded by the methane steam reforming reaction, and $\dot{n}_{i,\text{wgs}}$ is the molar flow rate of species $i$ yielded by the water-gas shift reaction. The water-gas shift reaction's equilibrium constant is given by:

$$\ln\left(K_{\text{wgs}}\right) = -\frac{\Delta\overline{g}^{\circ}_{\text{wgs}}(T_{\text{reform}})}{\overline{R}T_{\text{reform}}} \quad (5.21)$$

where $K_{\text{wgs}}$ is the equilibrium constant, and $\Delta\overline{g}^{\circ}(T_{\text{reform}})$ is the change in molar Gibbs free energy evaluated at standard pressure and the pre-reformer's temperature. The equilibrium constant is also expressed in terms of the product and reactant mole fractions:

$$K_{\text{wgs}} = \frac{y_{\mathrm{H_2}} y_{\mathrm{CO_2}}}{y_{\mathrm{H_2O}} y_{\mathrm{CO}}} \quad (5.22)$$

where $y_i$ is the mole fraction of species $i$ [49]. Solving Eqns. (5.15) and (5.17)–(5.22) yields the pre-reformer's exit (SOFC's inlet) composition.

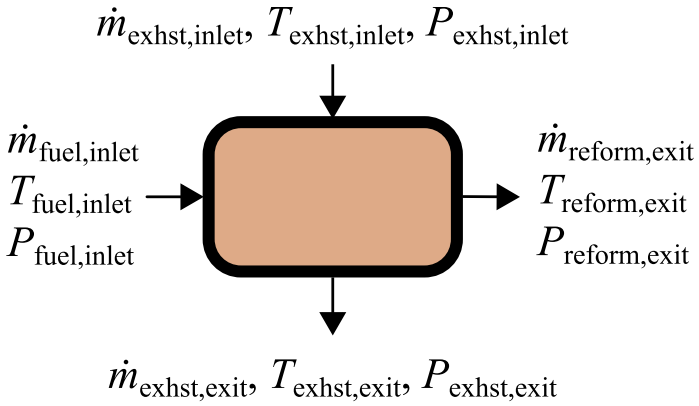


**Figure 5.5** Pre-reformer symbol.

The pre-reformer also pre-heats the fuel. The system's exhaust provides the thermal energy required to meet the SOFC stack's inlet temperature. The following energy balance provides the amount of thermal energy transferred between the system's exhaust and the pre-reformer:

$$q_{\text{reform}} = \dot{n}\left(\overline{h}_{\text{reform,exit}} - \overline{h}_{\text{fuel,inlet}}\right) \tag{5.23}$$

The rate of heat transfer is alternatively be expressed in terms of the exhaust's inlet and exit enthalpies:

$$q_{\text{reform}} = \dot{n}\left(\overline{h}_{\text{exhst,inlet}} - \overline{h}_{\text{exhst,exit}}\right) \tag{5.24}$$

The reformate's exit temperature (SOFC stack's inlet temperature) and the fuel's and exhaust's inlet temperatures are generally known, and the pre-reformer model calculates the reformate's exit temperature.

### 5.2.5 Heat Recovery Heat Exchanger

The heat recovery heat exchanger recovers thermal energy from the system's exhaust. The present study assumes that all thermal energy recovered is utilized for hot water heating (although the building's hot water loop is not modeled). The thermal energy recovered in the heat recovery heat exchanger is given by the following equation:

$$q_{\text{CHP}} = \dot{n}\left(\overline{h}_{\text{exhst,exit}} - \overline{h}_{\text{exhst,inlet}}\right) \tag{5.25}$$

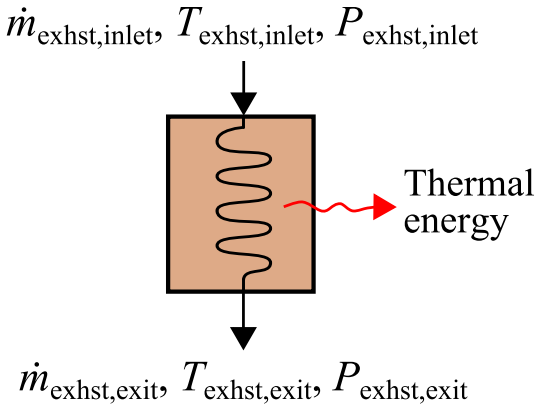


**Figure 5.6** Heat recovery heat exchanger symbol.

The heat recovery heat exchanger's exit temperature is specified to be 25°C above the exhaust's dew point temperature to avoid condensation and corrosion inside the heat exchanger. Also, the heat exchanger's size is assumed to remain fixed, regardless of the system's design point. Consequently, the heat recovery heat exchanger's capital cost remains fixed. Figure 5.6 presents the symbol representing the heat recovery heat exchanger.

### 5.2.6 Auxiliary Combustor

The auxiliary combustor consumes unused fuel exiting the fuel cell stack. Figure 5.7 presents the symbol representing the auxiliary combustor. The model assumes complete combustion. The combustion of the unused fuel is given by the following reactions:

$$\mathrm{H_2} + \tfrac{1}{2}\,\mathrm{O_2} \longrightarrow \mathrm{H_2O} \tag{5.26}$$

$$\mathrm{CO} + \tfrac{1}{2}\,\mathrm{O_2} \longrightarrow \mathrm{CO_2} \tag{5.27}$$

$$\mathrm{CH_4} + 2\,\mathrm{O_2} \longrightarrow \mathrm{CO_2} + 2\,\mathrm{H_2O} \tag{5.28}$$

The inlet molar flow rates and the stoichiometry specified in Eqns. (5.26)–(5.28) determine the exit molar flow rates. The species mass balances are expressed as follows on a molar basis:

$$\dot{n}_{i,\text{exit}} = \dot{n}_{i,\text{inlet}} + \sum_{j}^{3} \nu_{i,j}\dot{r}_j \tag{5.29}$$

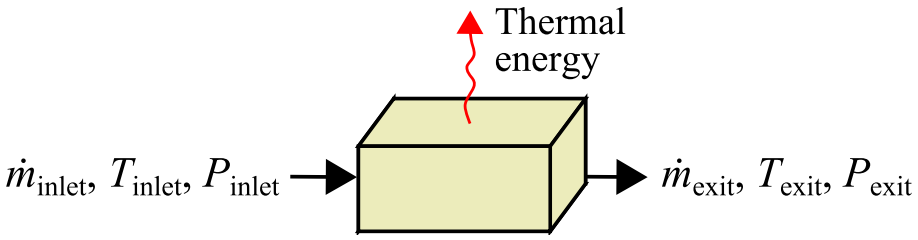


**Figure 5.7** Auxiliary combustor symbol.

where $\dot{n}_{i,\text{exit}}$ is the exit molar flow rate of species $i$, $\dot{n}_{i,\text{inlet}}$ is the inlet molar flow rate of species $i$, $\nu_{i,j}$ is the stoichiometric coefficient of species $i$ in reaction $j$, and $\dot{r}_j$ is the rate of reaction $j$, which is determined by the inlet species molar flow rates and the assumption of complete combustion.

The energy balance accounts for thermal energy loss from the system's hot components, which includes the SOFC stack, air pre-heater, pre-reformer, and auxiliary combustor. The present model assumes that 3% of the inlet fuel's higher heating value is lost to the environment, all of which is lost from the auxiliary combustor (although the heat loss would actually be more spread out among the stack, air pre-heater, pre-reformer, and auxiliary combustor) [56, 94, 95]. The energy balance applied to the auxiliary combustor is given by:

$$\overline{h}_{\text{inlet}} = \overline{h}_{\text{exit}} + q_{\text{loss}} \tag{5.30}$$

The inlet temperatures are known, and the auxiliary combustor model calculates the combustor's exit temperature.

### 5.2.7 Pressure Drops

Pressure drops occur across each BoP component. Braun [56] estimated the pressure drops based on several previous studies [145–147]. The present study adopts Braun's estimates. The BoP pressure drops are presented in Table 5.1. In the hybrid and non-hybrid systems, the total BoP fuel-side pressure drop is 365 mbar, and the total air-side BoP pressure drop is 315 mbar. These values are assumed to remain constant, regardless of the system's operating point. In an actual system, the pressure drops would vary based on the fluid's flow rate.

**Table 5.1** BoP component pressure drops [56].

| Component | Pressure drop (mbar) |
|---|---|
| Desulfurizer | 100 |
| Pre-reformer | 50 |
| Fuel cell stack (fuel side) | 30 |
| Fuel cell stack (air side) | 30 |
| Auxiliary combustor | 20 |
| Air pre-heater | 100 |
| Heat recovery heat exchanger | 15 |

## 5.3 SYSTEM INTEGRATION

The hybrid and non-hybrid systems integrate the SOFC stack with the BoP components. The hybrid system pressurizes the SOFC stack, placing the stack between the compressor and turbine (where the combustor would normally be situated). The SOFC stack generates power electrochemically, and the stack's exhaust drives the microturbine. Zhang, et al. [148] refers to this design as a "direct thermal coupling" scheme, as it involves the exchange of thermal energy between the stack and microturbine by passing the same working fluid from one device to the other. The non-hybrid system, on the other hand, relies on the SOFC stack as its sole power source. The SOFC stack operates at near-atmospheric pressure. Braun [56] considered various non-hybrid system configurations, considering such features as anode gas recycle, cathode gas recycle, internal reforming, and external reforming. The present study adopts Braun's methane-fed, internal reforming design. In both systems, the system's exhaust pre-heats the incoming fuel and air. The heat recovery heat exchanger recovers any remaining thermal energy.

### 5.3.1 Hybrid System

The hybrid system integrates the SOFC stack with a microturbine. Figure 5.8 provides a schematic of the hybrid system. Air enters the air compressor, where it is compressed to the

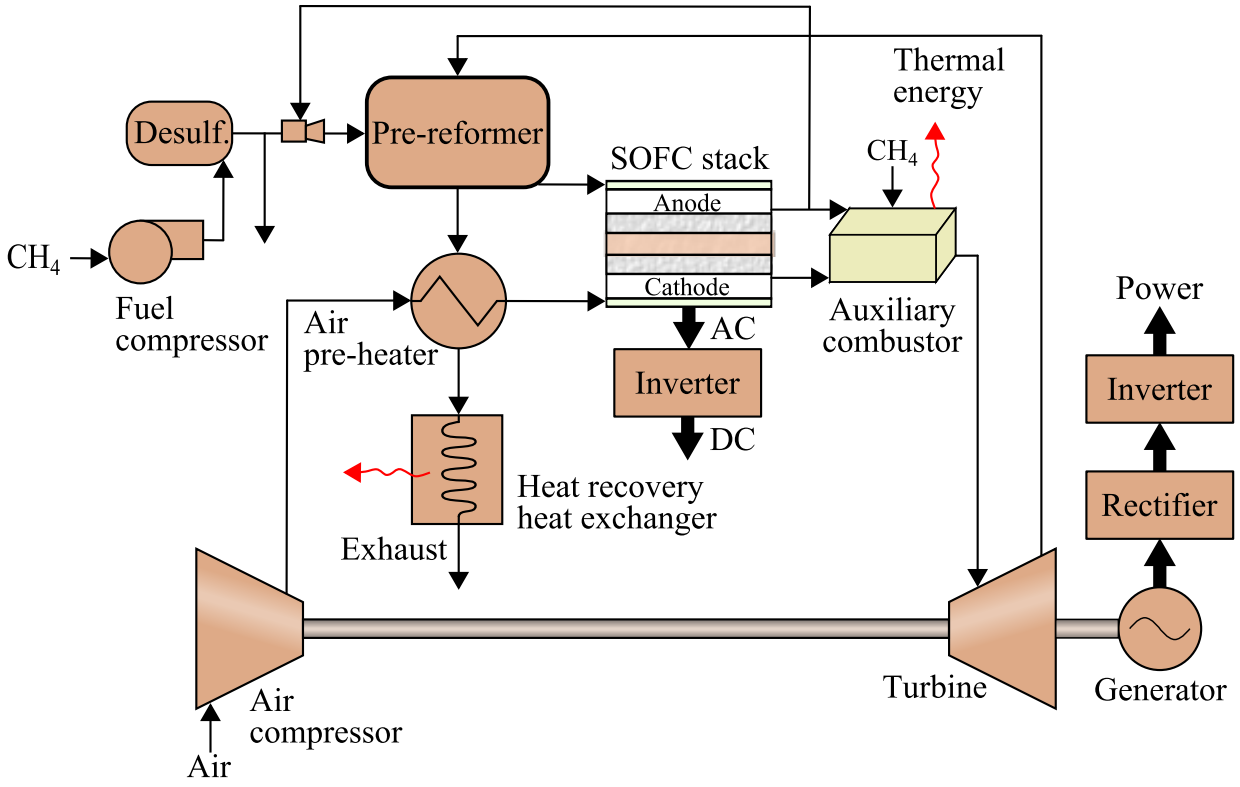


**Figure 5.8** Hybrid system schematic.

fuel cell stack's operating pressure. The air is then pre-heated to a temperature suitable for SOFC operation. Meanwhile, fuel (modeled as pure $CH_4$) enters the fuel compressor, where it is compressed to the SOFC stack's operating pressure. The fuel is desulfurized and enters the pre-reformer, where it is partially converted into $H_2$, $H_2O$, CO, and $CO_2$. The reformate then enters the fuel cell stack, and it reacts electrochemically with the $O_2$. The fuel cell stack generates AC power, which is inverted to DC power. Part of the anode exhaust circulates back to the pre-reformer inlet. The purpose of anode gas recycle is to maintain an S/C ratio of 2 at the pre-reformer's inlet. The S/C ratio of 2 avoids solid carbon formation (or coking) inside the pre-reformer. Coking blocks the Ni-catalyst, inhibiting the reforming reaction. Unused fuel exits the fuel cell stack and reacts with air in the auxiliary combustor. The combustor consumes additional fuel to maintain a 15°C pinch-point temperature difference in the air pre-heater. (The temperature of the exhaust entering the air pre-heater is otherwise too low to provide the thermal energy required for pre-heating the air.) Most of the energy

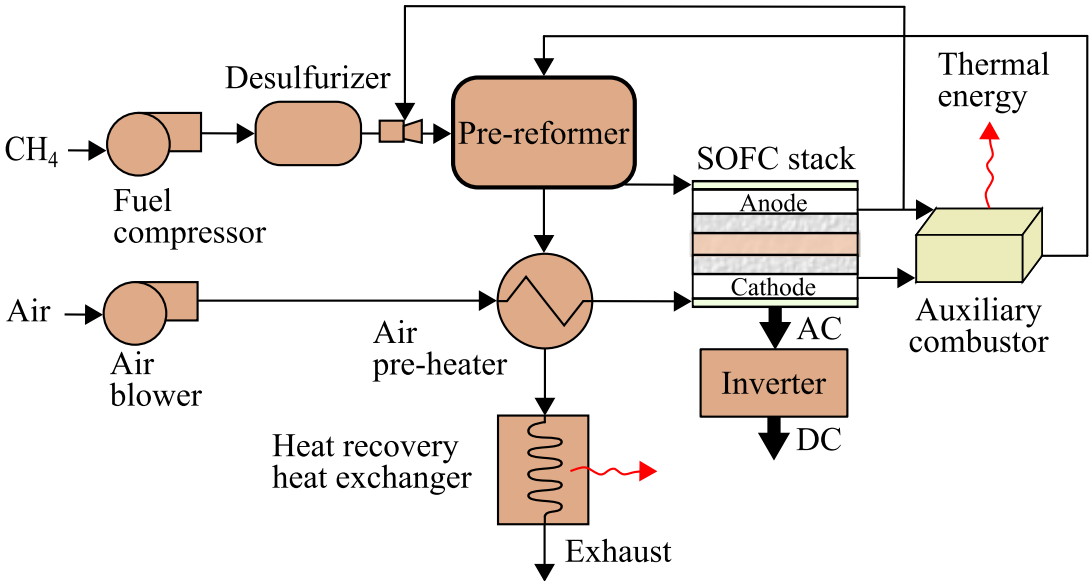


**Figure 5.9** Non-hybrid system schematic (adapted from [56]).

in the auxiliary combustor goes toward heating the combustion productions, but a small portion of the energy is lost to the environment. The combustor's exhaust drives the turbine, generating additional power, which is converted to 60 Hz AC. The system's exhaust pre-heats the incoming fuel and air streams, and the heat recovery heat exchanger recovers any remaining thermal energy.

### 5.3.2 Non-Hybrid System

The non-hybrid system consists of an SOFC stack as its sole power source. Figure 5.9 presents a schematic of the non-hybrid system. In the non-hybrid system, air enters the air blower, where it compressed to a pressure necessary to overcome the system's air-side pressure drop. The air is then pre-heated in the air pre-heater to a temperature suitable for SOFC operation. Meanwhile, fuel enters the fuel compressor, where it is compressed to a pressure necessary to overcome the system's fuel-side pressure drop. Similar to the hybrid system, the fuel is then desulfurized and pre-reformed. The reformate enters the fuel cell stack, generating power electrochemically. Unlike the hybrid system, the fuel cell stack operates at near-atmospheric

pressure. Again, part of the anode exhaust circulates back to the pre-reformer inlet in order to maintain an S/C ratio of 2. Unused fuel reacts in the auxiliary combustor, providing thermal energy to pre-heat the fuel and air. The heat recovery heat exchanger recovers any remaining thermal energy.

## 5.4 BASELOAD DEMAND

The hybrid and non-hybrid systems are sized to meet the baseload power demand of the University of Pittsburgh's Mascaro Center for Sustainable Innovation (MCSI). MCSI is a recent addition to the University of Pittsburgh's Benedum Hall engineering building. Figure 5.10 presents MCSI's average hourly load data during several different time periods throughout the year (collected from September 1, 2012 through September 1, 2013). The data represents major times during the school and calendar years. Fig. 5.10a presents the data for a typical (week-averaged) summer day during the semester, Fig. 5.10b presents the data for a typical (week-averaged) summer day during break, Fig. 5.10c presents the data for a typical (week-averaged) winter day during the semester, and Fig. 5.10d presents the data for a typical (week-averaged) winter day during break. The electric loads include plug loads, lights, fans for the air-handling units, and miscellaneous equipment. The thermal energy loads include the hot water used by the radiators and air-handling units. The steam demand (not shown here) contributes to the building's thermal load, particularly during the warmer months. Steam production, however, requires higher quality thermal energy than either system can produce. Thus, only the hot water demand is considered [149].

Figure 5.10 exhibits several notable features. First, the building exhibits a constant (baseload) power demand of approximately 65 $kW_e$ (amidst dynamic loads), regardless of the time of day, week, school year, or season. Thus, the system models developed herein are sized to meet the building's baseload power demand, generating a constant 65 $kW_e$. Second, the building's hot water demand varies significantly throughout the year. The hot water demand ranges from 89 $kW_{th}$ (during the summer break, as shown in Fig. 5.10b) to 302 $kW_{th}$ (during the winter break, as shown in Fig. 5.10d). Ideally, the systems will produce

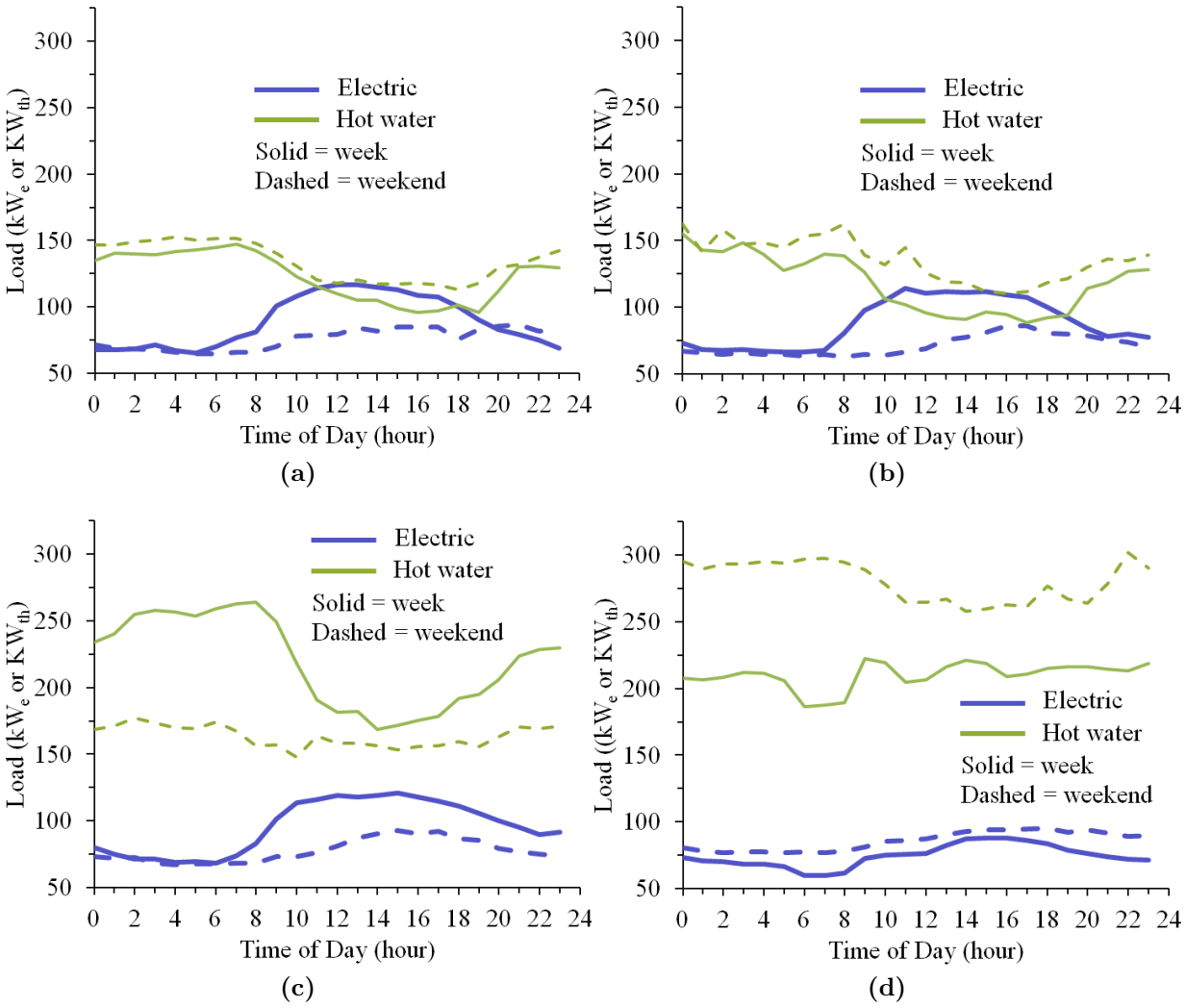


**Figure 5.10** A university building's electric and thermal loads during different time periods throughout the year (data obtained from Ref. [149]): (a) Summer day during the semester, (b) Summer day during break, (c) Winter day during the semester, (d) Winter day during break.

thermal energy as close to the minimum demand as possible. Thermal energy exceeding the minimum annual demand may be wasted if thermal energy storage is unavailable, and thermal energy less than the minimum demand leaves room for improvement. Third, the electric and hot water loads exhibit significant variation over the course of a day. A ramp-up in power demand (ramp-down in hot water demand) occurs during morning hours for

both weekdays and weekends, followed by a plateau during mid-day, and an eventual ramp-down (ramp-up in hot water demand) during the afternoons and evenings. Although system dynamics fall outside of the present work's scope, it bears mentioning that the power grid (or an additional prime mover) would likely be required to meet such loads. Fuel cells are generally not capable of meeting such fast transients on their own. A fuel cell stack may take minutes or hours to ramp up or ramp down due to thermal effects, as demonstrated in Chapter 4. Hence, an actual system may be larger and more complex than those considered herein.

## 5.5 COST MODEL

The cost model calculates the hybrid and non-hybrid systems' levelized costs of electricity (LCOE). The LCOE is defined as a system's life cycle cost per unit net power generated, accounting for the time value of money. The LCOE includes capital, maintenance, and fuel costs. The LCOE herein does not, however, include utility costs, such as the cost to import electricity from the power grid or operate a supplemental boiler. These costs come into play when considering the life cycle cost of the fuel cell system and utility combined. (Duffie and Beckman's $P_1, P_2$ method is particularly well-suited for calculating the life cycle cost of the fuel cell system and utility combined [97, 150].) Each system generates constant (baseload) power, and no consideration is given to loads exceeding the baseload demand. Thus, utility power is not considered. The following sections describe the cost model in more detail. The cost model results are presented in Chapter 8.

### 5.5.1 Levelized Cost of Electricity

The LCOE ($/kWh) depends on capital costs and system performance. The system's capital cost determines the system's initial expense (and associated replacement costs), and the system's electric efficiency and overall (CHP) efficiency determine the system's fuel costs.

The following LCOE formula is based on that presented by Braun [97] for CHP systems, who adapted the formula from Ellis and Gunes [151]:

$$\text{LCOE} = \frac{R_\text{F} C_\text{sys}}{CF_\text{e} A_\text{plant} \cdot 8,760 \text{ h/yr}} + \sum_i MC_i + \frac{F_\text{c}}{\eta_\text{sys,e}} - \frac{F_c \left(\eta_\text{CHP} - \eta_\text{sys,e}\right)}{\eta_\text{sys,e} \eta_\text{htg}} \cdot CF_\text{h} \tag{5.31}$$

where $R_\text{F}$ is the capital recovery factor, $C_\text{sys}$ is the system's total capital cost (\$/kW), $CF_\text{e}$ is the electric capacity factor, $A_\text{plant}$ is the plant's availability, $MC_i$ is the maintenance cost of component $i$ (\$/kWh), $F_\text{c}$ is the fuel cost (\$/kWh), $\eta_\text{sys,e}$ is the system's electric efficiency, $\eta_\text{CHP}$ is the system's overall efficiency, $\eta_\text{htg}$ is the conventional heating system's efficiency, and $CF_\text{h}$ is the heating capacity factor. Each term on the right-hand side of Eqn. (5.31) represents a cost category. The first term represents the system's capital cost. The system's capital cost equals the sum of its component costs. Also, the system's capital cost is normalized by 8,760 hours per year because the system is assumed to generate constant (baseload) power. The second term represents the maintenance cost. The maintenance cost consists of the component replacement costs over the course of the system's life, which will be discussed in more detail below. The third term represents the fuel cost associated with generating electricity. The fuel is assumed to be natural gas. The fourth term represents the fuel savings due to cogeneration. The fourth term represents a credit, which is the fuel savings resulting from the avoided use of the conventional heating system. The conventional heating system is assumed to be a natural gas boiler operating at 80% (HHV) efficiency [3].

The maintenance cost represents the periodic replacement of certain system components. Specifically, the maintenance cost accounts for the replacement of the SOFC stack, steam reformer catalysts, and the desulfurizer sorbent (ZnO), as well as the years in which these components are replaced. The maintenance cost does not include inspection, cleaning, or smaller component replacement costs. The maintenance cost associated with replacing component $i$ in years $N_1, N_2$, etc. is given by the following formula:

$$MC_i = \frac{R_\text{F} C_i \left[\frac{(1+i_\text{equip})^{N_1}}{(1+d)^{N_1}} + \frac{(1+i_\text{equip})^{N_2}}{(1+d)^{N_2}} + \cdots\right]}{CF_\text{e} A_\text{plant} \cdot 8{,}760 \text{ h/yr}} \tag{5.32}$$

where $C_i$ is the capital cost of component $i$, $i_\text{equip}$ is the equipment inflation rate, and $d$ is the discount rate [97]. The fuel cell stack is replaced every five years, as is the steam reformer

catalyst [5, 97, 152]. The desulfizer's sorbent, on the other hand, is assumed to be replaced every year [97, 153]. Notice that the maintenance cost in Eqn. (5.33) is normalized by 8,760 per year, similar to the capital cost in Eqn. (5.31), reflecting the system's constant power generation throughout the year. Furthermore, the discount rate is assumed to be $d = 10\%$, and the equipment inflation rate is assumed to be $i_{\text{equip}} = 2.8\%$ (based on the average annual change in the Chemical Engineering Plant Cost Index from 2004 to 2014 [154]). The capital recovery factor, $R_{\text{F}}$, annualizes each component's replacement cost, converting its present value to an equivalent annual (uniform) value. The capital recovery factor is given by the following formula:

$$R_{\text{F}} = \frac{d(1+d)^N}{(1+d)^N - 1} \tag{5.33}$$

where $N$ is the system's lifetime (in years) [155].

### 5.5.2 Capital Cost Estimation

Perhaps the most arduous (yet least certain) part of performing a cost analysis is estimating the system's capital cost. The system's capital cost equals the sum of its component costs:

$$C_{\text{sys}} = \sum_i C_i \tag{5.34}$$

Each component's capital cost depends on numerous factors, including the system's operation and the year(s) in which the cost data is provided. The present study adopts a bottom-up approach to estimating the system's capital cost, approximating each component based on previous estimates, and scaling these estimates as appropriate. The component costs are calculated according to the following formula:

$$C_i = C_{i,0} \left( \frac{S_i}{S_{i,0}} \right)^n \frac{CEPCI}{CEPCI_0} \tag{5.35}$$

where $C_{i,0}$ is the reference cost of component $i$, $S_i$ is the capacity of component $i$, $S_{i,0}$ is the reference capacity of component $i$, $n$ is the capacity scaling exponent, $CEPCI$ is the Chemical Engineering Plant Cost Index, and $CEPCI_0$ is the reference Chemical Engineering Plant Cost Index [155].[1] Each component's reference capacity depends on the system's design point,

[1] If the reference cost, $C_{i,0}$, is not already expressed in \$/kW (see Table 5.2), then the right-hand side of Eqn. (5.35) is divided by the net power generated to yield units of \$/kW.

whereas the scaling exponent is taken from previous studies for each device. The Chemical Engineering Plant Cost Index ensures that all costs are expressed in 2014 USD [154]. It should be noted that the above equation does not explicitly account for economies of production. Previous studies have investigated the influence of higher production volumes on fuel cell manufacturing costs [97, 144, 156]. In the present study, however, the production volume is assumed to remain fixed. Table 5.2 presents the cost parameters for a 250 kW, non-hybrid system. The estimated capital cost uncertainty is ±30% [157].

The cost parameters presented in Table 5.2 come from various studies. The National Energy Technology Laboratory (NETL) provides a fuel cell cost of $\$540/m^2$ in 2007 USD [158]. This cost is based on the U.S. Department of Energy's 2010 cost goal. The Pacific Northwest National Laboratory's (PNNL's) analysis of a 270 kW hybrid system provides cost estimates for the stack enclosure, fuel compressor, desulfurizer, and inverter [156]. These cost estimates are scaled appropriately for use in the present study. TIAX conducted a study in 2002 on 250 kW SOFC systems [159]. TIAX provides cost estimates for the air blower and filter, pre-reformer, and air pre-heater. Battelle conducted a study in 2014 on 1 kW and 5 kW SOFC auxiliary power units [153]. Battelle provides cost data for the combustor and additional components. The U.S. Environmental Protection Agency (EPA) characterized various combined heat and power systems [5]. The EPA provides cost estimates for the microturbine and heat recovery equipment. In addition, the scaling exponents in Table 5.2 come predominantly from Braun's techno-economic analysis of residential-scale SOFC systems [96, 97]. Braun obtained these scaling exponents by curve fitting cost data. The cost model results are presented in Chapter 8.

## 5.6 SUMMARY

The hybrid and non-hybrid systems generate constant power to meet a university building's baseload power demand, and the systems also cogenerate thermal energy. The building's dynamic loads, however, will likely require supplemental power and thermal energy, which is beyond the present work's scope. The BoP components account for changes in the fluid's

**Table 5.2** Cost parameters used to estimate the components' costs. All costs correspond to a 250 kW, non-hybrid system.[a]

| System component | Reference capacity ($S_{i,0}$) | Reference cost ($C_{i,0}$) | | Scaling exponent ($n$) | |
|---|---|---|---|---|---|
| Fuel cell stack | Area = 331.85 m$^2$ | \$196,494 | [158] | 1.00 | |
| Stack enclosure | $p_{\text{stack,inlet}} = 1.21$ atm | \$147 | [156] | 0.33 | [92] |
| Air blower | $\dot{W}_{\text{blow}} = 25.52$ kW | \$9,283 | [159] | 0.81 | [96, 97] |
| Air filter | $\dot{W}_{\text{blow}} = 25.52$ kW | \$589 | [159] | 0.81 | [96, 97] |
| Fuel compressor | $\dot{W}_{\text{comp,fuel}} = 0.64$ kW | \$1,987 | [156] | 0.67 | [96] |
| Desulfurizer | $\dot{m}_{\text{desulf}} = 36.56$ kg/h | \$2,432 | [156] | 0.67 | [96, 97] |
| Pre-reformer | $\dot{m}_{\text{reform}} = 302.85$ kg/h | \$54,900 | [159] | 0.67 | [96, 97] |
| Ejector | $\dot{m}_{\text{ejector}} = 302.85$ kg/h | \$241 | [145] | 0.67 | [96, 97] |
| Air pre-heater | $UA_{\text{air}} = 2.61$ kW/K | \$87,264 | [159] | 0.67 | [96] |
| Heat recovery[b] | - | \$13,500 | [5] | - | |
| Inverter | $\dot{W}_{\text{net}} = 250$ kW | \$149/kW | [156] | −0.22 | [96, 97] |
| Auxiliary combustor | $\dot{m}_{\text{comb}} = 2{,}985.61$ kg/h | \$10,286 | [153] | 0.82 | [97] |
| Microturbine[c] | $\dot{W}_{\text{MT}} = 30$ kW | \$53,100 | [5] | 0.80 | [5] |
| Additional components[d] | $\dot{W}_{\text{net}} = 250$ kW | \$24/kW | [153] | -0.83 | [97] |
| Labor and equipment[e] | - | $0.02 \times C_{\text{plant}}$ | [156] | - | |
| Installation[e] | - | $0.61 \times C_{\text{plant}}$ | [156] | - | |

[a] All costs are provided in 2014 USD.
[b] The heat recovery heat exchanger cost is assumed to remain fixed.
[c] The microturbine cost is based on a 30 kW Capstone system (instead of a 250 kW system). The microturbine cost includes the turbine, air compressor, combustor, and recuperator in a single package.
[d] The additional components include electronics and controls, instrumentation, and assembly components [153].
[e] $C_{\text{plant}}$ represents the plant's capital cost, which equals the sum of the prime mover and BoP costs.

composition and temperature as the species interact chemically and thermally throughout the system. In the hybrid system, the stack operates under pressure, and the stack's exhaust drives the microturbine. In the non-hybrid system, the stack's exhaust serves only to pre-heat the incoming fuel and air before passing through the heat recovery heat exchanger and exiting the system. The cost model accounts for the systems' capital, operating, and maintenance costs. The component costs come from previous studies, and the fuel costs come from the models developed herein. The next chapter investigates the fuel cell stack's dynamic response to load changes. Later chapters investigate the systems' performance.

# 6.0 RESPONSE TO CONTROL VARIABLES

The fuel cell model stack developed herein allows for dynamic simulations on multiple timescales. Processes within solid oxide fuel cells (SOFCs) are tightly coupled. Effective controllers minimize conflicts between control variables, thereby maintaining safe and efficient operation of the system. The present chapter simulates the open-loop response of the SOFC stack model to step load changes. The objective is to identify pairs of control variables that minimize interdependence, where interdependence may be defined as the inability of a manipulated variable to effectively control a targeted variables, unless control of another variable(s) is implemented. The reason for minimizing interdependence is to reduce the risk of oscillations between control loops. Consideration is also given to the time required for the stack to respond to load changes, as a faster response is desired to enhance load-following.

## 6.1 CASCADE CONTROL

Cascade control presents both benefits and challenges. Martinez, et al. [23] proposed the use of a cascade controller to operate a hybrid system safely and efficiently. Figure 6.1 presents a cascade controller's basic operation. A major benefit of such a controller is the minimization of interference between control loops, as lower levels are not pursued until the higher (safety-oriented) levels have been satisfied. At the highest level of priority (level 1 in Fig. 6.1), the controller satisfies safety requirements. The controller ensures that the average fuel cell temperature, for instance, remains within acceptable bounds. At lower levels of priority, the controller performs functions related to the system's performance. The controller ensures that the fuel utilization, for instance, remains within acceptable bounds. By stepping through

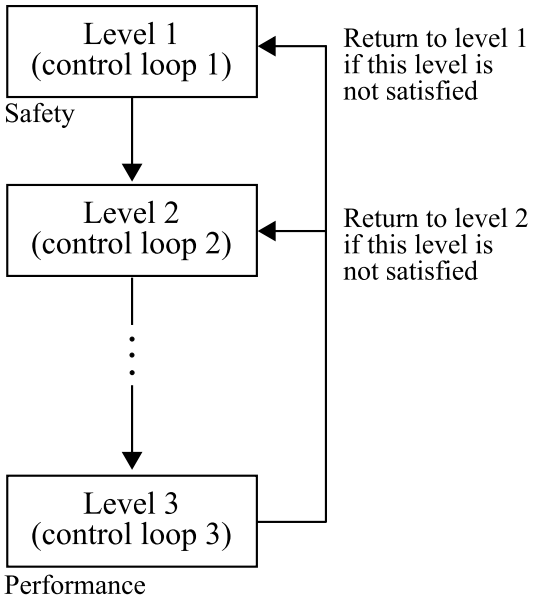


**Figure 6.1** Basic operation of a cascade controller for a hybrid system (adapted from [23]).

the control levels sequentially, such a control scheme avoids interference between the different control loops. A major challenge, however, is avoiding oscillations between the various levels, as changes in one level could provoke changes in another level due to the coupled nature of physical processes inside SOFCs, particularly if the processes occur on similar timescales. As the lower levels are pursued, the higher level control variables may fall outside their bounds, causing the controller to return to these higher levels and potentially oscillate back and forth between control levels.

The present work identifies pairs of control variables that minimize interdependence, where interdependence may be defined as the inability of a manipulated variable to effectively control a targeted variable, unless control of another variable(s) is implemented. The reason for minimizing interdependence is to reduce the risk of oscillations between control levels in a cascade controller. To do so, the present chapter simulates the stack's dynamic response to step changes in manipulated variables on different timescales. In particular, the uncontrolled (open-loop) response of the average PEN temperature, fuel utilization, and SOFC power is simulated in response to step changes in the inlet fuel flow rate, current density (or voltage), and inlet air flow rate. The former set of variables typically requires control in an SOFC-gas

turbine (GT) system for safety and efficiency reasons, while the latter variables are often manipulated to achieve control, as manipulation of these variables is feasible and can also induce significant changes in the controlled variables [22,23,57–59].[1] During each simulation, only one variable (inlet fuel flow rate, current density, or inlet air flow rate) is altered to observe the particular influence that each manipulated variable has on SOFC stack behavior. A step change in the manipulated variable is imposed after 50 time steps; the precise time at which the step change is imposed is thus not significant. Due to the fuel cell's varying response on different timescales, each simulation has been performed on millisecond, second, and minute timescales.

## 6.2 DYNAMIC RESPONSE

### 6.2.1 Operating Conditions

Table 6.1 presents the SOFC stack's operating conditions. The operating conditions reflect typical SOFC-GT operating conditions found in the literature. Even though the balance-of-plant components are not modeled in this chapter, system context has been considered here. The SOFC operates at a pressure ratio of 4:1 [18,21], and the stack is sized to meet a power demand of approximately 100 kW (assuming a typical power output of approximately 20 W per fuel cell). The power rating of 100 kW is similar to that of a small microturbine [55]. In the dynamic response simulations, consideration has been given to the SOFC operating conditions presented in the 1996 IEA benchmark study discussed in Chapter 4 [142], particularly the inlet gas temperature, fuel composition, and mean current density. Because the balance-of-plant components are not considered in this chapter, the operating parameters in Table 6.1 are assumed to remain constant, unless otherwise specified. Lastly, it should be mentioned that "definition 2" of the fuel utilization is considered in this chapter:

$$U_{\mathrm{f},2} = 1 - \frac{4\dot{n}_{\mathrm{CH_4,exit}} + \dot{n}_{\mathrm{H_2,exit}} + \dot{n}_{\mathrm{CO,exit}}}{4\dot{n}_{\mathrm{CH_4,inlet}} + \dot{n}_{\mathrm{H_2,inlet}} + \dot{n}_{\mathrm{CO,inlet}}} \qquad \text{(3.38 revisited)}$$

This definition accounts for mass storage inside the fuel cell.

[1] It should be noted that microturbines (MTs) form a subcategory of gas turbines (GTs).

**Table 6.1** Fuel cell's operating conditions during dynamic response simulations.

| Parameter | Value |
|---|---|
| Flow configuration | Co-flow |
| Inlet gas pressure | 4 bar |
| Inlet gas temperature | 1173 K |
| Extent of pre-reforming | 30% |
| Steam-to-carbon ratio | 2.5 |
| Inlet air composition | $O_2 = 21\%$ |
| | $N_2 = 79\%$ |
| Inlet fuel flow rate[a] | $2.978 \times 10^{-6}$ kg/s |
| Inlet air flow rate[a] | $8.874 \times 10^{-5}$ kg/s |
| Mean current density[a] | 3000 A/m$^2$ |
| Number of cells | 5000 |

[a] Input variable that may vary.

### 6.2.2 Fuel Flow Rate Step Change

The SOFC stack's dynamic response to a step change in the inlet fuel flow rate is shown in Fig. 6.2. During this simulation, the fuel flow increases by 50% (from an initial value of $2.978 \times 10^{-6}$ kg/s, as indicated in Table 6.1) at times 50 ms, 5 s, and 50 min (Figs. 6.2a, 6.2b, and 6.2c, respectively). On the millisecond timescale (Fig. 6.2a), it can be seen that a small increase in the fuel utilization occurs before the exit fuel flow rate has time to respond, followed by a gradual decline in the fuel utilization. This gradual decline likely demarcates the beginning of the mass flow response. Meanwhile, the SOFC power and PEN temperature remain relatively constant. On the second timescale (Fig. 6.2b), the fuel utilization changes significantly, decreasing from 85% to slightly over 55% in a few seconds time. This settling time is indicative of mass flow transient behavior. The power undergoes a slight increase as well, which is due to the increasing operating voltage on the second timescale. Lastly, on the minute timescale (Fig. 6.2c), the PEN temperature decreases slightly, which is likely due to the increased convection between the PEN structure and fuel when the fuel flow rate increases. This slight change in the PEN temperature corresponds to a similarly small decrease in the power.

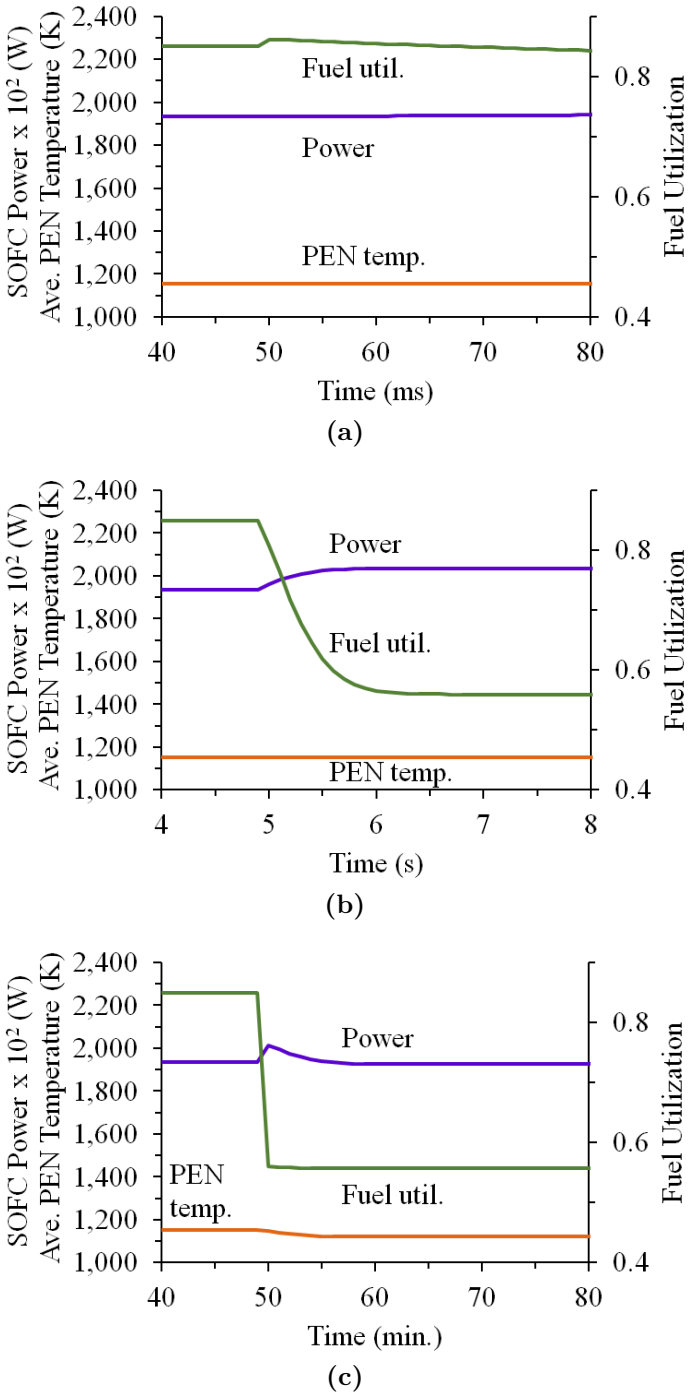


**Figure 6.2** SOFC stack's response to a step change in the inlet fuel flow rate: (a) Millisecond timescale, (b) Second timescale, (c) Minute timescale.

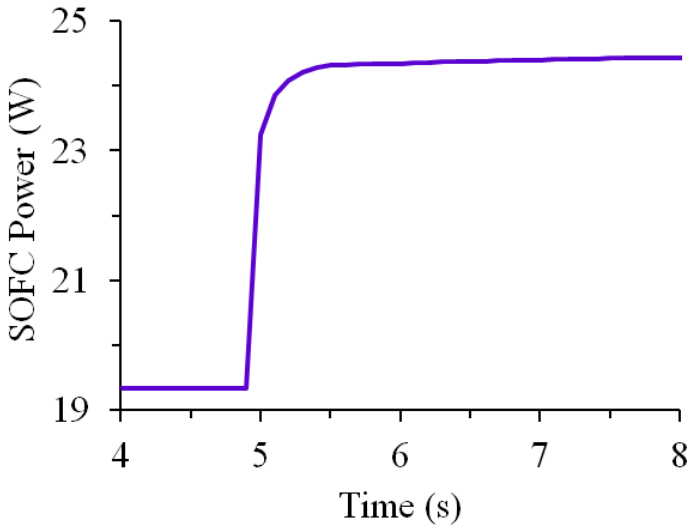


**Figure 6.3** SOFC stack's response to a step change in the inlet fuel flow rate assuming constant fuel utilization ($U_{\mathrm{f},2} = 85\%$).

Interestingly, the influence of the inlet fuel flow rate on the SOFC power when assuming constant fuel utilization differs drastically from that when the fuel utilization is allowed to vary freely. In particular, under constant fuel utilization (i.e., ideal control of the fuel utilization), changing the fuel flow rate changes the power significantly. Figure 6.3 displays the SOFC stack's response to the same change in the inlet fuel flow rate as considered previously, except the fuel utilization is held fixed at $U_{\mathrm{f},2} = 85\%$. As can be seen in Fig. 6.3, the power exhibits an increase of over 5 W on the second timescale. This result differs drastically from that obtained when the fuel utilization is allowed to vary freely, during which the power increases by only 1 W (Fig. 6.2b). The reason for this difference is rooted in the definition of the fuel utilization, which is given in Eqn. (3.38). The fuel utilization may be qualitatively defined as the ratio of the mass consumed over the mass acquired. If this ratio is held constant and the inlet fuel flow rate increases, then the mass consumed (or current) also increases, leading to a significant increase in the power.

### 6.2.3 Current Density Step Change

The average current density is manipulated to observe its influence on the SOFC stack's behavior. Figure 6.4 illustrates the stack's dynamic response to a step change in the average current density. The current density is decreased by 50% (from an initial value of 3000 $A/m^2$) at times 50 ms, 5 sec., and 50 min. (Figs. 6.4a, 6.4b, and 6.4c, respectively). On the millisecond timescale (Fig. 6.4a), the power responds instantaneously to the change in the current density, decreasing sharply from 19 W to 11 W. The fuel utilization, on the other hand, decreases gradually, which is likely the beginning of the mass flow response. Meanwhile, the PEN temperature remains relatively constant. On the second timescale (Fig. 6.4b), the fuel utilization responds at a rate similar to that previously seen when manipulating the fuel flow rate (Fig. 6.2b), decreasing from 85% to 44% within seconds. Again, the mass flow dynamic behavior appears to be at work here. Observe, also, from Fig. 6.2b that the power increases slightly on the second timescale, which is due to the increasing operating voltage on the second timescale. On the minute timescale (Fig. 6.4c), the PEN temperature decreases slightly. Lower power generation (and hence lower thermal energy generation) likely explains this behavior.

### 6.2.4 Air Flow Rate Step Change

Finally, it can seen from Fig. 6.5 that a step change in the inlet air flow rate (50% increase) negligibly influences all of the SOFC variables shown, under the assumed operating conditions. This result is not surprising, however, as the inlet air temperature is specified to be 1173 K (Table 6.1), and the PEN temperature is already near this value at the outset of the simulation (1153 K, initially). Changing the air flow thus negligibly influences the PEN temperature under the present operating conditions. During a transient event that induces more severe PEN temperature changes, however, changing the air flow would likely be useful for returning the PEN temperature back to its reference value.

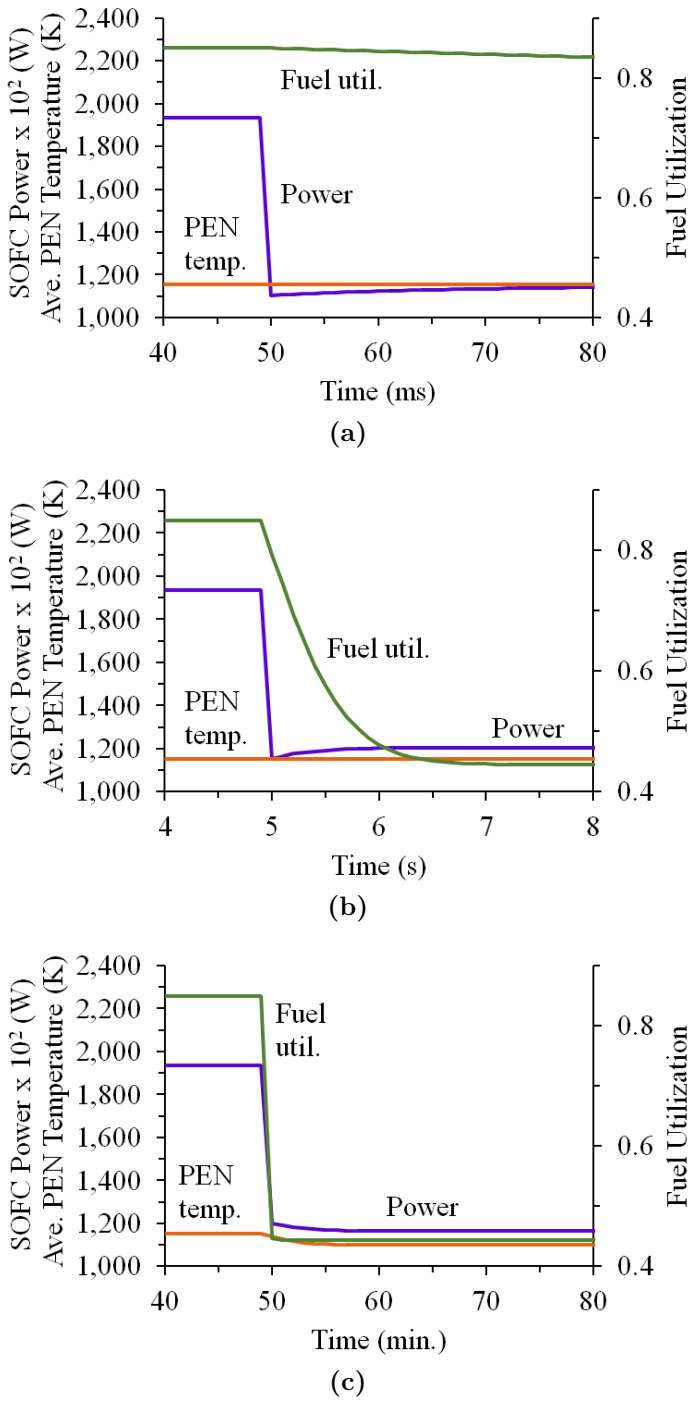


**Figure 6.4** SOFC stack's response to a step change in the current density: (a) Millisecond timescale, (b) Second timescale, (c) Minute timescale.

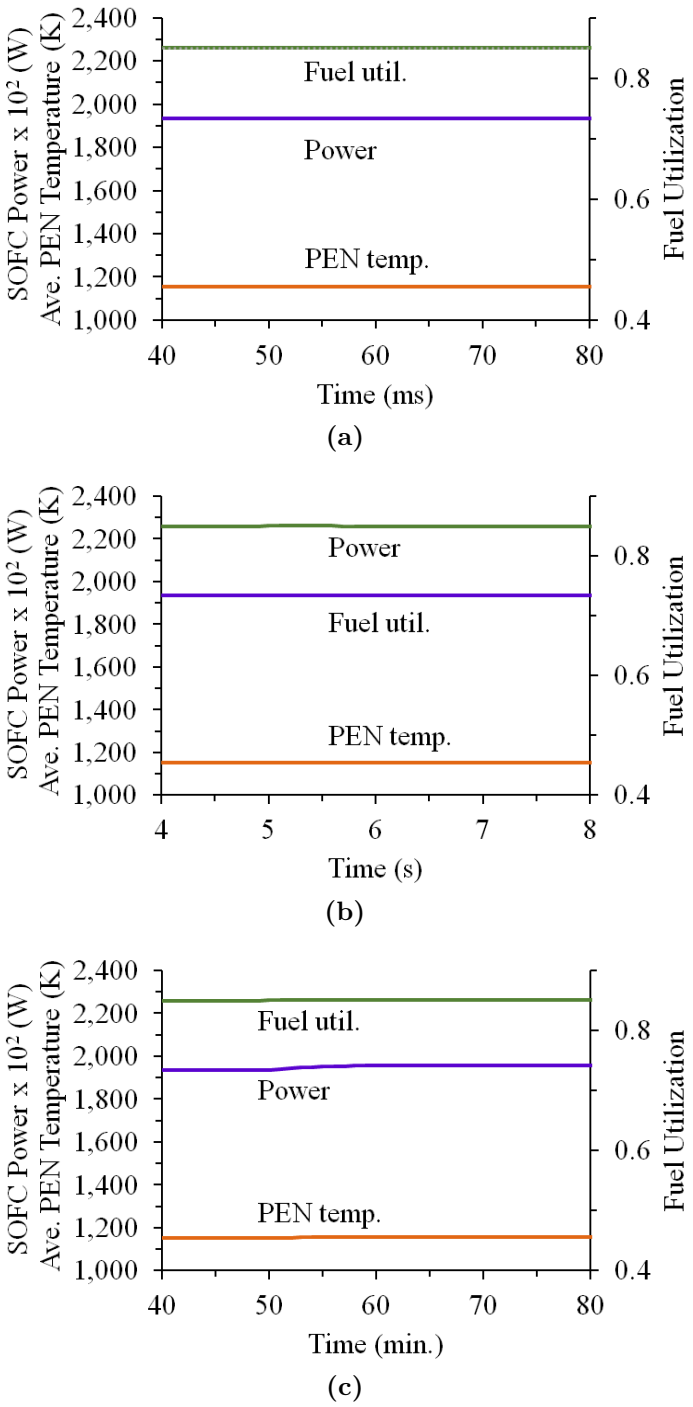


**Figure 6.5** SOFC stack's response to a step change in the inlet air flow rate: (a) Millisecond timescale, (b) Second timescale, (c) Minute timescale.

**Table 6.2** Comparison of control strategies.

| Strategy | Description | Characteristics |
|---|---|---|
| 1 | Inlet fuel flow rate controls power<br>Current density controls fuel utilization | High interdependence<br>Slow power response |
| 2 | Current density controls power<br>Inlet fuel flow rate controls fuel utilization | Low interdependence<br>Fast power response |

## 6.3 COMPARISON OF CONTROL STRATEGIES

Based on the previous results, two control strategies emerge as feasible for operating the SOFC stack. Table 6.2 summarizes these control strategies. While both of these strategies have been considered before at the system level [22, 23, 57, 58], the present work considers these strategies at the stack level. The first strategy involves manipulating the fuel flow to control the power, while manipulating the current density to control the fuel utilization. The second strategy is the reverse of the first—it involves manipulating the current density to control the power, while manipulating the fuel flow rate to control the fuel utilization. Control of the fuel utilization may be achieved by manipulating either the fuel flow rate or the current density because changing either of these variables induces significant changes in the fuel utilization (Figs. 6.2b and 6.4b, respectively). Likewise, control of the power may be achieved by manipulating either the fuel flow rate or the current density because changes in both of these variables induce significant changes in the power (Figs. 6.3 and 6.4a, respectively). In either strategy, the air flow would serve to control SOFC temperature, as the air flow was found to negligibly influence the fuel utilization and power while still having the potential to control the PEN temperature during a transient event.

A major difference between these control strategies is their interdependent quality. As mentioned previously, interdependence may be defined as the inadequacy of a manipulated variable to effectively control a targeted variable, unless tight control of another variable(s) is assumed. Interdependence between pairs of control variables is undesired, as it could lead

to oscillations between control levels in a cascade controller. Importantly, the first strategy (manipulating the fuel flow rate to control the power, while manipulating the current density to control the fuel utilization) gives rise to strong interdependence. When the fuel utilization is maintained at 85%, in particular, Fig. 6.3 demonstrates that manipulating the fuel flow rate influences the power significantly. However, when the fuel utilization is allowed to vary freely, Fig. 6.2b demonstrates that manipulating the fuel flow rate hardly influences the power at all. Hence, controlling the power using the fuel flow rate is sensible only if tight control of the fuel utilization is implemented. In a cascade controller, such as that proposed by Martinez, et al. [23], such a control strategy may result in oscillations between the fuel utilization and power control levels, as these control loops would be highly interdependent.

The second control strategy, on the other hand, appears to minimize interdependence. If the current density controls the power, that is, then the power and fuel utilization operate fairly independently. In particular, it can be seen from Fig. 6.4a that manipulating the current density gives rise to significant changes in the SOFC power, without placing any restrictions on the fuel utilization. Likewise, Fig. 6.2b shows that manipulating the fuel flow rate gives rise to significant changes in the fuel utilization, without placing any restrictions on the current density. Because these control loops operate fairly independently, control need not jump back and forth between the power and fuel utilization levels to satisfy control criteria. Of course, restrictions may apply. Changing the current density too rapidly, for instance, may cause the fuel utilization to overshoot or undershoot its bounds (as shown in Fig. 6.4, the fuel utilization responds to the fuel flow in seconds, whereas the power responds nearly instantaneously to the current density). However, rate limitations could be incorporated into the control strategy at the system level [22].

Based on the considerations discussed previously, manipulating the current density is the most effective way to control the SOFC power, while manipulating the inlet fuel flow rate is the most effective way to control the fuel utilization. Relying on one variable (current density) to control power, rather than relying on two variables (current density while holding the fuel utilization fixed), simplifies the control logic. The time required for the SOFC stack to meet a power demand provides further motivation for adopting this strategy. If the current density controls the power, then the power responds instantaneously to a load change (Fig. 6.4a).

If the fuel flow rate controls the power, on the other hand, then the power responds slower to load changes (Fig. 6.3). Buildings experience significant load change over the course of a day [149, 160, 161], and meeting power demand quickly is important.

## 6.4 SUMMARY

This chapter investigated the response of key SOFC variables to step changes in the inlet fuel flow rate, current density, and inlet air flow rate. Manipulating the current density significantly changed the SOFC stack's power without placing any restrictions on the fuel utilization. Manipulating the inlet fuel flow rate, on the other hand, required tight control of the fuel utilization; otherwise, the inlet fuel flow rate exhibited little or no influence on the SOFC stack's power. Because the former strategy provides greater independence between control loops, it is recommended that this strategy be considered for use in a cascade controller. Consideration has also been given in this study to the time required for the SOFC to meet a power demand. The SOFC power responded quicker to changes in the current density (near-instantaneous) compared to changes in the inlet fuel flow rate (seconds), thus providing further motivation for adopting the former strategy. The next chapter continues to consider the SOFC stack's dynamic behavior, looking more closely at electrochemical dynamics.

# 7.0 CHARGE DOUBLE LAYER

The fuel cell stack model allows for dynamic simulations on the millisecond timescale. Importantly, if the charge double layer extends beyond the millisecond timescale, then it will likely influence the fuel cell stack's control logic (described in the previous chapter), potentially leading to undesired operation. Although the charge double layer effect has traditionally been characterized as a millisecond phenomenon, longer timescales may be possible under certain operating conditions. The present chapter identifies operating conditions that give rise to unusually long electrochemical settling times inside the SOFC stack. Baseline conditions are first defined, followed by consideration of minor and major deviations from the baseline case. The present work also investigates the behavior of the fuel cell stack with a relatively large double layer capacitance value, as well as operation of the SOFC stack under proportional-integral (PI) control. The fuel cell stack model is simulated under step load changes. It is found that high activation and concentration polarizations correspond to unusually long electrochemical settling times, as do large capacitance values. Thus, while neglecting the charge double layer simplifies the fuel cell model, it may also detract from the fuel cell model's accuracy under certain operating conditions.

## 7.1 CHARGE DOUBLE LAYER

The charge double layer is a (dual) layer of positive and negative charge that accumulates along the electrode-electrolyte interfaces, giving rise to a capacitor-like effect. Charge may accumulate due to electrochemical reactions or charge diffusion across the interfaces, or possibly another cause [26, 43]. An example of such a charge configuration is shown in

Fig. 7.1a, where the negative charges represent oxygen ions being transported from the cathode to the anode through the electrolyte. Clearly, the charge double layer resembles an electric capacitor. Similar to an electric capacitor, the charge double layer may be charged or discharged, depending on the direction of current, or load (Fig. 7.1b). As discussed in Chapter 3, the voltage drop across the charge double layer is treated as an irreversibility in the SOFC, similar to the ohmic polarization. That is, the double layer polarization is subtracted from the Nernst potential when calculating the fuel cell's operating voltage:

$$V_{\text{op}} = E_{\text{N}} - V_{\text{dbl}} - iR_{\text{ohm}} \qquad \text{(3.25 revisited)}$$

where $V_{\text{op}}$ is the fuel cell's operating voltage, $E_{\text{N}}$ is the Nernst potential, $V_{\text{dbl}}$ is the double layer polarization, $i$ is the electric current, and $R_{\text{ohm}}$ is the ohmic resistance. The present study is especially concerned with the time required for the charge double layer to settle following a load change. The time constant of the electrochemical model is given by [64]:

$$\tau_{\text{dbl}} = (R_{\text{act}} + R_{\text{conc}}) \times C_{\text{dbl}} \qquad (7.1)$$

where $\tau_{\text{dbl}}$ is the electrochemical time constant, $R_{\text{act}}$ is the activation resistance, $R_{\text{conc}}$ is the concentration resistance, and $C_{\text{dbl}}$ is the double layer capacitance. The activation and concentration resistances equal the ratio of the activation and concentration polarizations to the electric current. It is evident from Eqn. (7.1) that increasing $R_{\text{act}}$, $R_{\text{conc}}$, or $C_{\text{dbl}}$ slows the fuel cell's response to load changes. Section 7.2 further explores operating conditions that give rise to high values of $R_{\text{act}}$ and $R_{\text{conc}}$. A high value of the double layer capacitance is considered during dynamic simulations presented in Section 7.3.

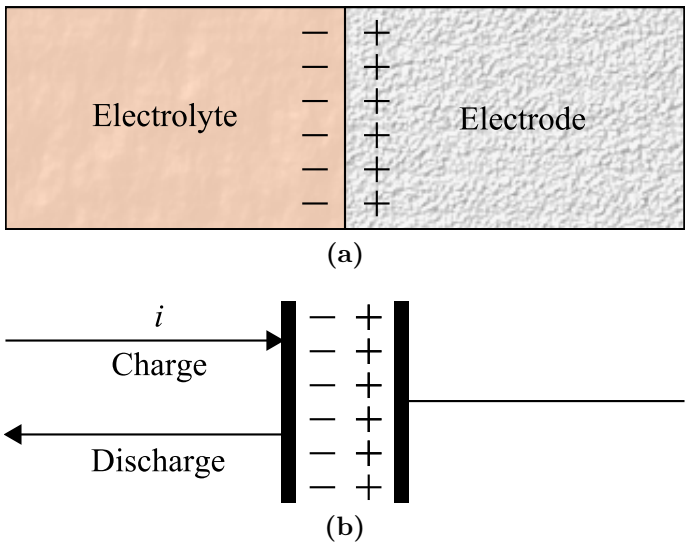


**Figure 7.1** The charge double layer (adapted from Ref. [43]): (a) Charge double layer, (b) Equivalent capacitor showing the charging and discharging of the charge double layer.

## 7.2 STEADY-STATE BEHAVIOR

This section identifies operating conditions that give rise to high values of the activation and concentration polarizations. Higher values of the activation and concentration polarizations correspond to higher values of the equivalent resistances, and higher equivalent resistances, in turn, give rise to longer electrochemical time constants. In this section, a baseline case is first defined, followed by investigation of off-design operation. The baseline case reflects typical SOFC operating conditions. The off-design conditions, on the other hand, reflect scenarios that give rise to higher values of the activation and concentration polarizations. Both minor and major deviations from the baseline case are considered.

### 7.2.1 Baseline Case

Table 7.1 presents the baseline operating conditions. These conditions reflect an SOFC's typical operation in a hybrid SOFC-gas turbine (GT) system.[1] Even though the balance-of-plant components are not modeled in this chapter, system context has been considered here.

[1]It should be noted that microturbines (MTs) form a subcategory of gas turbines (GTs).

**Table 7.1** Fuel cell stack's baseline operating conditions during charge double layer simulations.

| Parameter | Value |
|---|---|
| Flow configuration | Co-flow |
| Inlet gas pressure | 4 bar |
| Inlet gas temperature | 1173 K |
| Inlet fuel composition[a] | $CH_4 = 17.07\%$ |
| | $H_2 = 26.31\%$ |
| | $H_2O = 49.30\%$ |
| | $CO = 2.96\%$ |
| | $CO_2 = 4.36\%$ |
| Inlet air composition | $O_2 = 21\%$ |
| | $N_2 = 79\%$ |
| Inlet fuel flow rate (single cell) | $2.978 \times 10^{-6}$ kg/s |
| Inlet air flow rate (single cell) | $8.874 \times 10^{-5}$ kg/s |
| Mean current density | 3000 A/m$^2$ |
| Number of fuel cells | 5000 |

[a] The fuel composition is based on a 30% pre-reformed steam-methane mixture with a steam-to-carbon ratio of 2.5.

Thus, the SOFC is assumed to operate at a pressure ratio of 4:1 [18, 21], and the stack is sized to meet a power demand of approximately 100 kW (assuming a typical power output of approximately 20 W per fuel cell). The power rating of 100 kW is similar to that of a small microturbine [55]. Significant consideration has also been given to the design specifications and operating conditions presented in the 1996 IEA benchmark study discussed in Chapter 4 [142] (and accompanying report [127]), particularly those regarding cell geometry, material properties, inlet gas temperature, fuel composition, and mean current density. Because the balance-of-plant components are not considered in this chapter, the operating parameters presented in Table 7.1 are assumed to remain constant, unless otherwise specified.

**7.2.1.1 Minor Deviation** During normal operation of an SOFC-GT system, minor variations in the average PEN temperature and inlet fuel flow rate are to be expected. Martinez, et al. [23, 63] and Stiller, et al. [22] simulated the controlled, dynamic behavior of SOFC-GT systems intended for use in locomotives and stationary power applications, respectively. In

both studies, the systems exhibited variations in the average fuel cell temperature and inlet fuel flow rate during normal operation. In particular, the controllers manipulated the inlet air flow rate to control the average fuel cell temperature, and they manipulated the inlet fuel flow rate to control either the power or fuel utilization. Safe and efficient operation necessitates the use of such control, as too high a fuel utilization could lead to deleterious redox cycling of the anode [162–164], and too low a temperature could significantly increase the electrolyte's ohmic resistance [43], thereby reducing the SOFC's operating voltage. Therefore, variations in the average PEN temperature and inlet fuel flow rate are to be expected.

Figure 7.2a presents the axially averaged activation and concentration polarizations in the present model as the inlet gas temperature varies between 1173 K (baseline conditions) and 1073 K (the lower bound of the high-temperature regime [73]). The black dots in Fig. 7.2a indicate the values associated with the baseline case. Evidently, as the inlet gas temperature is lowered, the activation polarization increases significantly. This result likely stems from the exchange current density's temperature dependence, as lowering the average PEN temperature typically reduces the exchange current density [26, 43], thus increasing the activation polarization. The concentration polarization, on the other hand, decreases slightly with decreasing temperature because the concentration polarization is directly proportional to the average PEN temperature. It should also be noted that Fig. 7.2 scales the activation polarization by a factor of $10^2$ in order to fit the plot. Hence, the activation polarization dominates the concentration polarization by a large margin.

Figure 7.2b presents the axially averaged activation and concentration polarizations as the inlet fuel flow rate varies between $2.98 \times 10^{-6}$ kg/s (baseline) and $2.59 \times 10^{-6}$ kg/s (87% of baseline). Again, the black dots indicate the baseline values. Evidently, lowering the inlet fuel flow rate (i.e., increasing the fuel utilization) increases the concentration polarization significantly. This result likely stems from the relatively low reactant partial pressures at the triple-phase boundary resulting from the high fuel utilization. After all, SOFCs are known to exhibit higher concentration losses with increasing fuel utilization, particularly as they enter the high current density (concentration-loss dominated) regime [26, 68]. Figure 7.2b shows that the activation polarization, on the other hand, decreases slightly with a decreasing inlet fuel flow rate.

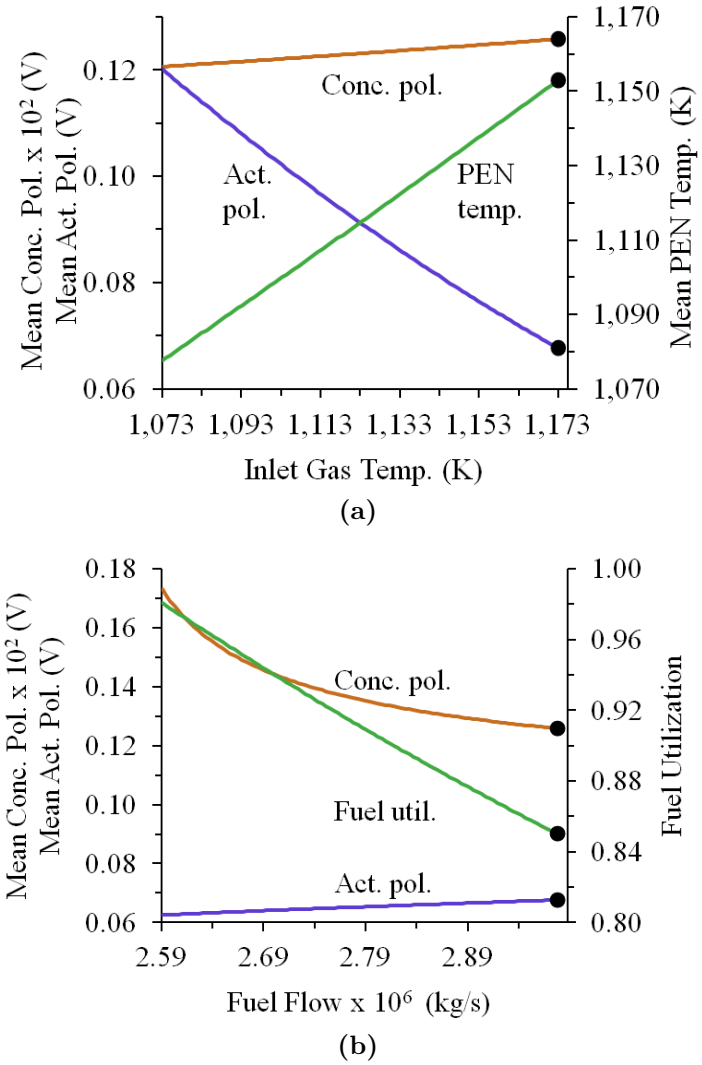


**Figure 7.2** Sensitivity of the axially averaged activation and concentration polarizations to minor deviations from baseline (the black dots indicate the baseline values): (a) Polarizations and the average PEN temperature as a function of the inlet gas temperature, (b) Polarizations and the fuel utilization as a function of the inlet fuel flow rate into a single cell.

**7.2.1.2 Major Deviation** In addition to considering minor deviations from the baseline case, the present study also investigates major deviations. It is supposed that such deviations may result from fuel cell degradation processes, such as redox cycling [162–164], thermal stress [165], or secondary phase formation [166–168]. Major deviations could conceivably also

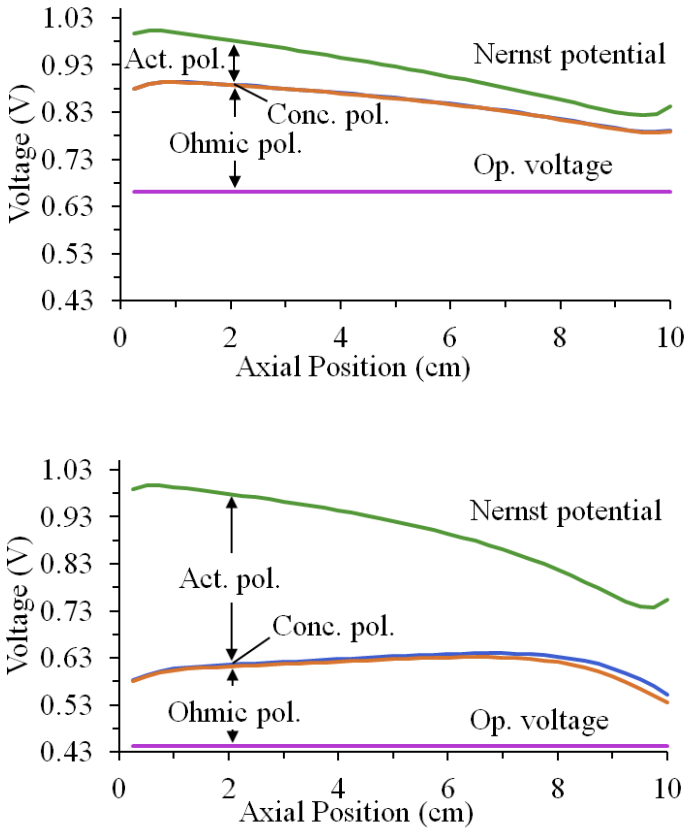


**Figure 7.3** Polarizations under major deviations from baseline: (a) Baseline operation, (b) Five-fold increase in activation and concentration polarizations.

result from equipment failure, such as sensor malfunction [22]. In the present work, severe changes in operation are modeled by simply assuming a five-fold increase in the activation and concentration polarizations. A factor of five has been chosen somewhat arbitrarily, representing a significant increase in the activation and concentration polarizations without causing the fuel cell to stall (i.e., reach zero voltage). After modifying the model to include a five-fold increase, the polarization distributions in Fig. 7.3b result. Figure 7.3a presents the baseline case for comparison. As expected, the operating voltage drops significantly with such a large increase in the activation and concentration polarizations, and the activation polarization remains much more prominent than the concentration polarization. Notice, also, that the shapes of the polarization distributions change slightly.

## 7.3 DYNAMIC RESPONSE

The present study investigates the SOFC stack's dynamic response to step changes in current density. In each simulation, the SOFC stack is initialized to one of the following aforementioned sets of conditions: (i) baseline, (ii) minor deviations from baseline, or (iii) major deviations from baseline. During each simulation, a step change of 500 A/m$^2$ is introduced after 50 time steps, and the operating fuel cell voltage is monitored. The double layer capacitance varies between $1 \times 10^{-9}$ mF and 10 mF in most simulations to investigate the charge double layer's influence on the SOFC stack's behavior. The small double layer capacitance value represents the case where virtually no charge double layer effect is present, while the larger value represents a more typical value [26, 64, 130].

### 7.3.1 Baseline Case

The dynamic response of the SOFC stack initialized to the baseline conditions (Table 7.1) is presented in Fig. 7.4. In Fig. 7.4a, the current density increases from 3000 A/m$^2$ to 3500 A/m$^2$ (step-wise) at 50 ms, while in Fig. 7.4b, the current density decreases from 3000 A/m$^2$ to 2500 A/m$^2$ (step-wise) at 50 ms. (It should be noted that the operating voltage is plotted for a single fuel cell, although the entire stack has been simulated). In both simulations, the settling time is found to be approximately 75–100 ms, where settling time is defined here as the time required for the charge double layer effect to diminish following a step change in current density (i.e., where the operating voltage at $C_{\text{dbl}} = 10$ mF meets the curve at $C_{\text{dbl}} = 1 \times 10^{-9}$ mF). A settling time of 75–100 ms is consistent with the traditional characterization of the charge double layer effect as a millisecond phenomenon [59, 68, 134].

Moreover, Fig. 7.4 shows that the double layer polarization follows the same trend as the fuel cell's operating voltage (in terms of time response) for a given capacitance value. That is, when the current density increases, the double layer polarization increases within milliseconds for $C_{\text{dbl}} = 10$ mF (meaning that the capacitor is charging), whereas the double layer polarization increases instantaneously for $C_{\text{dbl}} = 1 \times 10^{-9}$ mF (meaning that the charging time is negligible). Similarly, when the the current density decreases, the dou-

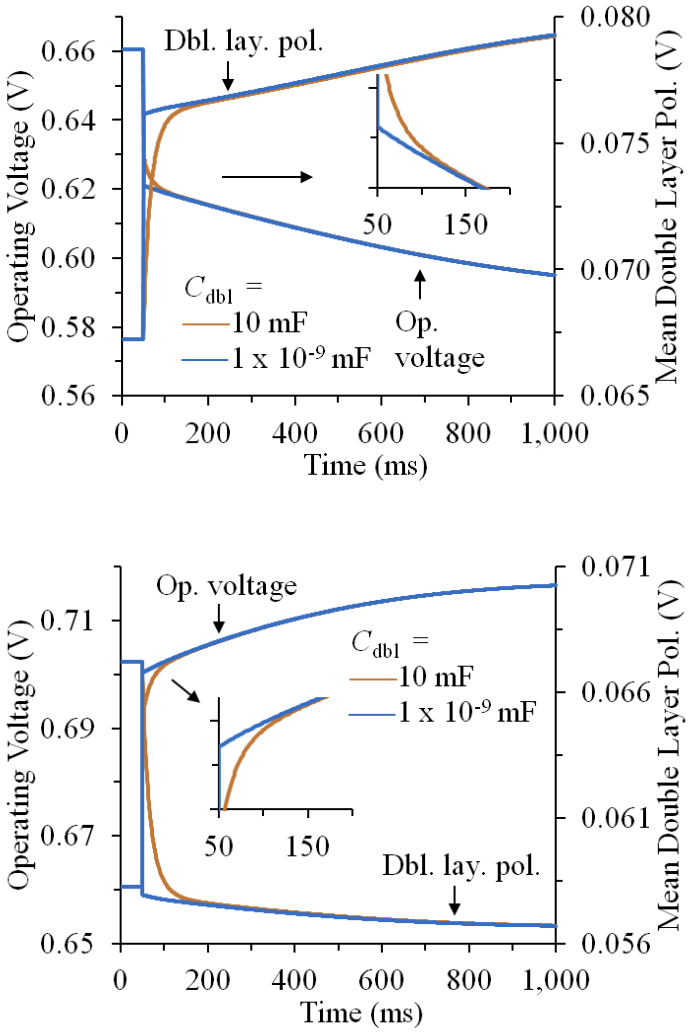


**Figure 7.4** Dynamic response of the SOFC stack initialized to baseline conditions: (a) Dynamic response to a step increase in current density, (b) Dynamic response to a step decrease in current density.

ble layer polarization decreases within milliseconds for $C_{\text{dbl}} = 10$ mF (meaning that the capacitor is discharging), whereas the double layer polarization decreases instantaneously for $C_{\text{dbl}} = 1 \times 10^{-9}$ mF (meaning that the discharging time is negligible). Notice, also, that slight differences exist between the precise settling times of the operating voltages and the double layer polarizations. These differences likely stem from the insensitivity of the ohmic-dominated operating voltage to the activation and concentration polarizations, mak-

ing changes in the operating voltage difficult to see. All settling times stated hereafter refer to the operating voltage (rather than the double layer polarization), as the operating voltage is directly measurable in an actual system.

### 7.3.2 Minor Deviation

Figure 7.5 presents the dynamic response of the SOFC stack initialized to operating conditions that deviate slightly from the baseline case. That is, at the simulation's outset, the inlet gas temperature is initialized to 1073 K (reduced by 100 K from the baseline value of 1173 K), and the inlet fuel flow rate is $2.59 \times 10^{-6}$ kg/s (87% of the baseline value). At 50 ms, a change in load is introduced by decreasing the current density from 3000 A/m$^2$ to 2500 A/m$^2$ (step-wise). It is found that the charge double layer effect diminishes, again, within milliseconds, where the precise settling time is found to be approximately 150 ms. Importantly, this settling time comes very close to that obtained previously under baseline conditions (75–100 ms). Thus, minor deviations from baseline appear to minimally influence the SOFC stack's electrochemical setting time. In addition, Fig. 7.4 shows that, again, the fuel cell's operating voltage follows the same trend (in terms of time response) as the double layer polarization, with slight differences as explained before. Also, as before, the charge double layer polarization continues to vary even after settling has occurred, which likely demarcates the beginning of the mass flow dynamic response. As a final note, it was found that increasing the current density from 3000 A/m$^2$ to 3500 A/m$^2$ caused the model's equations to become constrained, and thus, a solution could not be obtained. This error likely stems from the excessively high fuel utilization that results from increasing the current density while holding the inlet fuel flow rate fixed.

### 7.3.3 Major Deviation

Figure 7.6 presents the dynamic response of the SOFC stack initialized to operating conditions that deviate significantly from the baseline case. That is, a five-fold increase in the activation and concentration polarizations has been imposed, as discussed in Section 7.2.1.2. In Fig. 7.6a, the current density increases from 3000 A/m$^2$ to 3500 A/m$^2$ (step-wise) at 50 ms,

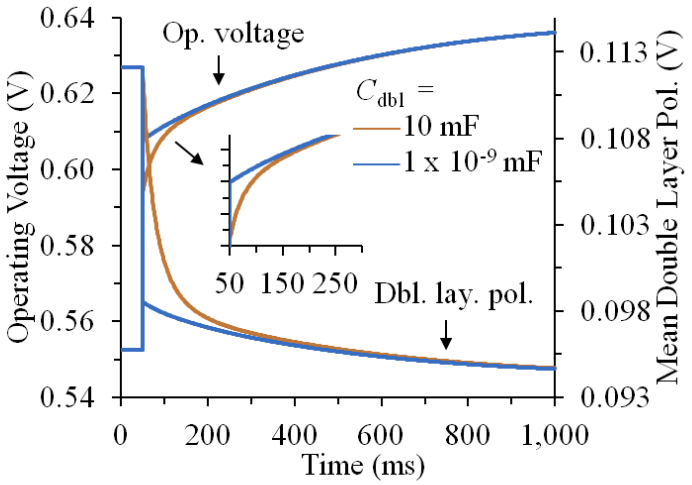


**Figure 7.5** Dynamic response of the SOFC stack initialized to minor deviations from baseline.

while in Fig. 7.6b, the current density decreases from 3000 A/m$^2$ to 2500 A/m$^2$ (step-wise) at 50 ms. When current density increases under the present conditions (Fig. 7.6a), it can be seen that the charge double layer's influence creeps into the second timescale. In fact, the operating voltage appears to exhibit a settling time of approximately 750 ms. Such a settling time could become influential during shorter simulations, particularly those on the second timescale (i.e., simulations with a time horizon of 100 sec. or less). Any additional changes in the operating conditions may give rise to even longer electrochemical settling times, potentially spanning multiple seconds. When the current density decreases (Fig. 7.6b), on the other hand, the settling time is not quite as large, but it is still significant compared to the baseline value (75–100 ms), exhibiting a settling time of approximately 450 ms. Thus, significantly increasing the activation and concentration polarizations appears to give rise to correspondingly long electrochemical settling times.

### 7.3.4 Large Capacitance

Possible values for the double layer capacitance range widely, from very small (hundreds of microFarads) to very large (a few Farads) [26, 64, 130]. This study has so far assumed a balanced value of 10 mF. The actual value of the double layer capacitance, however,

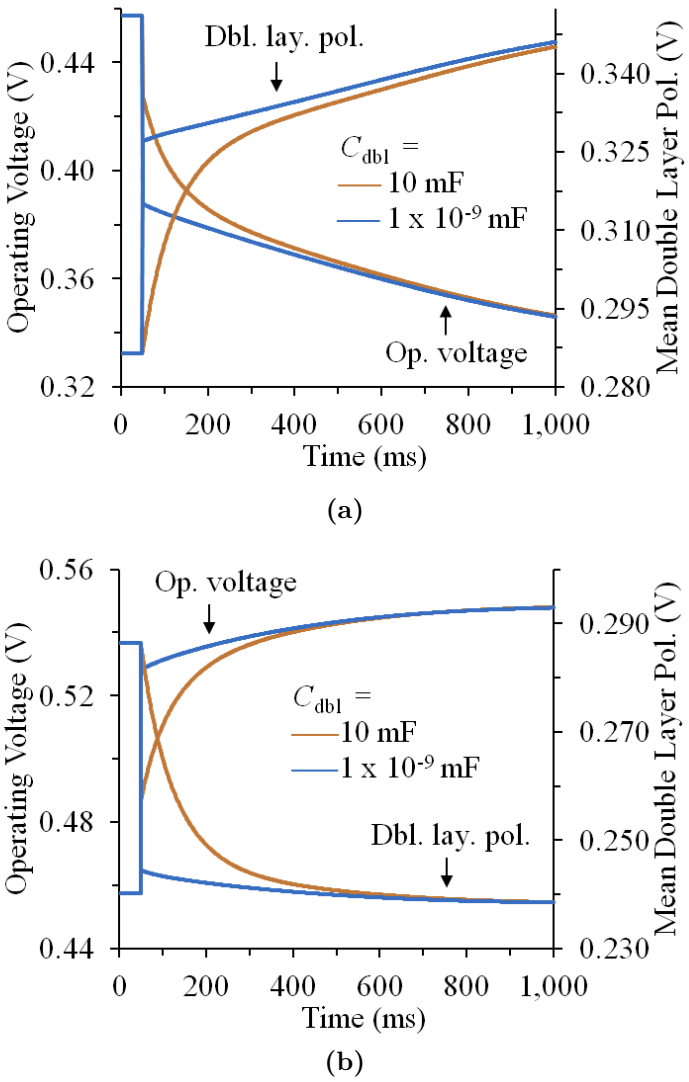


**Figure 7.6** Dynamic response of the SOFC stack initialized to major deviations from baseline: (a) Dynamic response to a step increase in current density, (b) Dynamic response to a step decrease in current density.

depends largely on the electrode's porosity, as the capacitance is directly proportional to the electrode's real surface area [26]. Consequently, the double layer capacitance could change over time, as the porosity of the anode material (Ni-YSZ) is likely to change if redox cycling occurs [162]. For comparison purposes, a large capacitance value of 1 F is considered in the simulations to follow. Figure 7.7 presents the SOFC stack's dynamic response to step changes in current density, assuming that $C_{\text{dbl}} = 1$ F. In these simulations, the SOFC stack is initialized to the baseline conditions (Table 7.1). In Fig. 7.7a, the current density increases

from 3000 A/m$^2$ to 3500 A/m$^2$ (step-wise) at 5 sec., while in Fig. 7.7b, the current density decreases from 3000 A/m$^2$ to 2500 A/m$^2$ (step-wise) at 5 sec. As before, a very small value of the double layer capacitance ($C_{\text{dbl}} = 1 \times 10^{-9}$ mF) is shown for comparison, representing the case where virtually no charge double layer effect is present. Also, as before, the double layer polarization is plotted, and the time response of the double layer polarization is found to agree with that of the operating voltage (for a given capacitance value).

In Fig. 7.7, the charge double layer's settling time is found to be on the order of seconds (between 6 and 7 sec.). Such a settling time is much longer than that previously seen for the baseline case (milliseconds), as well as that for minor deviations from baseline (milliseconds) and major deviations from baseline (milliseconds to seconds). In the context of a larger system, an operating voltage settling time on the order of seconds could influence the system's response to load changes substantially. In particular, SOFC-GT systems often implement multiple controllers that operate on different timescales. Mueller, et al. [57], for instance, controlled the fuel cell stack power by manipulating the fuel flow, and they controlled the combustor temperature (or the amount of fuel leaving the fuel cell stack) relatively quickly by manipulating the current density. Stiller, et al. [22] took a different approach, choosing instead to manipulate the current density to control the system power nearly instantaneously, while manipulating the system fuel flow to control the fuel utilization in a few seconds time. In both of these studies, at least one control loop operated on the second timescale—control of the fuel utilization in Stiller, et al.'s study, and control of the fuel cell stack power in Mueller, et al.'s study—while a different control loop operated on a shorter timescale. If the charge double layer effect does, indeed, extend into the second timescale, then it will likely influence control loops on the second timescale, as well as interactions between control loops on different timescales.

### 7.3.5 PI Control

Finally, the present study investigates the SOFC stack's dynamic response to changes in load under PI control. In an actual load-following scenario, the current density is likely to exhibit patterns other than step changes, which has been assumed along in this study. Stiller, et al. [22], for instance, showed that an SOFC-GT system gradually (rather than abruptly) met

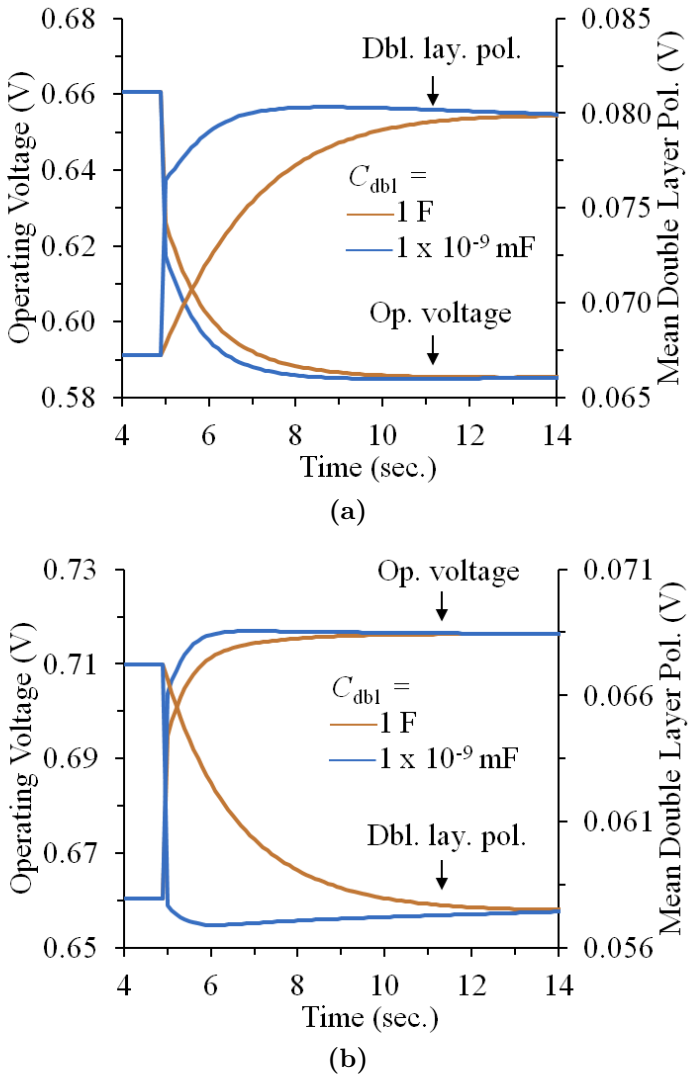


**Figure 7.7** Dynamic response of the SOFC stack initialized to baseline conditions, and $C_{\text{dbl}} = 1$ F: (a) Dynamic response to a step increase in current density, (b) Dynamic response to a step decrease in current density.

demand. In particular, these authors imposed a 47% step change in power demand and found that the SOFC-GT system met the demand in a span of seconds (11 sec. during a power demand decrease and 57 sec. during a power demand increase). Increasing the SOFC stack's power too rapidly could also lead to undesirable operating characteristics, such as excessively high fuel utilization [57]. Thus, the SOFC stack is expected to meet demand gradually, rather than abruptly, in an actual load-following scenario.

In this study, a PI controller is implemented to control the SOFC stack's power in response to a step change in the power demand [22]. The PI controller is based on the discrete controller presented in Ref. [169]. The proportional and integral gains are obtained from trial-and-error tuning in order to meet the new demand in a span of milliseconds to seconds [23, 170]. In these simulations, the current density is the manipulated variable, and the SOFC stack power is the controlled variable. The operating conditions are similar to the baseline conditions presented in Table 7.1, except that the fuel utilization and air ratio are held constant, rather than the inlet fuel flow rate and inlet air flow rate. Specifically, the fuel utilization is maintained at $U_{\mathrm{f}} = 85\%$, and the air ratio is maintained at $\lambda = 7$. It should also be noted that the fuel utilization used in this section differs from that appearing in Section 7.2.1.1 (used to investigate operating conditions that deviate slightly from the baseline case). The fuel utilization used in this section is defined as the ratio of hydrogen consumed (expressed in terms of electric current) to the inlet flow rate of combustible species. The fuel utilization appearing in Fig. 7.2b, on the other hand, is defined as the difference between the inlet and exit flow rates of the combustible species divided by the inlet flow rate of the combustible species. The latter definition has been chosen here for better convergence.

Fig. 7.8 shows the the SOFC stack's controlled response to a step change in power demand. In Fig. 7.8a, the power demand increases by 50% from 64.1 kW to 96.2 kW (where 96.2 kW is the power generated by the SOFC stack under baseline operation) at 50 ms, while in Fig. 7.8b, the power demand decreases from 96.2 kW to 64.1 kW at 50 ms. It can be seen that the dynamic response of the SOFC stack with a small capacitance value agrees well with the stack's response assuming a regular capacitance value, indicating that the controlled system's behavior is nearly independent of the charge double layer. In Fig. 7.8, a small difference is perhaps discernible during the first half of the simulations, as shown in the insets. However, this difference lasts for only milliseconds, and such an effect is not considered significant. It should be kept in mind, however, that the SOFC stack's response in an actual system depends on a number of factors, including controller design, part-load operation of the balance-of-plant components, and the actual power demand.

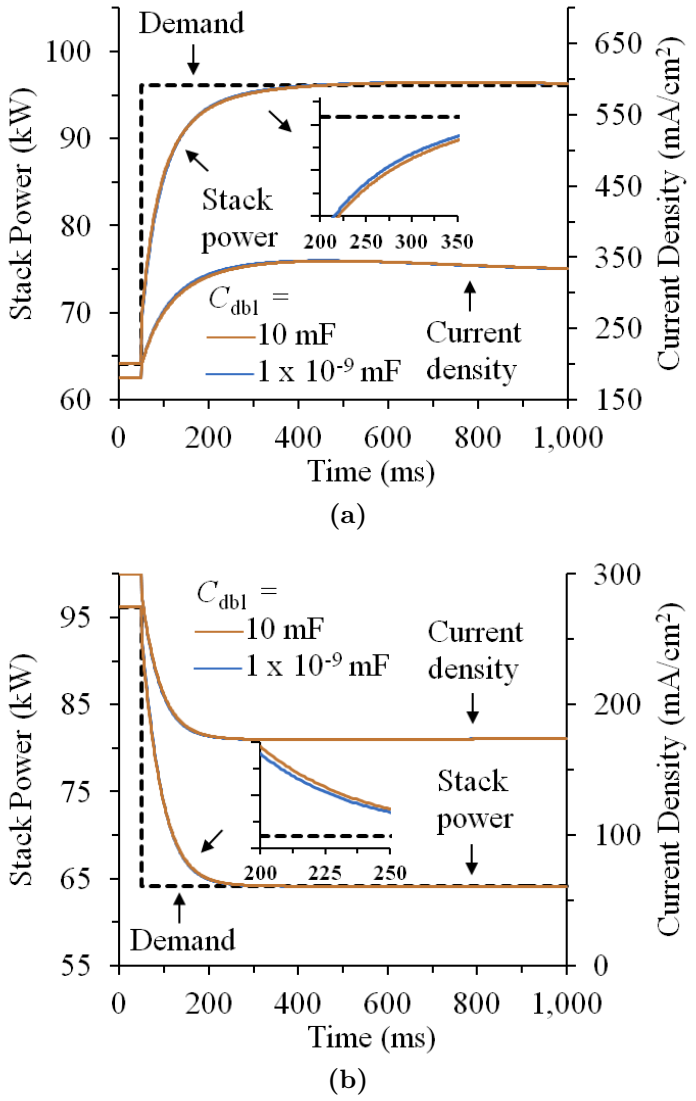


**Figure 7.8** Dynamic response of the closed-loop SOFC stack initialized to baseline conditions and operating under PI control: (a) Dynamic response to a step increase in load, (b) Dynamic response to a step decrease in load.

## 7.4 SUMMARY

The charge double layer may extend beyond the millisecond timescale under certain operating conditions. In general, the charge double layer influenced the SOFC stack's behavior most significantly under the following circumstances: (i) the SOFC stack experienced significant excursions in operation, or (ii) a large double layer capacitance value was assumed. During normal (baseline) operation and minor deviations thereabout, on the other hand, the charge double layer effect was found to be far less influential in terms of the SOFC stack's dynamic behavior. That is, the charge double layer effect diminished within milliseconds, including under PI control. It seems reasonable, then, to exclude the charge double layer under normal operating conditions. Before neglecting the charge double layer, however, careful consideration should be given to possible deviations in operation or material properties, as such changes could give rise to longer electrochemical settling times during operation. The next chapter analyzes the hybrid and non-hybrid systems' performance during steady-state operation. Specifically, the next chapter conducts exergy and economic analyses of the hybrid and non-hybrid systems.

# 8.0 EXERGETIC AND ECONOMIC PERFORMANCE

Exergy and cost are important considerations when evaluating a thermal system's viability. As discussed in Chapter 1, fuel cells present numerous opportunities for improvement over conventional power generation, including cogeneration, high electric efficiency, and enhanced fuel cell performance (in the case of the hybrid system). Hybrid systems, however, remain in the demonstration phase. In order to advance toward commercialization, there is a need to better understand these systems through exergy and cost analyses. The present chapter evaluates the hybrid and non-hybrid systems' energetic, exergetic and economic performances. The thermodynamic model calculates the temperature, pressure, and species mass flow rates throughout each system. The exergy analysis identifies areas for improvement in each system. In addition, the cost model developed in Chapter 5 calculates the systems' life cycle costs. The life cycle costs provide perhaps the most telling indication of the hybrid system's potential for future growth.

## 8.1 DEFINITIONS AND METHODOLOGY

The fuel cell stack and balance-of-plant component models developed in Chapter 5 calculate the temperature, pressure, and species mas flow rates at specific points throughout the hybrid and non-hybrid systems. The thermodynamic models capture changes in the fluid's composition and temperature as the species interact chemically and thermally throughout the system. The thermodynamic model also calculates the parasitic and thermal energy losses within each system. The systems' performance indicators and associated methdology are presented below.

### 8.1.1 Efficiency

The present work evaluates the fuel cell's electric efficiency and the system's overall and exergetic efficiencies. The SOFC's electric efficiency is defined as the ratio of the fuel cell's DC power output to the fuel's higher heating value (evaluated at the anode channel's inlet conditions):

$$\eta_{\text{SOFC}} = \frac{\dot{W}_{\text{SOFC,DC}}}{(\dot{n}_{\text{fuel}} \cdot \overline{\text{HHV}}_{\text{fuel}})_{\text{anode,inlet}}} \tag{8.1}$$

where $\dot{W}_{\text{SOFC,DC}}$ is the DC power generated by the SOFC, $\dot{n}_{\text{fuel}}$ is the anode's inlet molar flow rate, and $\overline{\text{HHV}}_{\text{fuel}}$ is the fuel's higher heating value [56]. The system's electric efficiency is defined in a manner similar to the fuel cell's electric efficiency, but it also includes power generated by the turbine (in the hybrid system), as well as losses due to power conditioning:

$$\eta_{\text{sys,e}} = \frac{\dot{W}_{\text{AC,net}}}{(\dot{n}_{\text{fuel}} \cdot \overline{\text{HHV}}_{\text{fuel}})_{\text{system,inlet}}} \tag{8.2}$$

where $\dot{W}_{\text{AC,net}}$ is the net AC system power, $\dot{n}_{\text{fuel}}$ is the fuel's molar flow rate at the system's inlet, and $\text{HHV}_{\text{fuel}}$ is the fuel's higher heating value at the system's inlet [56]. The system's combined heat and power (CHP, or overall) efficiency also includes thermal energy as a desired output:

$$\eta_{\text{CHP}} = \frac{\dot{W}_{\text{AC,net}} + q_{\text{CHP}}}{(\dot{n}_{\text{fuel}} \cdot \overline{\text{HHV}}_{\text{fuel}})_{\text{system,inlet}}} \tag{8.3}$$

where $q_{\text{CHP}}$ is the recovered thermal energy. Lastly, the exergetic efficiency is defined as the ratio of the exergy of the desired products to the inlet exergy:

$$\varepsilon_{\text{sys}} = \frac{\dot{W}_{\text{AC,net}} + \left(1 - \frac{T_0}{T_b}\right) q_{\text{CHP}}}{(\dot{n}_{\text{fuel}} \cdot \overline{\mathsf{e}}_{\text{f,fuel}})_{\text{system,inlet}}} \tag{8.4}$$

where $T_0$ is the environment's temperature (298 K), $T_{\text{b}}$ is the system's boundary temperature (at which heat transfer occurs), and $\overline{\mathsf{e}}_{\text{f,fuel}}$ is the fuel's flow exergy [87]. The first term in the numerator of Eqn. (8.4) represents the exergy associated with power generation (which is simply the power during steady-state operation). The second term represents the exergy associated with the recovered thermal energy. The factor $(1 - T_0/T_b)$ may be interpreted as the Carnot efficiency, which represents the maximum amount of work that could be obtained from $q_{\text{CHP}}$. The next section discusses exergy in more detail.

### 8.1.2 Exergy

The present work develops an exergy accounting of the hybrid and non-hybrid systems. As defined by Moran, et al. [49], exergy accounting is the evaluation and comparison of the different terms in an exergy balance. The steady-state exergy balance applied to each system component is given by the following equation:

$$0 = \sum_{i=1}^{\#\text{ transfers}} \left(1 - \frac{T_0}{T_i}\right) q_i - \dot{W} + \sum_{i=1}^{\#\text{ inlets}} \dot{n}_{\text{in},i} \overline{\mathsf{e}}_{\text{f,in},i} - \sum_{i=1}^{\#\text{ exits}} \dot{n}_{\text{out},i} \overline{\mathsf{e}}_{\text{f,out},i} - \dot{\mathsf{E}}_{\text{d}} \tag{8.5}$$

where $T_i$ is the boundary temperature (at which heat transfer $q_i$ occurs), $\dot{W}$ denotes power generation, $\dot{n}_{\text{in},i}$ is the molar flow rate entering inlet $i$, $\overline{\mathsf{e}}_{\text{f,in},i}$ is the molar flow exergy entering inlet $i$, $\dot{n}_{\text{in},e}$ is the molar flow rate leaving exit $i$, and $\overline{\mathsf{e}}_{\text{f,in},e}$ is the molar flow exergy leaving exit $i$. Each term on the right-hand side of Eqn. (8.5) is interpreted differently. The first term represents the exergy associated with heat transfer. The second term represents the exergy associated with power generation, which reduces to the power at steady-state. The third and fourth terms represent the exergy accompanying mass entering and exiting the control volume, respectively (expressed on a molar basis). Finally, the fifth term represents the destruction of exergy. Irreversibilities within a system destroy exergy [49].

As mentioned briefly in Chapter 2, exergy is the maximum possible work that a system can produce as it reaches equilibrium with its environment. A system equilibrates with its environment when it assumes the environment's temperature, pressure, and composition. Thus, the flow exergy consists of thermomechanical and chemical contributions. The thermomechanical contribution accounts for differences between the system's temperature and pressure and the environment's conditions (kinetic and potential energies are neglected). The chemical contribution accounts for differences between the system's composition and the environment's composition. The total flow exergy is given by the following formula:

$$\overline{\mathsf{e}}_{\text{f}} = \overline{h} - \overline{h}_0 - T_0 \left(\overline{s} - \overline{s}_0\right) + \overline{\mathsf{e}}^{\text{ch}} \tag{8.6}$$

where $\overline{h}$ is the fluid's molar enthalpy evaluated at the inlet or exit conditions, $\overline{h}_0$ is the fluid's molar enthalpy evaluated at the environment's conditions, $T_0$ is the environment's temperature, $\overline{s}$ is the molar entropy evaluated at the inlet or exit conditions, and $\overline{s}_0$ is the

fluid's molar entropy evaluated at the environment's conditions. The first three terms on the right-hand side of Eqn. (8.5) represent the thermomechanical contribution to the total flow exergy. The last term represents the chemical contribution. The chemical exergy of a substance (denoted by $C_aH_bO_c$, where a, b, and c are specified accordingly) is given by the following formula:

$$\begin{aligned}\overline{\mathsf{e}}^{\mathsf{ch}} = &\left[\overline{g}_{C_aH_bO_c} + \left(a + \frac{b}{2} - \frac{c}{2}\right)\overline{g}_{O_2} - \frac{b}{2}\overline{g}_{H_2O(g)}\right](T_0, p_0) \\ &+ \overline{R}T_0 \ln\left[\frac{\left(y^e_{O_2}\right)^{a+b/4-c/2}}{\left(y^e_{CO_2}\right)^{a}\left(y^e_{H_2O}\right)^{b/2}}\right]\end{aligned} \tag{8.7}$$

where $\overline{g}_{C_aH_bO_c}$ is the molar Gibbs function of the substance under consideration, $\overline{g}_{O_2}$ is the molar Gibbs function of $O_2$, $\overline{g}_{H_2O(g)}$ is the molar Gibbs function of $H_2O$ (vapor), $\overline{R}$ is the universal gas constant, $y^e_{O_2}$ is the mole fraction of $O_2$ in the environment, $y^e_{CO_2}$ is the mole fraction of $CO_2$ in the environment, and $y^e_{H_2O}$ is the mole fraction of $H_2O$ in the environment. In the present work, the environment's temperature and pressure are assumed to be $T_0 = 25°C$ and $p_0 = 1$ atm. The environment's composition is assumed to be $y^e_{H_2O} = 0.0312$, $y^e_{CO_2} = 0.0003$, and $y^e_{O_2} = 0.2035$. Nitrogen makes up the balance.

### 8.1.3 Levelized Cost of Electricity

The cost model presented in Chapter 5 calculates the systems' levelized costs of electricity (LCOEs). The LCOE is a system's annualized life cycle cost. The life cycle cost includes capital, maintenance, and fuel costs. The LCOE formula is revisited below:

$$\text{LCOE} = \frac{R_F C_{sys}}{CF_e A_{plant} \cdot 8,760 \text{ h/yr}} + \sum_i MC_i + \frac{F_c}{\eta_{sys,e}} - \frac{F_c\left(\eta_{CHP} - \eta_{sys,e}\right)}{\eta_{sys,e}\eta_{htg}} \cdot CF_h \quad \text{(5.31 revisited)}$$

where $R_F$ is the capital recovery factor, $C_{sys}$ is the system's total capital cost (\$/kW), $CF_e$ is the electric capacity factor, $A_{plant}$ is the plant's availability, $MC_i$ is the maintenance cost of component $i$ (\$/kWh), $F_c$ is the fuel cost (\$/kWh), $\eta_{sys,e}$ is the system's electric efficiency, $\eta_{CHP}$ is the system's overall efficiency, $\eta_{htg}$ is the conventional heating system's efficiency, and $CF_h$ is the heating capacity factor. Table 8.1 presents the cost model's parameters. As discussed in Chapter 5, the maintenance cost includes replacement costs only (it does not

include inspection, cleaning, and smaller component replacement costs). The fuel cell stack is replaced every five years, as is the pre-reformer. The desulfurizer's sorbent is replaced every year. The fuel cost is assumed to be the average commercial natural gas price in 2014 of 3.0 ¢/kWh [171]. The heating capacity factor is assumed to be 100%, meaning that the building uses all of the thermal energy recovered by the system. The component costs come from various studies, as discussed in Chapter 5, and the cost estimates are scaled appropriately.

### 8.1.4 Operating Conditions

Table 8.1 presents the hybrid and non-hybrid systems' operating conditions. For reference, Table 8.1 also includes the university building's baseload power demand and baeload thermal energy demand. As discussed in Chapter 5, the baseload power and thermal energy demands represent a university building's constant power and thermal energy loads. In the present study, both systems are sized to generate a constant 65 $kW_e$ to meet the building's baseload power demand, and recovered thermal energy is assumed to go toward heating hot water. The heat recovery heat exchanger's exit temperature is specified to be 25°C above the exhaust's dew point temperature to avoid condensation and corrosion inside the heat exchanger. In addition, air enters the fuel cell stack in the amount necessary to maintain an average PEN temperature of 750°C, and the cathode air temperature rise is specified to be 150°C.

Several parameters appearing in Table 8.1 need to be defined. The system's fuel utilization represents the portion of the system's fuel that is oxidized inside the fuel cell stack:

$$U_{\text{f,sys}} = \frac{\dot{n}_{\text{H}_2,\text{consumed}}}{4\dot{n}_{\text{CH}_4,\text{sys}}} \tag{8.8}$$

where $U_{\text{f,sys}}$ is the system's fuel utilization, $\dot{n}_{\text{H}_2,\text{consumed}}$ is the amount of fuel consumed by the fuel cell stack, and $\dot{n}_{\text{CH}_4,\text{sys}}$ is the molar flow rate of $CH_4$ entering the system [56]. The denominator of Eqn (8.8) represents the amount of $H_2$ yielded if the reforming and water-gas shift reactions were brought to completion. In the pre-reformer, the steam-to-carbon ratio (S/C ratio) is 2 to avoid the formation of solid carbon. The S/C ratio is defined as follows:

$$\text{S/C} = \frac{\dot{n}_{\text{H}_2\text{O,AGR}}}{\dot{n}_{\text{CH}_4,\text{fresh}} + \dot{n}_{\text{CO,AGR}} + \dot{n}_{\text{CH}_4,\text{AGR}}} \tag{8.9}$$

where $\dot{n}_{H_2O,AGR}$ is the molar flow rate of $H_2O$ recycled back to the pre-reformer's inlet (AGR stands for anode gas recycle), $\dot{n}_{CH_4,fresh}$ is the molar flow rate of fresh $CH_4$ entering the pre-reformer, $\dot{n}_{CO,AGR}$ is the amount of recycled CO, and $\dot{n}_{CH_4,AGR}$ is the amount of recycled $CH_4$ [96]. Thirty percent of the inlet $CH_4$ is pre-reformed to reduce temperature gradients inside the fuel cell stack.

## 8.2 THERMODYNAMIC EVALUATIONS

The thermodynamic models evaluate the temperature, pressure, and species mass flow rates throughout each system. Figure 8.1 presents the hybrid system's flow diagram. Air enters the air compressor in the amount necessary to maintain the fuel cell's average temperature at 750°C. The heat of compression increases the air's temperature to 178°C. The air pre-heater heats the air to 681°C, which is necessary to maintain the specified cathode air temperature rise. The system's exhaust provides the requisite thermal energy. Meanwhile, fuel enters the system in the amount necessary to generate 65 kW (assuming 85% fuel utilization). The hot recycled anode gas raises the fuel's temperature to 689°C prior to entering the pre-reformer, and the pre-reformer converts 30% of the $CH_4$ into the reformate. The pre-reformer also pre-heats the fuel to the SOFC stack's specified inlet fuel temperature of 700°C. The system's exhaust again provides the requisite thermal energy. The fuel reacts with the air in the fuel cell stack, generating most of the system's power (45.4 $kW_e$, after conditioning). The system's exhaust then passes through the microturbine, generating additional power (20.3 $kW_e$). Finally, the exhaust passes through the heat recovery heat exchanger, recovering 22.2 $kW_{th}$ of thermal energy. It should be noted that the hybrid system meets 25% of the building's thermal energy demand (89 $kW_{th}$, as presented in Table 8.1).

Figure 8.2 presents the non-hybrid system's flow diagram. Similar to the hybrid system, air enters the air compressor in the amount necessary to maintain the fuel cell's average temperature at 750°C, and fuel enters the system in the amount necessary to generate 65 $kW_e$ (assuming 85% fuel utilization). The air pre-heater heats the air to 655°C, which is necessary to maintain the specified cathode air temperature rise. The recycled anode gas

**Table 8.1** Operating, economic, and building parameters.

| Parameter | System | |
|---|---|---|
| | Hybrid | Non-hybrid |
| *Operating parameters* | | |
| Net power ($kW_e$) | 65 | 65 |
| System fuel utilization | 0.85 | 0.85 |
| S/C ratio | 2 | 2 |
| Pre-reforming extent (%) | 30 | 30 |
| Operating voltage (V) | 0.7 | 0.7 |
| Average PEN temperature (°C) | 750 | 750 |
| Cathode temperature rise (°C) | 150 | 150 |
| Anode inlet temperature (°C) | 700 | 700 |
| Pressure ratio | 4:1 | - |
| Inverter efficiency (%) | 95 | 95 |
| Generator efficiency (%) | 98 | - |
| Mechanical efficiency (shaft) (%) | 98 | - |
| Air blower efficiency (%) | - | 75 |
| Air compressor efficiency (%) | 85 | - |
| Fuel compressor efficiency (%) | 75 | 75 |
| Turbine efficiency (%) | 85 | - |
| *Economic parameters* | | |
| System's life time (years) | 20 | 20 |
| Stack replacement (years) | 5 | 5 |
| Reformer catalyst replacement (years) | 5 | 5 |
| Desulfurizer sorbent replacement (years) | 1 | 1 |
| Fuel cost (¢/kWh) | 3.0 | 3.0 |
| Discount rate (%) | 10 | 10 |
| Equipment inflation rate (%) | 2.8 | 2.8 |
| Electric capacity factor (%) | 90 | 90 |
| Plant availability (%) | 99 | 99 |
| Heating capacity factor (%) | 100 | 100 |
| *Building's parameters* | | |
| Baseload power demand ($kW_e$) | 65 | 65 |
| Baseload thermal energy demand ($kW_{th}$) | 89 | 89 |

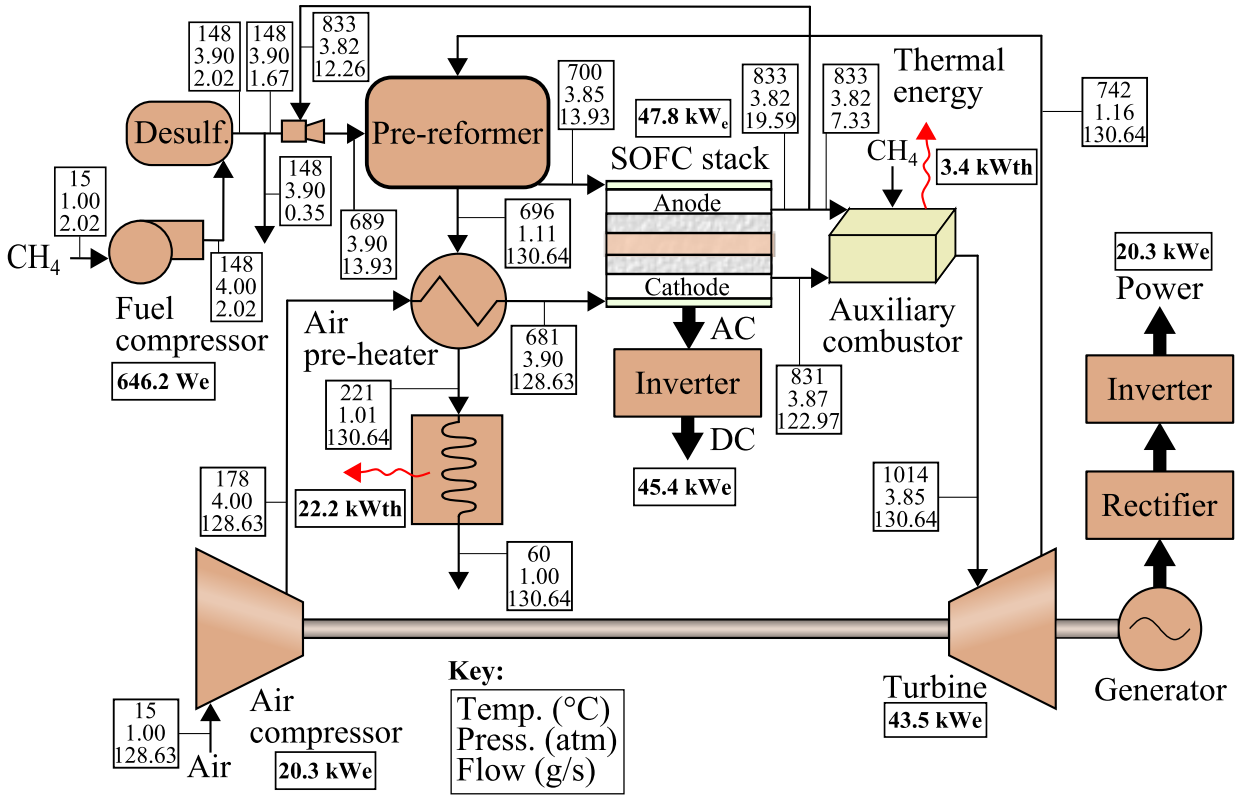


**Figure 8.1** Hybrid system's process flow diagram.

heats the fuel to 653°C, and the pre-reformer again provides the thermal energy necessary to meet the fuel cell stack's specified inlet fuel temperature of 700 °C. The fuel reacts with the air in the fuel cell stack, generating 71.8 $kW_e$ (after conditioning). The exhaust pre-heats the fuel and air, and the heat recovery heat exchanger recovers 49.8 $kW_{th}$ of thermal energy. Notice that the non-hybrid system recovers nearly twice as much thermal energy as the hybrid system. The non-hybrid system removes the turbine (and its associated temperature drop) from the system, thus increasing the system's exhaust temperature. The exhaust's mass flow rate is also larger in the non-hybrid system. These conditions facilitate greater thermal energy recovery, although the non-hybrid system requires more fuel to meet a given power demand.

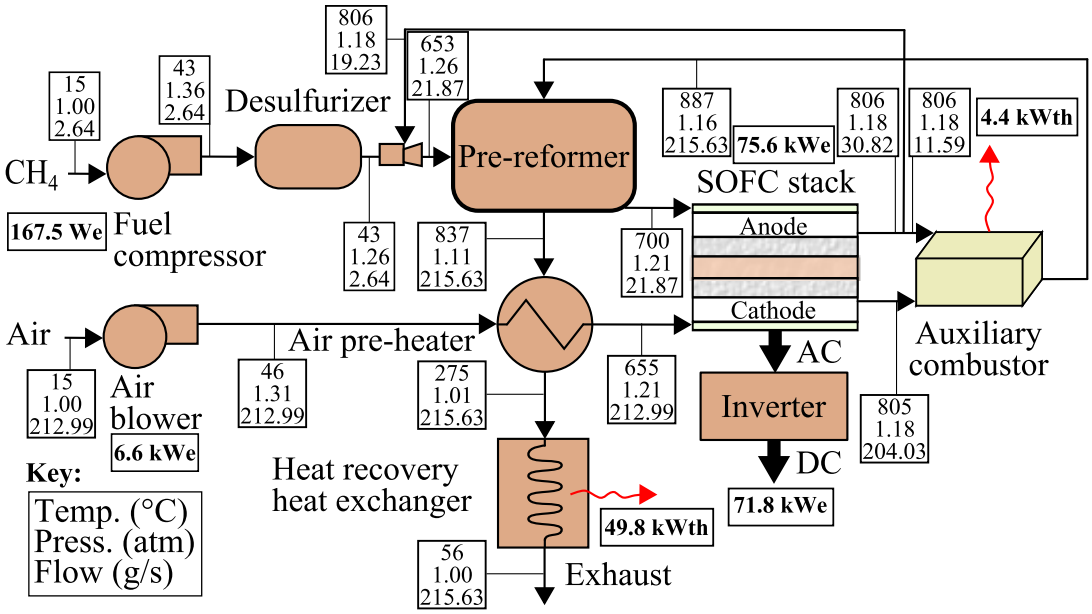


**Figure 8.2** Non-hybrid system's process flow diagram.

## 8.3 PERFORMANCE INDICATORS

Table 8.2 presents the hybrid and non-hybrid systems' performance indicators. The hybrid system operates at an electric efficiency of 57.9% and exergetic efficiency of 64.1%. The system's exergetic efficiency is higher than its electric efficiency because the exergetic efficiency includes thermal energy as a useful output (multiplied by the Carnot efficiency), as presented in Eqn. (8.4). The system's CHP efficiency (77.8%), on the other hand, is higher than both its electric and exergetic efficiencies. Unlike the exergetic efficiency, which multiplies the thermal energy by the Carnot efficiency, the CHP efficiency does not account for the usefulness (or value) of the thermal energy. Consequently, the CHP efficiency includes a higher thermal contribution. In contrast, the fuel cell's electric efficiency is fairly low (36.4%). The anode gas recycle reduces the SOFC's fuel utilization, thus reducing the fuel cell's electric efficiency. Under the present operating conditions, 62.6% of the anode exhaust is recycled back to the pre-reformer's inlet (not shown). Consequently, the SOFC's fuel utilization is $U_{f,1} = 67.2\%$ (not shown), compared to the system's fuel utilization of $U_{f,sys} = 85\%$ (Ta-

**Table 8.2** Performance indicators.

| | SOFC's electric efficiency (%) | System's electric efficiency (%) | CHP efficiency | Exergetic efficiency |
|---|---|---|---|---|
| Hybrid system | 36.4 | 57.9 | 77.8 | 64.1 |
| Non-hybrid system | 36.5 | 44.3 | 78.3 | 50.7 |

ble 8.2). The outcome is a relatively high system electric efficiency, but a relatively low SOFC electric efficiency.

The non-hybrid system operates at an electric efficiency of 44.3% and exergetic efficiency of 50.7%. The non-hybrid system's electric and exergetic efficiencies fall 13% below those of the hybrid system due to the microturbine's absence. That is, the non-hybrid system requires more fuel to meet the specified demand, relying entirely on the SOFC stack. Similar to the hybrid system, the non-hybrid system's exergetic efficiency is several percentage points higher than its electric efficiency. Again, the hybrid system's exergetic efficiency includes thermal energy as a useful output, converted to its work-equivalent value. Interestingly, the non-hybrid system's overall efficiency nearly equals that of the hybrid system, despite the non-hybrid system's relatively low electric efficiency. Evidently, the non-hybrid system's recovered thermal energy offsets its lower power output. That is, the energy that does not got toward generating power in the non-hybrid system instead goes toward cogenerating thermal energy.

The systems' electric, CHP, and exergetic efficiencies provide insight into each system's fuel requirement. Clearly, the hybrid system exhibits lower electric and exergetic efficiencies than the non-hybrid system. Consequently, during power-only operation (i.e., during lack of heat demand), the hybrid system would require less fuel to meet a given power demand. During cogeneration operation (as assumed in the present study), on the other hand, the non-hybrid system presents certain benefits. The non-hybrid system generates less power than the hybrid system, but it cogenerates more thermal energy, giving rise to a CHP efficiency that is on par with that of the non-hybrid system (Table 8.2), and potentially equivalent or greater fuel savings. In the present work, the cost model accounts for fuel savings by subtracting

the avoided cost of a conventional heater from the systems' LCOEs (Eqn. (5.31)). The cost model's results presented in Section 8.6 capture the fuel savings attributable to cogeneration.

## 8.4 EXERGY ACCOUNTING

Table 8.3 presents the hybrid system's exergy accounting. The left column represents the exergy associated with power generation, as well as the exergy associated with thermal energy recovery. The right column represents the exergy that is either destroyed or lost. In the hybrid system, the auxiliary combustor exhibits the largest exergy destruction/loss. The auxiliary combustor destroys 9.55% of the system's inlet exergy, and the combustor loses 2.46% of the inlet exergy in the form of thermal energy (Table 8.3 sums these contributions together). The fuel cell stack exhibits the second largest exergy destruction rate, destroying 5.51% of the system's inlet exergy. Interestingly, the highest exergy destruction occurs in the components involving chemical or electrochemical reactions, which are the auxiliary combustor and fuel cell stack, respectively. The rotating components, on the other hand, operate relatively efficiently due to their high isentropic efficiencies. These results agree with those of Calise, et al. [61]. The turbine-compressor destroys less than 5% of the inlet exergy, and the fuel compressor destroys less than 1%. The power conditioning also causes slight losses, and less than 2% of the inlet exergy leaves the system with the exhaust. The remaining components contribute only a few percent to the system's total exergy destruction. Notice, also, that the sum of the left and right columns in Table 8.3 equals 100%, thus serving as a check on the present model. The system's exergetic efficiency is given by the left column's sum (64.12%), which agrees with the value provided in Table 8.2.

Table 8.4 presents the non-hybrid system's exergy accounting. Clearly, the air pre-heater exhibits the largest exergy destruction. The air pre-heater destroys 16.95% of the system's inlet exergy, compared to only 2.67% in the hybrid system. The auxiliary combustor exhibits the second largest exergy destruction rate, destroying 8.84% of the system's inlet exergy, followed by the the heat recovery heat exchanger (7.93%) and the fuel cell stack (7.04%). Again, the chemical and electrochemical reactions inside the auxiliary combustor and fuel cell

**Table 8.3** Hybrid system's exergy accounting. (All values are expressed as a percentage of the system's inlet exergy.)

| | Power or useful thermal energy (%) | Exergy destroyed or lost (%) |
|---|---|---|
| Fuel cell stack | 43.24 | 5.51 |
| Fuel compressor | −0.62 | 0.11 |
| Turbine-air compressor | 19.29 | 4.23 |
| Desulfurizer | - | 0.01 |
| Pre-reformer | - | 0.88 |
| Ejector | - | 1.10 |
| Air pre-heater | - | 2.67 |
| Heat recovery | 2.21 | 3.67 |
| Power conditioning (stack) | - | 2.28 |
| Power conditioning (turb-comp) | - | 1.85 |
| Auxiliary combustor | - | 12.01 |
| Exhaust | - | 1.55 |
| Sum | 64.12 | 35.87 |

stack give rise to irreversibilities inside these components. The heat recovery heat exchanger also destroys a significant amount of exergy. The thermal energy obtained from cooling the system's exhaust evidently comes at a cost. Similar to the hybrid system, the fuel compressor, air blower, and power conditioning destroy only small amounts of exergy. The recovered thermal energy again constitutes a small portion of the system's exergetic output (3.39%).

The previous results suggest possible avenues for improving system performance. First, both systems exhibit relatively high exergy destruction rates in the fuel cell stack. The fuel cell stack's performance depends on many operating parameters, as explained in previous chapters, including the operating voltage, pressure, temperature, and fuel utilization. Increasing the fuel cell's operating voltage and temperature typically improves the fuel cell's electric efficiency, but doing so also increases the stack's capital costs. Hence, there is a need to systematically consider different combinations of operating parameters while also considering the trade-off between capital and operating costs [97]. Second, the non-hybrid system's

**Table 8.4** Non-hybrid system's exergy accounting. (All values are expressed as a percentage of the system's inlet exergy.)

| | Power or useful thermal energy (%) | Exergy destroyed or lost (%) |
|---|---|---|
| Fuel cell stack | 52.25 | 7.04 |
| Fuel compressor | −0.12 | 0.03 |
| Air blower | −4.83 | 1.14 |
| Desulfurizer | - | 0.02 |
| Pre-reformer | - | 1.72 |
| Ejector | - | 1.48 |
| Air pre-heater | - | 16.95 |
| Heat recovery | 3.39 | 7.93 |
| Power conditioning (stack) | - | 2.75 |
| Auxiliary combustor | - | 8.84 |
| Exhaust | - | 1.43 |
| Sum | 50.69 | 49.33 |

air pre-heater exhibits the highest exergy destruction in this system. As displayed in Figs. 8.1 and 8.2, the air flow rate is greater in the non-hybrid system than in the hybrid system. The temperature rise across the air pre-heater is also greater in the non-hybrid system than in the hybrid system. Consequently, significant heat transfer occurs in the air pre-heater, resulting in significant exergy destruction. In order to improve the air pre-heater's performance, cathode gas recycle may be employed. Cathode gas recycle is the recirculation of cathode exhaust to the air channel's inlet, thus pre-heating the incoming air. The resulting additional cost of such a system, however, may again deter the immediate adoption of this measure [97]. Lastly, the auxiliary combustor exhibits high exergy destruction in both systems. Improving combustor performance is thus a third avenue for improving system performance.

## 8.5 LIFE CYCLE COST

Figure 8.3 presents the hybrid and non-hybrid systems' levelized costs of electricity (LCOEs), as well as the average retail electricity price in the U.S. for commercial customers. The LCOEs are segmented into their capital, maintenance, and fuel contributions. Interestingly, the hybrid system's capital and maintenance costs fall below those of the non-hybrid system, despite the system's additional component (the turbine). It should be remembered, however, that the microturbine's maintenance cost includes replacement costs only, and not inspection, cleaning, or smaller component costs. The microturbine's relatively low cost likely results from economies of production. As discussed in Chapter 5, the present study adopts a microturbine cost estimate provided by the U.S. Environmental Protection Agency (EPA) for a 30 kW microturbine manufactured by Capstone Turbine Corporation. Capstone manufactures microturbines for a wide range of customers, and these units typically come pre-packaged with a turbine, air compressor, combustor, and recuperator. Other system components, such as the fuel cell stack, pre-reformer, and air blower, are more customized, implying lower production volumes and likely higher capital costs. In addition, the non-hybrid system exhibits fuel costs similar to those of the hybrid system. Evidently, the non-hybrid system recovers sufficient thermal energy to offset its lower electric efficiency. Even with these fuel savings, however, the hybrid system yields a lower LCOE than the non-hybrid system. The hybrid system's LCOE is 8.7 ¢/kWh, whereas the non-hybrid system's LCOE is 11.9 ¢/kWh.

The foregoing analysis suggests that hybrid systems will likely be economically competitive at some point in the future. The hybrid system exhibits a relatively low LCOE of 8.7 ¢/kWh. For comparison, the average retail electricity price in the U.S. for commercial customers is 10.8 ¢/kWh (2014 USD) (Fig. 8.3) [172]. Thus, hybrid systems have the potential to save money, assuming that their capital cost remains sufficiently low. It is important to recognize, however, that the present study integrates the fuel cell stack with an existing (packaged) microturbine. Hence, the microturbine's cost estimate benefits from economies of production. In the near future, production volumes may not even exceed 250 units/year, particularly as these systems begin to move beyond the demonstration phase. The Pacific

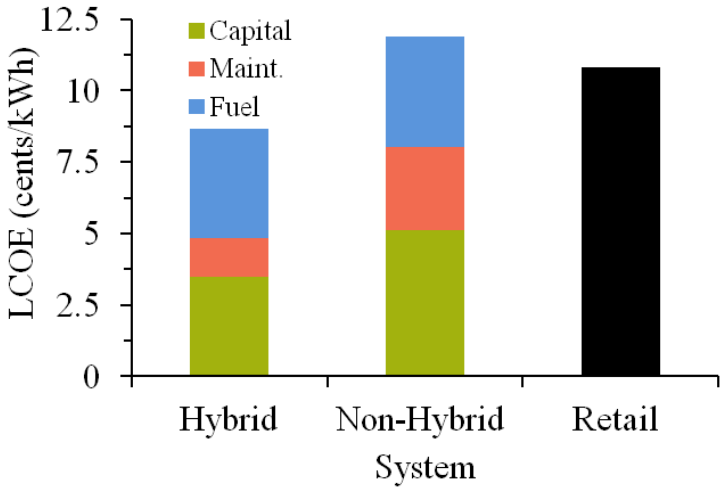


**Figure 8.3** Hybrid and non-hybrid systems' LCOEs (the average retail U.S. electricity price is shown for comparison).

Northwest National Laboratory analyzed the economic performance of a 270 kW hybrid system, considering a range of production volumes. The authors found that production volumes less than 250 units/year corresponded to LCOEs exceeding 20 ¢/kWh. Thus, while hybrid systems may be economically competitive as packaged entities, early-stage (customized) systems will likely be significantly more expensive.

Figure 8.4 presents the systems' component costs. Figures 8.4a and 8.4b depict the four largest contributions to the hybrid and non-hybrid systems' capital costs, respectively. The "other" category includes all other component costs (not including labor, equipment, or installation). The microturbine constitutes 42% of the hybrid system's capital cost. This result is not surprising, considering that the microturbine includes the turbine, air compressor, combustor, and recuperator in a single package; hence, it represents the cost of not only the prime mover but also multiple balance-of-plant components. The inverter, stack, and reformer each constitute between 14% and 18% of the hybrid system's capital cost. Inverters tend to be relatively expensive in low power applications, particularly kW-scale applications [156]. The non-hybrid system, on the other hand, requires greater stack area, giving rise to a greater fuel cell cost contribution (Fig. 8.4b). The fuel cell stack constitutes

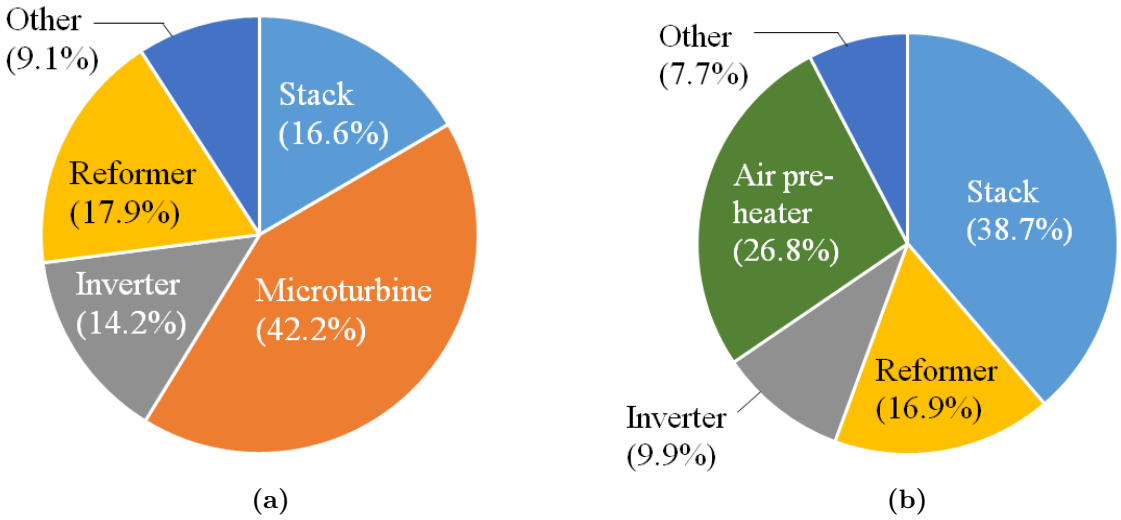


**Figure 8.4** Component costs: (a) Hybrid system, (b) Non-hybrid system.

39% of the non-hybrid system's capital cost. The air pre-heater also constitutes a relatively large contribution, followed by the pre-reformer and inverter. Unlike the hybrid system, the non-hybrid system does not package any of these components together. Each component cost is estimated separately, which probably contributes to their higher expense.

## 8.6 SUMMARY

A thermal system's viability depends on many factors. The present chapter compared the hybrid system's energetic, exergetic, and economic performances to those of a non-hybrid system during baesload operation. The hybrid system operated at higher electric and exeretic efficiencies than the non-hybrid system, suggesting that the hybrid system may be preferable during power-only operation. During cogeneration operation, on the other hand the non-hybrid system yielded a CHP efficiency and fuel cost on par with those of the hybrid system. The exergetic analysis further revealed inefficiencies associated with the fuel cell stack and auxiliary combustor in both systems. The air pre-heater in the non-hybrid

system also exhibited significant exergy destruction. Changing the fuel cell stack's operation may improve the system's performance, as may cathode gas recycle, but consideration should also be given to the additional capital costs associated with these measures. Lastly, the hybrid system exhibited a lower LCOE than the non-hybrid system. The cost model assumes, however, an existing (packaged) microturbine. Initial hybrid systems will likely be much more expensive. The next chapter briefly presents the hybrid and non-hybrid systems' environmental performance.

# 9.0 ENVIRONMENTAL PERFORMANCE

While fuel cell systems operate efficiently, they face certain environmental challenges. Fuel cell systems emit $CO_2$ during operation; natural gas reforming and auxiliary combustion produce $CO_2$. In 2013, the U.S. Environmental Protection Agency (EPA) proposed $CO_2$ regulations on new power plants. Electricity generation currently accounts for 31% of the greenhouse gas emissions in the U.S. [173], and to address environmental concerns, the EPA proposed rate-based standards on MW-scale fossil fuel-fired power plants. The present study compares the hybrid and non-hybrid systems' emissions to the EPA regulations. The present study also compares the systems' emissions to those of more conventional distributed generation technologies, including reciprocating internal combustion engines, gas turbines, and microturbines. Lastly, the present study compares the systems' emissions to those from coal and natural gas power plants. Similar to the previous chapter, the hybrid and non-hybrid systems are assumed to generate constant (baseload) power.

## 9.1 OPERATING CONDITIONS

The hybrid and non-hybrid systems operate according to the conditions presented in Chapter 8 (Table 8.1.) In particular, the hybrid and non-hybrid systems generate a constant 65 kW to meet a university building's baseload power demand. Fuel is supplied in the amount required to meet the building's demand while also maintaining a fuel utilization of 85% (thus avoiding concentration losses inside the fuel cell stack). Unused fuel exits the fuel cell stack and reacts with exhaust air in the auxiliary combustor, driving the microturbine (in the hybrid system) or pre-heating the fuel and air (in the non-hybrid system). Mean-

while, air is supplied in the amount required to maintain an average fuel cell temperature of 750°C. The fuel cell thus operates in the intermediate-temperature regime, permitting the use of less expensive metallic interconnects. The cathode air temperature rise remains fixed at 150°C, as before, in order to minimize temperature gradients inside the fuel cell stack. While both systems recover thermal energy, the $CO_2$ calculations herein do not incorporate cogenerated thermal energy. All carbon dioxide emissions are expressed in units of kg $CO_2$ per kWh of net power generated, thus excluding any thermal output.

## 9.2 EMISSION REGULATIONS

In 2013, the EPA proposed federal $CO_2$ regulations on fossil fuel-fired power plants. Currently, states implement their own efficiency measures to address carbon pollution, such as energy efficiency codes for buildings and demand-side efficiency programs. The EPA's standards, however, would apply uniformly to all states [174, 175]. In the present work, the EPA's standards serve as a benchmark for distributed power generation. While the EPA's standards technically target MW-scale power plants (rather than small-scale generators), fuel cell systems are emerging technologies that may be subject to similar standards in the future.

### 9.2.1 Proposed Standards

On September 20, 2013, the EPA proposed emission standards for new power plants. The proposed standards would legally require power plants with capacities exceeding 25 MW to limit their $CO_2$ production. In particular, the EPA proposed that new combustion turbines with a heat input greater than 850 MMBtu/h (approximately 100 $MW_e$) be required to limit their emissions to 1,000 $lb_m$ $CO_2$/MWh (0.45 kg $CO_2$/kWh), while those with a heat input less than or equal to 850 MMBtu/h would need to limit their emissions to 1,100 $lb_m$ $CO_2$/MWh (0.50 kg $CO_2$/kWh). The EPA also proposed that utility boilers and integrated gasification combined cycle plants be required to meet a stan-

dard of 1,000 $lb_m$ $CO_2$/MWh (0.45 kg $CO_2$/kWh) over a one year period, or 1,000–1,050 $lb_m$ $CO_2$/MWh (0.45–0.48 kg $CO_2$/kWh) over a seven year period [27]. On June 2, 2014, the EPA proposed emission standards for modified and reconstructed power plants, as well as rate-based emission goals for existing power plants. These guidelines are more system and state-specific. The proposed standards for new power plants, on the other hand, would apply uniformly to all states.

### 9.2.2 System Performance

Figure 9.1 compares the hybrid and non-hybrid systems' $CO_2$ emissions to the EPA's proposed standard for (smaller) new combustion turbines. The hybrid system emits 0.31 kg $CO_2$/kWh, whereas the non-hybrid system emits 0.40 kg $CO_2$/kWh. The far left column displays the EPA's proposed standard for combustion turbines (assuming a heat input less than or equal to 850 MMBTU/h), which is 0.50 kg $CO_2$/kWh. Evidently, both systems meet the proposed standard. That is, the hybrid and non-hybrid systems both emit less $CO_2$ than the proposed standard under the assumed operating conditions. The hybrid system, in fact, emits nearly 0.20 kg $CO_2$/kWh less than the standard. The hybrid system also emits less $CO_2$ than the non-hybrid system due to its higher electric efficiency. If thermal energy were treated as a credit (as in the cost model), however, then the non-hybrid system may produce lower $CO_2$ emissions than the hybrid system. In addition, during load changes, the systems may emit more or less $CO_2$, depending on their operating points. Under the present operating conditions (baseload), however, both systems appear to operate satisfactorily.

## 9.3 CONVENTIONAL TECHNOLOGIES

Fuel cells present opportunities for improvement over conventional fossil fuel-fired technologies. Fuel cells electrochemically convert fuel into electricity, operating at relatively high electric efficiencies. Conventional fossil fuel-fired technologies, on the other hand, convert thermal energy into mechanical energy, and then convert mechanical energy into electricity.

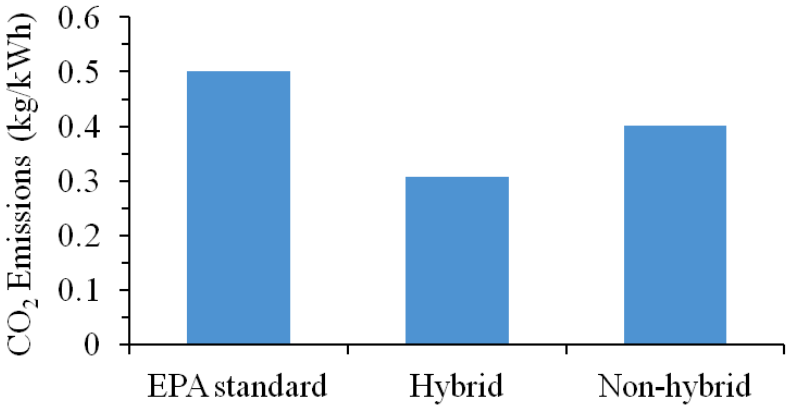


**Figure 9.1** Hybrid and non-hybrid systems' emissions. The far left column displays EPA's proposed standard for new combustion turbines (assuming a heat input less than or equal to 850 MMBTU/h).

Thus, conventional systems tend to operate at lower electric efficiencies. The present work compares the hybrid and non-hybrid systems' emissions to those from more conventional fossil fuel-fired technologies. The EPA's *Catalog of CHP Technologies* provides emissions data for reciprocating internal combustion engines, gas turbines, and microturbines [5]. The following section compares these estimates to the hybrid and non-hybrid systems' performance.

### 9.3.1 Distributed Generation

Figure 9.2 compares the hybrid and non-hybrid systems' emissions to those of the conventional systems. The reciprocating internal combustion engine emits the least $CO_2$ out of the conventional systems (0.67 kg $CO_2$/kWh). The gas turbine and microturbine each emit approximately 0.75 kg $CO_2$/kWh. Most notably, all of the conventional systems exceed the EPA's proposed standard of 0.50 kg $CO_2$/kWh. Thus, these systems may not address environmental concerns in the near future. It is furthermore evident that the hybrid and non-hybrid systems emit less $CO_2$ than the conventional systems. The conventional systems operate at an electric efficiency of approximately 25% (HHV). The hybrid and non-hybrid systems, on the other hand, operate at electric efficiencies of 58% (HHV) and 44% (HHV),

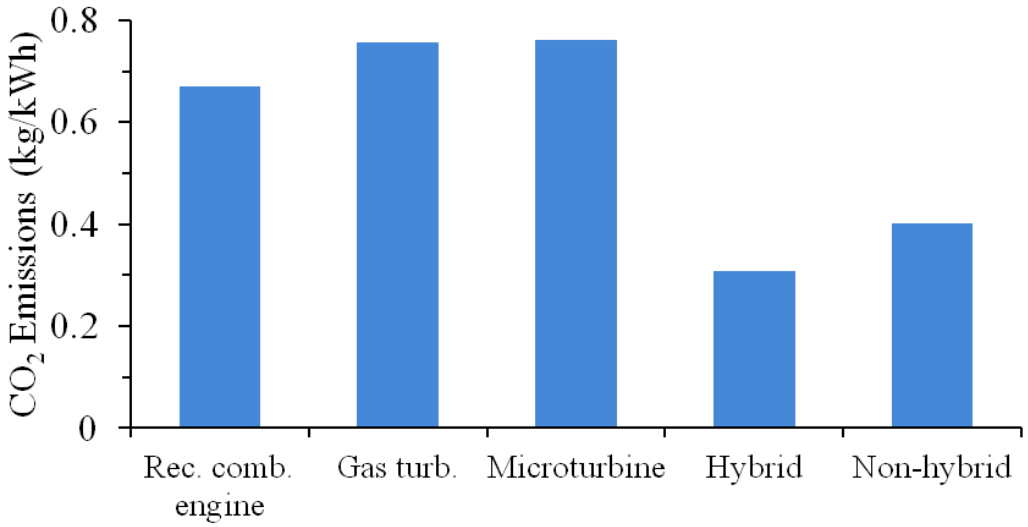


**Figure 9.2** Hybrid and non-hybrid systems' emissions compared to those from more conventional distributed generation systems [5].

respectively. The hybrid and non-hybrid systems' higher electric efficiencies give rise to lower emissions. As mentioned previously, however, the present study does not account for the environmental benefit of cogenerating thermal energy. Reciprocating internal combustion engines, gas turbines, and microturbines frequently cogenerate thermal energy, which (effectively) reduces their $CO_2$ emissions and may influence the results shown here.

### 9.3.2 U.S. Power Sector

Finally, Figure 9.3 compares the conventional systems' emissions to those from the U.S. power sector, which comprises mostly electric utilities and independent power producers [111, 112]. Figure 9.3 presents the emissions associated with coal and natural gas-fueled power plants. Not surprisingly, coal-fueled power plants emit the most $CO_2$ out of all the systems considered (1 kg $CO_2$/kWh). Natural gas-fueled power plants, on the other hand, emit 0.43 kg $CO_2$/kWh. Thus, natural gas-fueled power plants emit only slightly more $CO_2$ than the non-hybrid system. These results suggest that natural gas-fueled plants may remain competitive with distributed generation systems within the foreseeable future, although

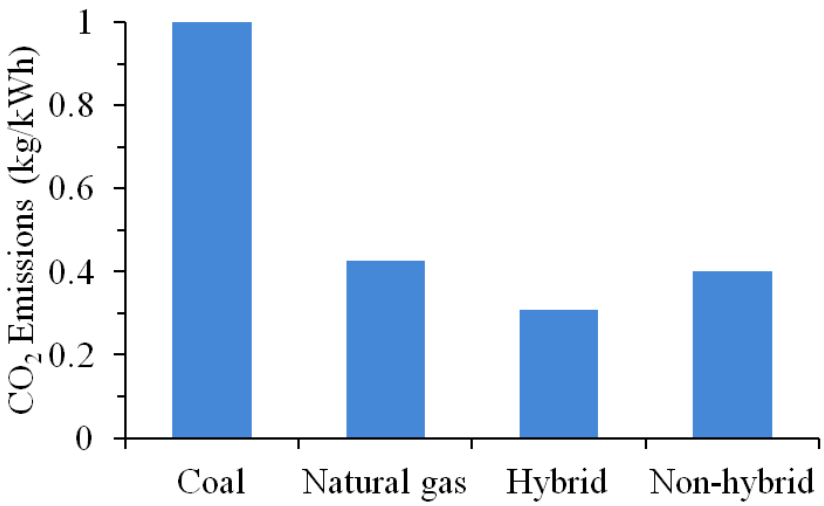


**Figure 9.3** Hybrid and non-hybrid systems' emissions compared to those from the U.S. power sector in 2014 (only coal and natural gas sources are shown).

transmission and distribution losses may further increase the natural gas sources' emissions. The hybrid system emits the lowest $CO_2$ out of all the technologies shown.

## 9.4 SUMMARY

Fuel cell systems provide distributed energy at relatively high electric efficiencies. The hybrid and non-hybrid systems emit 0.31 kg $CO_2$/kWh and 0.40 kg $CO_2$/kWh under the assumed operating conditions, respectively. Thus, these systems meet the EPA's standard for new combustion turbines, which is 0.50 kg $CO_2$/kWh for small combustion turbines. In addition, the hybrid and non-hybrid systems emit less $CO_2$ than more conventional distributed generation systems, including reciprocating internal combustion engine, gas turbines, and microturbines. The hybrid and non-hybrid systems also emit significantly less $CO_2$ than coal-fueled power plants, while remaining competitive with natural gas-fueled power plants. The next chapter is the final chapter, and it concludes the present work. The final chapter also provides possible directions for future work.

# 10.0 CONCLUSIONS AND FUTURE WORK

The present work developed and analyzed a hybrid solid oxide fuel cell microturbine (SOFC-MT) system model. The present work looked closely at the fuel cell stack's dynamic performance, as well as the hybrid and non-hybrid systems' thermodynamic performance. The fuel cell stack model consisted of electrochemical, species mass, energy, and momentum balances, allowing for dynamic simulations on multiple timescales. The hybrid and non-hybrid system models integrated the fuel cell stack with the balance-of-plant components. The system models calculated the energy and exergy flows throughout the prime mover(s) and balance-of-plant components, including thermal and chemical interactions between these components. The thermodynamic models also calculated the $CO_2$ emissions, allowing for evaluation of the hybrid and non-hybrid systems' environmental performance. The cost model calculated the systems' levelized costs of electricity, representing the systems' annualized life cycle costs. The following section discusses the present work's conclusions in more detail, followed by possible directions for future work.

## 10.1 CONCLUSIONS

Hybrid systems offer numerous potential benefits, including cogeneration, high electric efficiency, and enhanced fuel cell performance. Hybrid systems, however, remain in the demonstration phase. In order to advance toward commercialization, the present work addressed several issues related to hybrid systems' performance, including fuel cell control strategies, exergetic performance, and life cycle cost. In accordance with the contributions discussed throughout this study, the conclusions presented herein are divided into four sections. The

first section discusses the fuel cell stack's dynamic response to control variables. The second section discusses the fuel cell stack's electrochemical settling time. The third section discusses the systems' exergetic and economic performances. The final section discusses the systems' environmental performance.

### 10.1.1 Response to Control Variables

The present study investigated the SOFC stack's dynamic response to step changes in the inlet fuel flow rate, current density, and inlet air flow rate. The fuel cell model calculated changes in the fuel utilization, power, and fuel cell's average temperature on millisecond, second, and minute timescales. These latter variables typically require control in an SOFC-GT system for safety and efficiency reasons, while the inlet fuel flow rate, current density, and air flow rate may be manipulated to control these other variables. For simplicity, all dynamic simulations excluded the balance-of-plant components. The dynamic simulations instead focused on the fuel cell stack's behavior, as processes inside fuel cells are highly coupled. The fuel cell stack model operated at an inlet pressure of 4 bar, and the stack consumed fuel with an inlet fuel composition based on a 30% pre-reformed steam-methane mixture. Such conditions reflect typical SOFC-MT operating conditions.

Two possible control strategies emerged as feasible for operating the fuel cell stack. The first strategy involved manipulating the inlet fuel flow rate to control the SOFC stack's power, while manipulating the current density to control the fuel utilization. The second strategy (a reverse of the first) involved manipulating the current density to control the SOFC stack's power, while manipulating the inlet fuel flow rate to control the fuel utilization. Importantly, the former strategy required tight control of the fuel utilization in order to significantly change the power (by varying the inlet fuel flow rate). Otherwise, the inlet fuel flow rate negligibly influenced the fuel cell stack's power. The latter strategy, on the other hand, placed no restrictions on the fuel utilization. That is, changing the current density significantly changed the power, regardless of the fuel utilization's value. Thus, the latter strategy would likely provide greater independence between control loops in a cascade controller. Minimizing interdependence is desired because it reduces the risk of oscillations

between control loops in a cascade controller. The latter strategy also exhibited faster power responses. That is, the power responded instantaneously to current density changes, whereas it responded over the course of seconds to changes in the inlet fuel flow rate. The latter strategy would thus enhance load-following.

### 10.1.2 Electrochemical Settling Time

In addition to investigating the fuel cell stack's dynamic response to control variables, the present work investigated the fuel cell's sensitivity to the charge double layer. While the electrochemical settling time often lasts only milliseconds following a load change, the present work investigated possible operating conditions that may give rise to longer electrochemical settling times, thereby potentially influencing the fuel cell stack's control logic. The electrochemical model's equivalent circuit combined the charge double layer with the ohmic, activation, and concentration polarizations. Similar to the simulations discussed above, the fuel cell stack model excluded the balance-of-plant components. Nonetheless, the fuel cell stack operated under typical SOFC-MT conditions, as mentioned before. The present work investigated the fuel cell stack's electrochemical settling time by defining baseline operating conditions, as well as minor and major deviations from the baseline conditions. The present study also investigated the SOFC stack's performance under proportional-integral (PI) control, assuming an unusually large value of the double layer capacitance.

In general, the charge double layer influenced the SOFC stack's behavior most significantly under the following circumstances: (i) the SOFC stack experienced large increases in the activation and concentration polarizations, and/or (ii) the SOFC stack operated with a large capacitance value. In particular, the charge double layer significantly influenced the SOFC stack's behavior when the activation and concentration polarizations increased five-fold, representing the potential outcome of fuel cell degradation processes or equipment failure. Under such conditions, the voltage settling time reached approximately 750 ms, suggesting that the charge double layer could influence the fuel cell stack's behavior on the second timescale. The present study also found that increasing the charge double layer capacitance to $C_{\text{dbl}} = 1$ F significantly lengthened the electrochemical settling time. During

normal (baseline) operation and minor deviations thereabouts, however, the charge double layer effect diminished within milliseconds. Under PI control, the charge double layer, again, negligibly influenced the fuel cell stack's behavior. It seems reasonable, then, to exclude the charge double layer under normal operating conditions. However, careful consideration should be given to possible deviations in operation or material properties that could give rise to longer electrochemical settling times.

### 10.1.3 Exergy and Economic Analyses

The system models integrated the fuel cell stack with the balance-of-plant components. In the hybrid system, the SOFC stack generated most of the power, and the fuel cell stack's exhaust drove the microturbine, generating additional power. The non-hybrid system, on the other hand, relied entirely on the SOFC stack to meet the given power demand, and the exhaust exited the system soon after pre-heating the fuel and air streams. Both systems generated a constant 65 kW to meet a university building's baseload power demand, and it was assumed that cogenerated thermal energy could be used to meet the building's hot water demand. The energy and exergy flows permitted calculation of the systems' overall performance (electric and combined heat and power (CHP) efficiencies), as well as inefficiencies within individual components (exergy destruction and loss). The systems' electric and CHP efficiencies factored directly into the cost model. The cost model calculated the systems' levelized costs of electricity (LCOEs), which included capital, maintenance, and fuel costs, as well as a cogeneration credit. The cost model approximated each component cost based on previous estimates, and scaled these estimates as appropriate.

In general, the hybrid system competed well with the non-hybrid system. The hybrid system operated at higher electric and exergetic efficiencies than the non-hybrid system. The non-hybrid system, on the other hand, cogenerated greater thermal energy than the hybrid system, leading to similar fuel costs between the systems during cogeneration operation. The exergy analysis further revealed possible avenues for improving the systems' performance. The fuel cell stack and auxiliary combustor exhibited high exergy destruction rates in both systems. This means that these components exhibited the highest inefficiency,

and thus, these components (as well as the air pre-heater) deserve the most consideration when improving system performance. Varying the fuel cell stack's operating parameters and employing cathode gas recycle are possible remedies. The hybrid system furthermore yielded a lower LCOE than the non-hybrid system. The hybrid system cost 8.7 ¢/kWh, whereas the non-hybrid system cost 11.9 ¢/kWh. The hybrid system also competed well with the average retail electricity price in the U.S. These results suggest that hybrid systems will likely become economically competitive at some point in the future. It should be recognized, however, that the present study integrated the SOFC stack with an existing (packaged) microturbine. Packaged systems typically benefit from economies of production, yielding lower capital costs. During early stages of development, however, hybrid systems will likely cost significantly more than more conventional systems.

### 10.1.4 Environmental Analysis

Fuel cell systems are emerging, fossil-fuel fed technologies that may someday be subject to environmental regulations. The EPA recently proposed that a limit of 0.50 kg $CO_2$/kWh be placed on small (less than 100 $MW_e$) new combustion turbines. Under the assumed operating conditions, the hybrid system emitted 0.31 kg $CO_2$/kWh, and the non-hybrid system emitted 0.40 kg $CO_2$/kWh. Thus, if so required as some point in the future, the hybrid and non-hybrid systems would be capable of meeting the EPA's proposed standard. The hybrid and non-hybrid systems furthermore emitted less $CO_2$ than more conventional distributed generation systems, including reciprocating internal combustion engines, gas turbines, and microturbines. In fact, these more conventional technologies currently exceed the EPA's proposed limit of 0.50 kg $CO_2$/kWh. Lastly, the hybrid and non-hybrid systems emitted less $CO_2$ than coal-fueled power plants, while remaining competitive with natural gas-fueled power plants. The fuel cells systems' low emissions (relative to other systems) stems from their relatively high electric efficiencies.

## 10.2 FUTURE WORK

The present study has laid the groundwork for future research on hybrid systems. There is a need to further evaluate (and improve, as necessary) hybrid systems' performance through modeling and simulation. In particular, it is recommended that future work address system dynamics and optimization. The following sections briefly discuss each of these potential directions.

### 10.2.1 System Dynamics

Employing hybrid systems in distributed generation applications requires not only excellent thermodynamic performance but also the ability to follow a dynamic load. Residential, university, and office buildings experience significant load changes over the course of a day [149, 160, 161]. In order for hybrid systems to meet these needs, quick and efficient dynamic response is required. Several authors have considered hybrid system dynamics, including Martinez, et al. [23,63], Stiller, et al. [22], Mueller, et al. [57], and Roberts and Brouwer [33]. Perhaps the most diverse modeling assumption among these authors, however, is their choice of control strategy. There is a need to compare possible control strategies at the system level, looking closely at the system's allowable (safe) operating range, as well as how quickly the system responds to load changes. While the present study's findings are intended to inform control decisions at the system level, they do not serve as a substitute for system-level studies. In an actual system, the SOFC stack is subject to changes in operating conditions that have heretofore been considered static, such as changes in the fuel cell stack's inlet temperature and pressure. Such changes may give rise to unforeseen interactions between the the fuel cell stack and balance-of-plant components. The fuel processing system may further complicate operation by delaying fuel delivery to the fuel cell stack. Thus, an actual system's operation may differ significantly from that assumed herein during steady-state operation.

### 10.2.2 System Optimization

The present study compared the hybrid and non-hybrid systems' costs under a single set of operating parameters. It is recommended that future work consider many different sets of operating parameters. In particular, future studies could optimize the hybrid and non-hybrid systems, varying the average fuel cell temperature, operating voltage, current density, and similar parameters to minimize the systems' life cycle costs. In the case of the hybrid system, consideration could also be given to different pressure ratios and turbine inlet temperatures. In addition to considering different operating parameters, different system configurations could also be considered. If the system operates in parallel with the grid, for instance, then baseload operation may be an option. (Duffie and Beckman's $P_1, P_2$ method is particularly well-suited for calculating the life cycle cost of a fuel cell system and utility combined [97, 150].) If the system operates grid-independently, on the other hand, then the system will likely require a secondary power source if the system is to load-follow. Trade-offs exist between improving system efficiency and reducing costs, and there is a need to systematically evaluate the various configurations and sets of operating conditions to minimize the system's life cycle cost.

## 10.3 SUMMARY

Hybrid systems demonstrate the potential to compete with more conventional technologies. Hybrid systems operate at relatively high electric efficiencies, thus reducing their fuel costs and carbon emissions. Hybrid systems also exhibit superior exergetic performance compared to non-hybird systems, indicating better utilization of fuel. In addition, hybrid systems have the ability to cogenerate thermal energy, recovering thermal energy from the system's exhaust, although probably to a lesser extent than non-hybrid systems. Perhaps the biggest challenge facing hybrid systems is the requirement to meet dynamic loads. Although findings from the present study suggest the feasibility of safely and efficiently operating the fuel cell stack dynamically, no substitute can be made for system-level studies. It is recommended

that future work address system dynamics and optimization, looking closely at the interactions between the fuel cell stack and balance-of-plant components. Minimizing the life cycle cost of both hybrid and non-hybrid systems is an important goal for future research.

# BIBLIOGRAPHY


[1] N. Strachan. *Encyclopedia of Energy*, chapter Distributed Energy, Overview. Elsevier, Inc., London, United Kingdom, 2004.

[2] B. Shively and J. Ferrare. *Understanding Today's Electricity Business*. Enerdynamics Corp., Laporte, CO, sixth edition, 2012.

[3] Refrigerating American Society of Heating and Air-Conditioning (ASHRAE). *Heating, Ventilating, and Air-Conditioning Systems and Equipment (SI Edition)*, chapter Combined Heat and Power Systems, pages 7.1–7.9. ASHRAE, Atlanta, GA, 2012.

[4] A. Thumann and P. D. Mehta. *Handbook of Energy Engineering*. Fairmont Press, Inc., Lilburn, GA, sixth edition, 2008.

[5] K. Darrow, R. Tidball, J. Wang, and A. Hampson. Catalog of CHP Technologies. Accessed online at ⟨http://www.epa.gov/chp/technologies.html⟩, U.S. Environmental Protection Agency, 2015.

[6] N. Petchers. *Combined Heating Cooling & Power Handbook–Technologies & Applications*. The Fairmont Press, Inc., Lilburn, GA, second edition, 2012.

[7] M. Bollen and F. Hassan. *Integration of Distributed Generation in the Power System*. Institute of Electrical and Electronics Engineers, Hoboken, NJ, 2011.

[8] N. El Bassam, P. Maegaard, and M. L. Schlichting. *Distributed Renewable Energies for Off-Grid Communities: Strategies and Technologies Towards Achieving Sustainability in Energy Generation and Supply*. Elsevier Inc., Waltham, MA, 2013.

[9] Doosan Fuel Cell America, Inc. Project Profiles. Accessed online at ⟨http://www.doosanfuelcell.com/en/resources/profiles.do⟩ (see document titled, "Coca-Cola Refreshments"). Accessed on July 21, 2015, Copyright 2015.

[10] FuelCell Energy, Inc. Inland Empire Utilities Agency (IEUA) Case Study. Accessed online at ⟨http://www.fuelcellenergy.com/news-resources/white-papers/inland-empire-utilities-agency-ieua-case-study/⟩. Accessed on July 21, 2015, Copyright 2013.

[11] Capstone Turbine Corporation. Case Studies. Accessed online at ⟨http://www.capstoneturbine.com/case-studies/listing/all?c=north-america⟩ (see document titled, "Dominion Transmission Crayne Compressor Station"). Accessed on July 21, 2015, Copyright 2015.

[12] Capstone Turbine Corporation. Case Studies. Accessed online at ⟨http://www.capstoneturbine.com/case-studies/listing/all?c=north-america⟩ (see document titled, "Salem Community College"). Accessed on July 21, 2015, Copyright 2015.

[13] Capstone Turbine Corporation. Case Studies. Accessed online at ⟨http://www.capstoneturbine.com/case-studies/listing/all?c=north-america⟩ (see document titled, "Foothill College"). Accessed on July 21, 2015, Copyright 2015.

[14] S. M. Kaplan. Electric Power Transmission: Background and Policy Issues. Accessed online at ⟨http://fpc.state.gov/documents/organization/122949.pdf⟩, Congressional Research Service, 2009.

[15] U.S. Energy Information Administration. How much electricity is lost in transmission and distribution in the United States? Accessed online at ⟨http://www.eia.gov/tools/faqs/faq.cfm?id=105&t=3⟩. Accessed on July 21, 2015, Last Updated July 10, 2015.

[16] FlexEnergy. Brochures and Spec Sheets. Online at ⟨http://www.flexenergy.com/flexenergy_literature.html⟩ (see documents titled, "Flex Turbine GT250S," and, "Flex Turbine GT333S'"). Accessed on July 21, 2015, Copyright 2014.

[17] S&C Electric Company. The Role of Energy Storage in Smart Microrids. Accessed online at ⟨http://www.sandc.com/news/index.php/2013/07/white-paper-the-role-of-energy-storage-in-smart-microgrids/⟩ (see document). Accessed on July 21, 2015, Copyright 2014.

[18] S. H. Chan, H. K. Ho, and Y. Tian. Modelling for Part-Load Operation of Solid Oxide Fuel Cell-Gas Turbine Hybrid Power Plant. *Journal of Power Sources*, 114(2):213–227, 2003.

[19] S. H. Chan, H. K. Ho, and Y. Tian. Modelling of Simple Hybrid Solid Oxide Fuel Cell and Gas Turbine Power Plant. *Journal of Power Sources*, 109(1):111–120, 2002.

[20] S. H. Chan, H. K. Ho, and Y. Tian. Multi-Level Modeling of SOFC–Gas Turbine Hybrid System. *International Journal of Hydrogen Energy*, 28(8):889–900, 2003.

[21] S. Campanari. Full Load and Part-Load Performance Prediction for Integrated SOFC and Microturbine Systems. *Journal of Engineering for Gas Turbines and Power*, 122(2):239–246, 2000.

[22] C. Stiller, B. Thorud, O. Bolland, R. Kandepu, and L. Imsland. Control Strategy for a Solid Oxide Fuel Cell and Gas Turbine Hybrid System. *Journal of Power Sources*, 158(1):303–315, 2006.

[23] A. S. Martinez, J. Brouwer, and G. S. Samuelsen. Feasibility Study for SOFC-GT Hybrid Locomotive Power: Part I. Development of a Dynamic 3.5 MW SOFC-GT FORTRAN Model. *Journal of Power Sources*, 213:203–217, 2012.

[24] Capstone Turbine Corporation. Media Assets. Online at ⟨http://www.capstoneturbine.com/news/media-assets⟩ (see document titled "Product Catalog English"). Accessed on July 21, 2015, Copyright 2015.

[25] Bloom Energy. ES-5710 Energy Server. Online at ⟨http://www.bloomenergy.com/fuel-cell/es-5710-data-sheet/⟩. Accessed on July 21, 2015, Copyright 2014.

[26] J. Larminie and A. Dicks. *Fuel Cell Systems Explained*. John Wiley & Sons, Ltd., Chichester, England, second edition, 2003.

[27] U.S. Environmental Protection Agency. Standards of Performance for Greenhouse Gas Emissions From New Stationary Sources: Electric Utility Generating Units (IA2. Summary of Major Provisions, IIIA1. Covered EGUs, Generally, IIIB1a. Emission Standard, IIIB2. 84-Operating-Month Rolling Average Compliance Option). Accessed online at ⟨https://www.federalregister.gov/articles/2014/01/08/2013-28668/standards-of-performance-for-greenhouse-gas-emissions-from-new-stationary-sources-electric-utility⟩. Accessed on July 21, 2015.

[28] U.S. Environmental Protection Agency. Carbon Pollution Emission Standards for Modified and Reconstructed Stationary Sources: Electric Utility Generating Units (IA2. Summary of the Major Provisions and IIIA. Applicability Requirements). Accessed online at ⟨https://www.federalregister.gov/articles/2014/06/18/2014-13725/carbon-pollution-standards-for-modified-and-reconstructed-stationary-sources-electric-utility⟩. Accessed on July 21, 2015.

[29] U.S. Environmental Protection Agency. Carbon Pollution Emission Standards for Existing Stationary Sources: Electric Utility Generating Units (IA2. Summary of the Proposal's Major Provisions and VC. Affected Sources). Accessed online at ⟨https://www.federalregister.gov/articles/2014/06/18/2014-13726/carbon-pollution-emission-guidelines-for-existing-stationary-sources-electric-utility-generating⟩. Accessed on June 1, 2015.

[30] A. Osman and R. Ries. Life Cycle Assessment of Electrical and Thermal Energy Systems for Commercial Buildings. *The International Journal of Life Cycle Assessment*, 12(5):308–316, 2007.

[31] V. Karakoussis, N. P. Brandon, M. Leach, and R. van der Vorst. The Environmental Impact of Manufacturing Planar and Tubular Solid Oxide Fuel Cells. *Journal of Power Sources*, 101(1):10–26, 2001.

[32] S. E. Veyo, L. A. Shockling, J. T. Dederer, J. E. Gillett, and W. L. Lundberg. Tubular Solid Oxide Fuel Cell/Gas Turbine Hybrid Cycle Power Systems: Status. *Journal of Engineering for Gas Turbines and Power*, 124(4):845–849, 2002.

[33] R. A. Roberts and J. Brouwer. Dynamic Simulation of a Pressurized 220 kW Solid Oxide Fuel-Cell-Gas-Turbine Hybrid System: Modeled Performance Compared to Measured Results. *Journal of Fuel Cell Science and Technology*, 3(1):18–25, 2006.

[34] National Fuel Cell Research Center. NFCRC Research Summaries. Accessed online at ⟨http://www.nfcrc.uci.edu/3/RESEARCH/ResearchSummaries/Default.aspx⟩ (see link titled "Analyses of Hybrid Fuel Cell Gas Turbine Systems"). Accessed on July 21, 2015, Copyright 2013.

[35] National Fuel Cell Research Center. NFCRC Research Summaries. Accessed online at ⟨http://www.nfcrc.uci.edu/3/RESEARCH/ResearchSummaries/Default.aspx⟩ (see document titled, "HYBRID–220 kW SOFC/Micro Turbine Generator System"). Accessed on July 21, 2015, Copyright 2013.

[36] FuelCell Energy, Inc. Solid Oxide Fuel Cells. Online at ⟨http://www.fuelcellenergy.com/advanced-technologies/solid-oxide-fuel-cells/⟩ (see article titled "Hybrid Power Systems"). Accessed on May 11, 2015, Copyright 2013.

[37] Bloom Energy. What is an Energy Server? Accessed online at ⟨http://www.bloomenergy.com/fuel-cell/energy-server/⟩. Accessed on July 21, 2015, Copyright 2014.

[38] Bloom Energy. Customers. Accessed online at ⟨http://www.bloomenergy.com/customer-fuel-cell/⟩. Accessed on July 21, 2015, Copyright 2014.

[39] Acumentrics Holding Corporation. SOFC Products. Accessed online at ⟨http://www.acumentrics.com/sofc-products-overview.htm⟩. Accessed on July 21, 2015, Copyright 2015.

[40] Protonex. P200i. Accessed online at ⟨http://www.protonex.com/products/p200i/⟩. Accessed on July 21, 2015, Copyright 2015.

[41] Capstone Turbine Corporation. Products. Accessed online at ⟨http://www.capstoneturbine.com/products⟩. Accessed on July 21, 2015, Copyright 2015.

[42] FlexEnergy. Applications. Accessed online at ⟨http://www.flexenergy.com/flexenergy_applications.html⟩. Accessed on May 11, 2015, Copyright 2014.

[43] R. P. O'Hayre, S.-W. Cha, W. G. Colella, and F. B. Prinz. *Fuel Cell Fundamentals*. John Wiley & Sons, Inc., Hoboken, NJ, second edition, 2009.

[44] EG&G Technical Services, Inc. Fuel Cell Handbook. Accessed online at ⟨https://www.netl.doe.gov/File%20Library/research/coal/energy%

20systems/fuel%20cells/FCHandbook7.pdf⟩, U.S. Department of Energy, Office of Fossil Energy, National Energy Technology Laboratory, 2004.

[45] T. Malkow. *Modeling Solid Oxide Fuel Cells: Methods, Procedures and Techniques*, volume 1, chapter SOFC in Brief, pages 3–12. Springer Science+Business Media, B.V., Dordrecht, Netherlands, 2008.

[46] J. Meusinger, E. Riensche, and U. Stimming. Reforming of Natural Gas in Solid Oxide Fuel Cell Systems. *Journal of Power Sources*, 71(1–2):315–320, 1998.

[47] M. Poppinger and H. Landes. Aspects of the Internal Reforming of Methane in Solid Oxide Fuel Cells. *Ionics*, 7(1–2):7–15, 2001.

[48] T. M. Gür, H. Michael, and A. V. Virkar. High performance solid oxide fuel cell operating on dry gasified coal. *Journal of Power Sources*, 195(4):1085–1090, 2010.

[49] M. J. Moran, H. N. Shapiro, D. D. Boettner, and M. B. Bailey. *Fundamentals of Engineering Thermodynamics*. John Wiley & Sons, Inc., Hoboken, NJ, 2011.

[50] Y. Matsuzaki and I. Yasuda. Electrochemical Oxidation of $H_2$ and CO in a $H_2$–$H_2O$–CO-$CO_2$ System at the Interface of a Ni–YSZ Cermet Electrode and YSZ Electrolyte. *Journal of The Electrochemical Society*, 147(5):1630–1635, 2000.

[51] K. Ahmed and K. Föger. Fuel Processing for High-Temperature High-Efficiency Fuel Cells. *Industrial & Engineering Chemistry Research*, 49(16):7239–7256, 2010.

[52] S. Hosseini, S. M. Jafarian, and G. Karimi. Performance Analysis of a Tubular Solid Oxide Fuel Cell with an Indirect Internal Reformer. *International Journal of Energy Research*, 35(3):259–270, 2011.

[53] T. Takeguchi, Y. Kani, T. Yano, R. Kikuchi, K. Eguchi, K. Tsujimoto, Y. Uchida, A. Ueno, K. Omoshiki, and M. Aizawa. Study on Steam Reforming of $CH_4$ and $C_2$ Hydrocarbons and Carbon Deposition on Ni-YSZ Cermets. *Journal of Power Sources*, 112(2):588–595, 2002.

[54] B. F. Kolanowski. *Guide to Microturbines*. The Fairmont Press, Inc., Lilburn, GA, 2004, Chapter 5: Markets for the Microturbine, pp. 41–62.

[55] L. Goldstein, B. Hedman, D. Knowles, S. I. Freedman, R. Woods, and T. Schweizer. Gas-Fired Distributed Energy Resource Technology Characterizations. Accessed online at ⟨http://www.nrel.gov/docs/fy04osti/34783.pdf⟩ NREL/TP-620-34783, Gas Research Institute and National Renewable Energy Laboratory, Golden, CO, 2003, Chapter 4: Microturbine Systems.

[56] R. J. Braun, S. A. Klein, and D. T. Reindl. Evaluation of System Configurations for Solid Oxide Fuel Cell-Based Micro-Combined Heat and Power Generators in Residential Applications. *Journal of Power Sources*, 158(2):1290–1305, 2006.

[57] F. Mueller, R. Gaynor, A. E. Auld, J. Brouwer, F. Jabbari, and G. S. Samuelsen. Synergistic Integration of a Gas Turbine and Solid Oxide Fuel Cell for Improved Transient Capability. *Journal of Power Sources*, 176(1):229–239, 2008.

[58] F. Leucht, W. G. Bessler, J. Kallo, K. A. Friedrich, and H. Müller-Steinhagen. Fuel Cell System Modeling for Solid Oxide Fuel Cell/Gas Turbine Hybrid Power Plants, Part I: Modeling and Simulation Framework. *Journal of Power Sources*, 196(3):1205–1215, 2011.

[59] D. Bhattacharyya, R. Rengaswamy, and C. Finnerty. Dynamic Modeling and Validation Studies of a Tubular Solid Oxide Fuel Cell. *Chemical Engineering Science*, 64(9):2158–2172, 2009.

[60] M. Gandiglio, A. Lanzini, P. Leone, M. Santarelli, and R. Borchiellini. Thermoeconomic Analysis of Large Solid Oxide Fuel Cell Plants: Atmospheric vs. Pressurized Performance. *Energy*, 55:142–155, 2013.

[61] F. Calise, M. Dentice d'Accadia, A. Palombo, and L. Vanoli. Simulation and Exergy Analysis of a Hybrid Solid Oxide Fuel Cell (SOFC)-Gas Turbine System. *Energy*, 31(15):3278–3299, 2006.

[62] F. Calise, A. Palombo, and L. Vanoli. Design and Partial Load Exergy Analysis of Hybrid SOFC-GT Power Plant. *Journal of Power Sources*, 158(1):225–244, 2006.

[63] A. S. Martinez, J. Brouwer, and G. S. Samuelsen. Feasibility Study for SOFC-GT Hybrid Locomotive Power Part II. System Packaging and Operating Route Simulation. *Journal of Power Sources*, 213:358–374, 2012.

[64] M. H. Nehrir and C. Wang. *Modeling and Control of Fuel Cells: Distributed Generation Applications*. John Wiley & Sons, Inc., Hoboken, NJ, 2009, pages 53–55, chapter 2.

[65] R. S. Gemmen. *Modeling Solid Oxide Fuel Cells: Methods, Procedures and Techniques*, volume 1, chapter Dynamic Modeling of Fuel Cells, pages 269–322. Springer Science+Business Media, B.V., Dordrecht, Netherlands, 2008.

[66] Y. Qi, B. Huang, and K. T. Chuang. Dynamic Modeling of Solid Oxide Fuel Cell: The Effect of Diffusion and Inherent Impedance. *Journal of Power Sources*, 150:32–47, 2005.

[67] Y. Qi, B. Huang, and J. Luo. Dynamic Modeling of a Finite Volume of Solid Oxide Fuel Cell: The Effect of Transport Dynamics. *Chemical Engineering Science*, 61(18):6057–6076, 2006.

[68] C. Wang and M. H. Nehrir. A Physically Based Dynamic Model for Solid Oxide Fuel Cells. *IEEE Transactions on Energy Conversion*, 22(4):887–897, 2007.

[69] C. Wang, M. H. Nehrir, and S. R. Shaw. Dynamic Models and Model Validation for PEM Fuel Cells Using Electrical Circuits. *IEEE Transactions on Energy Conversion*, 20(2):442–451, 2005.

[70] J. Jia, R. Jiang, S. Shen, and A. Abudula. Effect of Operation Parameters on Performance of Tubular Solid Oxide Fuel Cell. *AIChE Journal*, 54(2):554–564, 2008.

[71] M. Sorrentino, C. Pianese, and Y. G. Guezennec. A Hierarchical Modeling Approach to the Simulation and Control of Planar Solid Oxide Fuel Cells. *Journal of Power Sources*, 180(1):380–392, 2008.

[72] L. Wang, H. Zhang, and S. Weng. Modeling and Simulation of Solid Oxide Fuel Cell Based on the Volume-Resistance Characteristic Modeling Technique. *Journal of Power Sources*, 177(2):579–589, 2008.

[73] P. Aguiar, C. S. Adjiman, and N. P. Brandon. Anode-Supported Intermediate Temperature Direct Internal Reforming Solid Oxide Fuel Cell. I: Model-Based Steady-State Performance. *Journal of Power Sources*, 138(1–2):120–136, 2004.

[74] P. Aguiar, C. S. Adjiman, and N. P. Brandon. Anode-Supported Intermediate-Temperature Direct Internal Reforming Solid Oxide Fuel Cell: II. Model-Based Dynamic Performance and Control. *Journal of Power Sources*, 147(1–2):136–147, 2005.

[75] Y. M. Barzi, M. Ghassemi, and M. H. Hamedi. A 2D Transient Numerical Model Combining Heat/Mass Transport Effects in a Tubular Solid Oxide Fuel Cell. *Journal of Power Sources*, 192(1):200–207, 2009.

[76] A. Chaisantikulwat, C. Diaz-Goano, and E. S. Meadows. Dynamic Modelling and Control of Planar Anode-Supported Solid Oxide Fuel Cell. *Computers & Chemical Engineering*, 32(10):2365–2381, 2008.

[77] A. M. Colclasure, B. M. Sanandaji, T. L. Vincent, and R. J. Kee. Modeling and Control of Tubular Solid-Oxide Fuel Cell Systems. I: Physical Models and Linear Model Reduction. *Journal of Power Sources*, 196(1):196–207, 2011.

[78] B. M. Sanandaji, T. L. Vincent, A. M. Colclasure, and R. J. Kee. Modeling and Control of Tubular Solid-Oxide Fuel Cell Systems: II. Nonlinear Model Reduction and Model Predictive Control. *Journal of Power Sources*, 196(1):208–217, 2011.

[79] P. Iora, P. Aguiar, C. S. Adjiman, and N. P. Brandon. Comparison of Two IT DIR-SOFC Models: Impact of Variable Thermodynamic, Physical, and Flow Properties. Steady-State and Dynamic Analysis. *Chemical Engineering Science*, 60(11):2963–2975, 2005.

[80] V. Menon, V. M. Janardhanan, S. Tischer, and O. Deutschmann. A Novel Approach to Model the Transient Behavior of Solid-Oxide Fuel Cell Stacks. *Journal of Power Sources*, 214:227–238, 2012.

[81] P. Kazempoor, F. Ommi, and V. Dorer. Response of a Planar Solid Oxide Fuel Cell to Step Load and Inlet Flow Temperature Change. *Journal of Power Sources*, 196(21):8948–8954, 2011.

[82] H. Zhu and R. J. Kee. Modeling Distributed Charge-Transfer Processes in SOFC Membrane Electrode Assemblies. *Journal of The Electrochemical Society*, 155(7):B715–B729, 2008.

[83] H. Zhu, R. J. Kee, V. M. Janardhanan, O. Deutschmann, and D. G. Goodwin. Modeling Elementary Heterogeneous Chemistry and Electrochemistry in Solid-Oxide Fuel Cells. *Journal of The Electrochemical Society,*, 152(12):A2427–A2440, 2005.

[84] J. Golbert, C. S. Adjiman, and N. P. Brandon. Microstructural Modeling of Solid Oxide Fuel Cell Anodes. *Industrial & Engineering Chemistry Research*, 47(20):7693–7699, 2008.

[85] S. H. Chan and Z. T. Xia. Anode Micro Model of Solid Oxide Fuel Cell. *Journal of The Electrochemical Society*, 148(4):A388–A394, 2001.

[86] E. S. Hecht, G. K. Gupta, H. Zhu, A. M. Dean, R. J. Kee, L. Maier, and O. Deutschmann. Methane Reforming Kinetics within a Ni-YSZ SOFC Anode Support. *Applied Catalysis A: General*, 295(1):40–51, 2005.

[87] S. Klein and G. Nellis. *Thermodynamics*. Cambridge University Press, New York, NY, 2011, pages 350–384, chapter 7.

[88] A. Franzoni, L. Magistri, A. Traverso, and A. F. Massardo. Thermoeconomic Analysis of Pressurized Hybrid SOFC Systems with $CO_2$ Separation. *Energy*, 33(2):311–320, 2008.

[89] M. Santin, A. Traverso, L. Magistri, and A. Massardo. Thermoeconomic Analysis of SOFC-GT Hybrid Systems Fed by Liquid Fuels. *Energy*, 35(2):1077–1083, 2010.

[90] D. F. Cheddie and R. Murray. Thermo-Economic Modeling of an Indirectly Coupled Solid Oxide Fuel Cell/Gas Turbine Hybrid Power Plant. *Journal of Power Sources*, 195(24):8134–8140, 2010.

[91] N. S. Siefert and S. Litster. Exergy and Economic Analyses of Advanced IGCC-CCS and IGFC-CCS Power Plants. *Applied Energy*, 107:315–328, 2013.

[92] N. S. Siefert, B. Y. Chang, and S. Litster. Exergy and Economic Analysis of a CaO-Looping Gasifier for IGFC-CCS and IGC-CCS. *Applied Energy*, 128:230–245, 2014.

[93] N. S. Siefert and S. Litster. Exergy & Economic Analysis of Biogas Fueled Solid Oxide Fuel Cell Systems. *Journal of Power Sources*, 272:386–397, 2014.

[94] A. A. Trendewicz and R. J. Braun. Techno-Economic Analysis of Solid Oxide Fuel Cell-Based Combined Heat and Power Systems for Biogas Utilization at Wastewater Treatment Facilities. *Journal of Power Sources*, 233:380–393, 2013.

[95] W. L. Becker, R. J. Braun, M. Penev, and M. Melaina. Design and Technoeconomic Performance Analysis of a 1 MW Solid Oxide Fuel Cell Polygeneration System for Combined Production of Heat, Hydrogen, and Power. *Journal of Power Sources*, 200:34–44, 2012.

[96] R. J. Braun. *Optimal Design and Operation of Solid Oxide Fuel Cell Systems for Small-Scale Stationary Applications*. PhD Thesis., University of Wisconsin-Madison, Madison, Wisconsin, 2002.

[97] R. J. Braun. Techno-Economic Optimal Design of Solid Oxide Fuel Cell Systems for Micro-Combined Heat and Power Applications in the U.S. *Journal of Fuel Cell Science and Technology*, 7(3):031018, 2010.

[98] A. Hawkes and M. Leach. Impacts of Temporal Precision in Optimisation Modelling of Micro-Combined Heat and Power. *Energy*, 30(10):1759–1779, 2005.

[99] A. Hawkes and M. A. Leach. Cost-Effective Operating Strategy for Residential Micro-Combined Heat and Power. *Energy*, 32(5):711–723, 2007.

[100] A. Hawkes and M. Leach. Solid Oxide Fuel Cell Systems for Residential Micro-Combined Heat and Power in the UK: Key Economic Drivers. *Journal of Power Sources*, 149:72–83, 2005.

[101] A. D. Hawkes, D. J. L. Brett, and N. P. Brandon. Fuel Cell Micro-CHP Techno-Economics: Part 1—Model Concept and Formulation. *International Journal of Hydrogen Energy*, 34(23):9545–9557, 2009.

[102] A. D. Hawkes, D. J. L. Brett, and N. P. Brandon. Fuel Cell Micro-CHP Techno-Economics: Part 2—Model Application to Consider the Economic and Environmental Impact of Stack Degradation. *International Journal of Hydrogen Energy*, 34(23):9558–9569, 2009.

[103] A. D. Hawkes, P. Aguiar, C. A. Hernandez-Aramburo, M. A. Leach, N. P. Brandon, T. C. Green, and C. S. Adjiman. Techno-Economic Modelling of a Solid Oxide Fuel Cell Stack for Micro Combined Heat and Power. *Journal of Power Sources*, 156(2):321–333, 2006.

[104] A. D. Hawkes, P. Aguiar, B. Croxford, M. A. Leach, C. S. Adjiman, and N. P. Brandon. Solid Oxide Fuel Cell Micro Combined Heat and Power System Operating Strategy: Options for Provision of Residential Space and Water Heating. *Journal of Power Sources*, 164(1):260–271, 2007.

[105] N. Autissier, F. Palazzi, F. Marechal, J. van Herle, and D. Favrat. Thermo-Economic Optimization of a Solid Oxide Fuel Cell, Gas Turbine Hybrid System. *Journal of Fuel Cell Science and Technology*, 4(2):123–129, 2007.

[106] F. Palazzi, N. Autissier, F. M. A. Marechal, and D. Favrat. A Methodology for Thermo-Economic Modeling and Optimization of Solid Oxide Fuel Cell Systems. *Applied Thermal Engineering*, 27(16):2703–2712, 2007.

[107] F. Marechal, F. Palazzi, J. Godat, and D. Favrat. Thermo-Economic Modelling and Optimisation of Fuel Cell Systems. *Fuel Cells*, 5(1):5–24, 2005.

[108] Environmental Management—Life Cycle Assessment—Requirements and Guidelines. ISO 14044:2006(E), 2006.

[109] Environmental Management—Life Cycle Assessment—Principles and Framework ISO 14040:2006(E), 2006.

[110] I. Staffell, A. Ingram, and K. Kendall. Energy and Carbon Payback Times for Solid Oxide Fuel Cell Based Domestic CHP. *International Journal of Hydrogen Energy*, 37(3):2509–2523, 2012.

[111] U.S. Energy Information Administration. Environment. Accessed online at ⟨http://www.eia.gov/environment/data.cfm⟩ (see document titled, "Summary by Electric Power"). Accessed on July 21, 2015, Release date: June 25, 2015.

[112] U.S. Energy Information Administration. Electricity. Accessed online at ⟨http://www.eia.gov/electricity/data.cfm⟩ (see document titled, "Electric Power Sector"). Accessed on July 21, 2015, Release date: June 25, 2015.

[113] M. Pehnt. *Handbook of Fuel Cells*, volume 4, chapter Life-Cycle Analysis of Fuel Cell System Components, pages 1293–1317. John Wiley & Sons Ltd, Chichester, England, 2003.

[114] M. A. Rosen, I. Dincer, and A. Ozbilen. *Life Cycle Assessment Handbook*, chapter Exergy Analysis and its Connection to Life Cycle Assessment, pages 185–215. Scrivener Publishing LLC, Beverly, MA, 2012.

[115] A. Ozbilen, I. Dincer, and M. A. Rosen. Exergetic Life Cycle Assessment of a Hydrogen Production Process. *International Journal of Hydrogen Energy*, 37(7):5665–5675, 2012.

[116] P. Costamagna and K. Honegger. Modeling of Solid Oxide Heat Exchanger Integrated Stacks and Simulation at High Fuel Utilization. *Journal of The Electrochemical Society*, 145(11):3995–4007, 1998.

[117] P. Costamagna, A. Selimovic, M. Del Borghi, and G. Agnew. Electrochemical Model of the Integrated Planar Solid Oxide Fuel Cell (IP-SOFC). *Chemical Engineering Journal*, 102(1):61–69, 2004.

[118] S. Ubertini and R. Bove. *Modeling Solid Oxide Fuel Cells: Methods, Procedures and Techniques*, volume 1, chapter Mathematical Models: A General Overview, pages 51–93. Springer Science+Business Media, B.V., Dordrecht, Netherlands, 2008.

[119] M. Mogensen and T. Lindegaard. The Kinetics of Hydrogen Oxidation on a Ni-YSZ SOFC Electrode at 1000°C. In S. C. Singal and T. Iwahara, editors, *Solid Oxide Fuel Cells III (The Electrochemical Society Proceedings Series)*, pages 484–493. The Electrochemical Society, 1993.

[120] M. Mogensen. Electrode Kinetics of SOFC Anodes and Cathodes. In F. W. Poulsen, J. J. Bentzen, T. Jacobsen, E. Skou, and M. J. L. Østegård, editors, *Proceedings of the 14th Risø International Symposium on Material Science*, pages 117–135. Risø National Laboratory, 1993.

[121] E. Achenbach. Three-Dimensional and Time-Dependent Simulation of a Planar Solid Oxide Fuel Cell Stack. *Journal of Power Sources*, 49(1–3):333–348, 1994.

[122] F. P. Incropera, D. P. DeWitt, T. L. Bergman, and A. S. Lavine. *Fundamentals of Heat and Mass Transfer*. John Wiley & Sons, Inc., Hoboken, NJ, sixth edition, 2007.

[123] E. L. Cussler. *Diffusion: Mass Transfer in Fluid Systems*. Cambridge University Press, Cambridge, England, second edition, 1997, page 173, chapter 6.

[124] S. H. Chan, K. A. Khor, and Z. T. Xia. A Complete Polarization Model of a Solid Oxide Fuel Cell and its Sensitivity to the Change of Cell Component Thickness. *Journal of Power Sources*, 93(1–2):130–140, 2001.

[125] A. F. Mills. *Mass Transfer*. Prentice-Hall, Inc., Upper Saddle River, NJ, 2001, pages 68–69, chapter 2.

[126] R. B. Bird, W. E. Stewart, and E. N. Lightfoot. *Transport Phenomena*. John Wiley & Sons, Inc., New York, NY, second edition, 2007, pagse 526–527, chapter 17.

[127] U. G. Bossel. Facts & Figures: Final report on SOFC Data. Final Report on SOFC Data, International Energy Agency and Swiss Federal Office of Energy, 1992.

[128] Personal correspondence with F. J. Rohr. ABB Research Center Heidelberg/Germany.

[129] H. Koide, Y. Someya, T. Yoshida, and T. Maruyama. Properties of Ni/YSZ Cermet as Anode for SOFC. *Solid State Ionics*, 132(3–4):253–260, 2000.

[130] M. G. H. M. Hendriks, J. E. ten Elshof, H. J. M. Bouwmeester, and H. Verweij. The Electrochemical Double-Layer Capacitance of Yttria-Stabilised Zirconia. *Solid State Ionics*, 146(3–4):211–217, 2002.

[131] S. C. Chapra and R. P. Canale. *Numerical Methods for Engineers*. The McGraw-Hill Companies, Inc., New York, NY, sixth edition, 2010.

[132] E. Achenbach and E. Riensche. Methane/Steam Reforming Kinetics for Solid Oxide Fuel Cells. *Journal of Power Sources*, 52(2):283–288, 1994.

[133] R. E. Treybal. *Mass-Transfer Operations*. McGraw-Hill, Inc., New York, NY, third edition, 1980, pages 29–30, chapter 2.

[134] D. Bhattacharyya and R. Rengaswamy. A Review of Solid Oxide Fuel Cell (SOFC) Dynamic Models. *Industrial & Engineering Chemistry Research*, 48(13):6068–6086, 2009.

[135] R. K. Shah and A. L. London. *Advances in Heat Transfer, Supplement I: Laminar Flow Forced Convection in Ducts*. Academic Press, Inc., New York, NY, 1978, pages 199–203, chapter 7.

[136] B. E. Poling, J. M. Prausnitz, and J. P. O'Connell. *The Properties of Gases and Liquids*. The McGraw-Hill Companies, Inc., New York, NY, fifth edition, 2001.

[137] F. White. *Viscous Fluid Flow*. The McGraw-Hill Companies, Inc., New York, NY, third edition, 2006.

[138] Y. A. Çengel and J. M. Cimbala. *Fluid Mechanics: Fundamentals and Applications*. The McGraw-Hill Companies, Inc., New York, NY, second edition, 2010, p. 345, chapter 8.

[139] W. M. Kays and A. L. London. *Compact Heat Exchangers*. McGraw-Hill, Inc., New York, NY, third edition, 1984, pp. 35–38, chapter 2.

[140] R. J. Kee, P. Korada, K. Walters, and M. Pavol. A Generalized Model of the Flow Distribution in Channel Networks of Planar Fuel Cells. *Journal of Power Sources*, 109(1):148–159, 2002.

[141] S. A. Klein. Engineering Equation Solver (EES). V9.715, Copyright 2014.

[142] E. Achenbach. Annex II: Modelling and Evaluation of Advanced Solid Oxide Fuel Cells: SOFC Stack Modelling. Final Report of Activity A2, International Energy Agency, 1996.

[143] R. R. Judkins. U. S. Patent for Iron Aluminide Alloy Container for Solid Oxide Fuel Cells. Patent No. 6,114,058, 2000.

[144] J. Thijssen, LLC. The Impact of Scale-Up and Production Volume on SOFC Manufacturing Cost. Accessed online at ⟨https://www.netl.doe.gov/File%20Library/research/coal/energy%20systems/fuel%20cells/JT-Manufacturing-Study-Report-070522.pdf⟩, National Energy Technology Laboratory, 2007.

[145] Arthur D. Little, Inc. Conceptual Design of POX/SOFC 5kW Net System. Accessed online at ⟨http://www.netl.doe.gov/File%20Library/research/coal/energy%

20systems/fuel%20cells/conceptualdesignofpoxsofc5kwnetsystem.pdf⟩, National Energy Technology Laboratory, 2001.

[146] E. Riensche, U. Stimming, and G. Unverzagt. Optimization of a 200 kW SOFC Cogeneration Power Plant Part I: Variation of Process Parameters. *Journal of Power Sources*, 73(2):251–256, 1998.

[147] W. L. Lundberg. Solid Oxide Fuel Cell Cogeneration System Conceptural Design. Technical Report GRI-89/0162, Gas Research Institute, 1989.

[148] X. Zhang, S. H. Chan, G. Li, H. K. Ho, J. Li, and Z. Feng. A Review of Integration Strategies for Solid Oxide Fuel Cells. *Journal of Power Sources*, 195(3):685–702, 2010.

[149] Personal communication with William O. Collinge, Postdoctoral Researcher at the University of Pittsburgh. December, 2013 and January, 2014.

[150] J. A. Duffie and W. A. Beckman. *Solar Engineering of Thermal Processes*. John Wiley & Sons, Inc., Hoboken, NJ, fourth edition, 2013, pages 447–476, chapter 11.

[151] M. W. Ellis and M. B. Gunes. Status of Fuel Cell Systems for Combined Heat and Power Applications in Buildings. *ASHRAE Transactions*, 108:1032–1044, 2002.

[152] R. A. Newby A. K. S. Iyengar and D. L. Keairns. Techno-Economic Analysis of Integrated Gasification Fuel Cell Systems Created by Energy Sector Planning and Analysis for SEAP & OPPB (Executive summary and Section 2.10 Cost Estimating Methodology). Accessed online at ⟨http://netl.doe.gov/File%20Library/Research/Energy%20Analysis/Publications/341_03_05_FR_IGFC_Rev1H_20141120.pdf⟩ DOE/NETL-341/112613, National Energy Technology Laboratory, 2014.

[153] Battelle. Manufacturing Cost Analysis of 1 kW and 5 kW Solid Oxide Fuel Cell (SOFC) for Auxiliary Power Applications. Accessed online at ⟨http://energy.gov/sites/prod/files/2014/06/f16/fcto_battelle_cost_analysis_apu_feb2014.pdf⟩, U.S. Department of Energy, 2014.

[154] Access Intelligence, LLC. Plant Cost Index. Accessed online at ⟨http://www.chemengonline.com/pci⟩. Accessed on July 21, 2015, Copyright 2014.

[155] W. G. Sullivan, E. M. Wicks, and C. P. Koelling. *Engineering Economy*. Pearson Higher Education, Inc., Upper Saddle River, NJ, fifteenth edition, 2012.

[156] M. R. Weimar, L. A. Chick, D. W. Gotthold, and G. A. Whyatt. Cost Study for Manufacturing of Solid Oxide Fuel Cell Power Systems. Accessed online at ⟨http://www.pnnl.gov/main/publications/external/technical_reports/PNNL-22732.pdf⟩, Pacific Northwest National Laboratory, 2013.

[157] M. S. Peters and K. D. Timmerhaus. *Plant Design and Economics for Chemical Engineers*. McGraw-Hill, Inc., New York, NY, fourth edition, 1991, pages 160–162, chapter 6.

[158] R. Newby and D. Keairns. Analysis of Natural Gas Fuel Cell Plant Configurations—Revision 1 (Executive Summary and Section 2.6 Economic Analysis). Accessed online at ⟨http://netl.doe.gov/File%20Library/Research/Energy%20Analysis/Publications/341_02_20_FR_rev2A_20140221_NGFC_Cost_Study.pdf⟩ DOE/NETL-2013/1593, National Energy Technology Laboratory, 2013.

[159] TIAX LLC. Scale-Up Study of 5-kW SECA modules to a 250-kW System. Accessed online at ⟨http://www.netl.doe.gov/File%20Library/research/coal/energy%20systems/fuel%20cells/scaleupstudyof5kwsecamodulestoa250kw.pdf⟩, National Energy Technology Laboratory, 2002.

[160] D. S. Parker. Research Highlights from a Large Scale Residential Monitoring Study in a Hot Climate. *Energy and Buildings*, 35(9):863–876, 2003.

[161] National Action Plan for Energy Efficiency. Sector Collaborative on Energy Efficiency Accomplishments and Next Steps (Chapter 3: Energy Use and Savings Profiles). Accessed online at ⟨http://www.epa.gov/cleanenergy/documents/suca/sector_collaborative.pdf⟩, ICF International, 2008.

[162] D. Waldbillig, A. Wood, and D. G. Ivey. Electrochemical and Microstructural Characterization of the Redox Tolerance of Solid Oxide Fuel Cell Anodes. *Journal of Power Sources*, 145(2):206–215, 2005.

[163] J. Pusz, A. Smirnova, A. Mohammadi, and N. M. Sammes. Fracture Strength of Micro-Tubular Solid Oxide Fuel Cell Anode in Redox Cycling Experiments. *Journal of Power Sources*, 163(2):900–906, 2007.

[164] D. Fouquet, A. C. Müller, A. Weber, and E. Ivers-Tiffée. Kinetics of Oxidation and Reduction of Ni/YSZ Cermets. *Ionics*, 9(1-2):103–108, 2003.

[165] A Selimovic, M. Kemm, T. Torisson, and M. Assadi. Steady State and Transient Thermal Stress Analysis in Planar Solid Oxide Fuel Cells. *Journal of Power Sources*, 145(2):463–469, 2005.

[166] A. Hagen, R. Barfod, P. V. Hendriksen, Y.-L. Liu, and S. Ramousse. Degradation of Anode Supported SOFCs as a Function of Temperature and Current Load. *Journal of The Electrochemical Society*, 153(6):A1165–A1171, 2006.

[167] A. Hagen, Y. L. Liu, R. Barfod, and P. V. Hendriksen. Assessment of the Cathode Contribution to the Degradation of Anode-Supported Solid Oxide Fuel Cells. *Journal of The Electrochemical Society*, 155(10):B1047–B1052, 2008.

[168] Y. L. Liu, A. Hagen, R. Barfod, M. Chen, H. J. Wang, F. W. Poulsen, and P. V. Hendriksen. Microstructural Studies on Degradation of Interface between LSM-YSZ Cathode and YSZ Electrolyte in SOFCs. *Solid State Ionics*, 180(23–25):1298–1304, 2009.

[169] G. F. Franklin, J. D. Powell, and M. L. Workman. *Digital Control of Dynamic Systems*. Addison Wesley Longman, Inc., Menlo Park, California, 1998.

[170] R. S. Esfandiari and B. Lu. *Modeling and Analysis of Dynamic Systems*. Taylor and Francis Group, LLC, Boca Raton, Florida, 2010.

[171] U.S. Energy Information Administration. Natural Gas. Accessed online at ⟨http://www.eia.gov/dnav/ng/ng_pri_sum_dcu_nus_m.htm⟩. Accessed on July 21, 2015, Release Date: June 30, 2015.

[172] U.S. Energy Information Administration. Electric Power Monthly. Accessed online at ⟨http://www.eia.gov/electricity/monthly/epm_table_grapher.cfm?t=epmt_5_03⟩. Accessed on July 21, 2015, Release Date: June 15, 2015.

[173] U.S. Environmental Protection Agency. Sources of Greenhouse Gas Emissions. Accessed online at ⟨http://www.epa.gov/climatechange/ghgemissions/sources.html⟩. Accessed on July 21, 2015, Last updated on July 21, 2015.

[174] U.S. Environmental Protection Agency. Fact Sheet: Details About the Proposal for New Sources. Accessed online at ⟨http://www2.epa.gov/carbon-pollution-standards/fact-sheet-details-about-proposal-new-sources⟩. Accessed on July 21, 2015, Last updated on January 8, 2015.

[175] U.S. Environmental Protection Agency. Where You Live. Accessed online at ⟨http://www2.epa.gov/carbon-pollution-standards/where-you-live⟩. Accessed on July 21, 2015, Last updated on November 6, 2014.